POLITECNICO DI MILANO

Facoltà di Ingegneria dei Sistemi
Corso di Laurea Specialistica in Ingegneria Biomedica

Patient-Specific Monoventricular Models of Cardiac Biomechanics for Hypoplastic Left Heart Syndrome

Relatore: Prof. Alberto C. L. Redaelli

Correlatore: Ing. Emiliano Votta

Tesi di Laurea di:

Giulia CONCA
814229

Anno Accademico 2014/2015

Contents

Abstract

Cardiac malformations are the most common type of congenital defect, and affect approximately 1% of all newborns. Thanks to the progressive improvements in the management of complex congenital heart diseases (CHDs), currently more than 90% of CHD-affected children survive until the early adult age [1, 2]. Unfortunately, many of these patients, and particularly those affected by functional single ventricle or systemic right ventricle (RV), are at risk of ventricular dilatation and dysfunction with associated morbidity and mortality [3]. Often, even though on the long term, the final outcome is heart failure (HF), with leads to worse quality of life and shorter life expectancy [4]; however, the occurrence of HF is affected by the specific surgical treatment initially performed on the patient.

Nowadays, computational models of cardiac electro-mechanics (EM) are increasingly being considered in clinical applications as an additional modality to optimize therapies or understand therapy mechanisms.

On this basis, the thesis project herein described focuses on the development of patient-specific finite element models of the RV in a preliminary cohort of patients suffering from hypoplastic left heart syndrome (HLHS). HLHS is a single ventricle defect characterized by underdevelopment or absence of the left ventricle. It usually includes hypoplasia of the left ventricle and ascending aorta, mitral and aortic valve atresia or stenosis.

The primary goal of the project is to identify and statistically validate new model-derived parameters of ventricular shape and mechanics that may serve as early clinical markers for adverse remodeling and heart failure in adult HLHS patients.

Materials and methods

Patient-specific cardiovascular model consists of four main components: an anatomic model of the ventricle, a passive constitutive model, an active contractile model, and a hemodynamic model.

The anatomic model of the ventricles consists of the unloaded ventricular geometry and a fiber-sheet local material coordinate system, which represents the myofibres and sheet architecture. The second component of the patient-specific model consists of the constitutive law for the resting myocardial material properties. The third component is the active-contractile law that simulates muscle contraction. The last component is the

lumped-parameter closed-loop hemodynamic model that generates the boundary condition for the ventricular finite-element model.

For the project, cardiac MRIs of two patients (RCH-5-1 and RCH-6-1) affected by HLHS were collected from the Rady Children's Hospital, San Diego. Short axis images at the end of diastole were first segmented using the software *Seg3D*. Then, segmentation outputs were imported in *Blender*, where a mono-ventricular mesh template was fitted with the patient-specific data.

The software *Continuity* was used to enrich the model with fibers and to run biomechanics simulations with the aim of estimating passive, active, and hemodynamics parameters.

The unloaded reference state was estimated using two different approaches. The first approach consisted in the use of the algorithm developed by Krishnamurthy et al. [5]. This method can estimate the unloaded state given the end-diastolic geometry, pressure, and passive material properties. Passive material properties were unknown for HLHS patients considered in the project. Optimized patient-specific parameters [5] have been used to run the simulation. At the end, Klotz's empirical relationship [6] was used to scale the passive material parameters so that the right-ventricular cavity volume of the unloaded model matched the empirical value predicted by Klotz relation. The second approach consisted in the use of the images at 1/3 of the diastolic timeframe. These were segmented from MRI and then fitted with the template mesh. The resulting discretized geometry was considered as the unloaded configuration of the ventricle. Passive inflation was simulated starting from the unloaded geometry to reach the end-diastolic one.

After the passive material parameters and unloaded geometry were obtained, the contractile parameters and the hemodynamic parameters were determined to match the measured peak right ventricular pressures and end-systolic volume, using a full beat simulation. Similarly as the unloaded geometry estimation, the simulation was first performed with the default hemodynamic and active parameters from Kerckhoffs et al. [7] and then these were then manually adjusted.

The output files of the full beat simulation were used to estimate the stress and strain distribution, as well as the stroke work density and the total cardiac work.

Results

The analyzed cardiac MRIs clearly showed the severe underdevelopment of the left ventricle for both patients. For RCH-5-1 the right ventricle is completely deformed, elongated, and lumpy, showing a very thick ventricular wall. Conversely, RCH-6-1 has a more spherical right ventricle and the ventricular wall is thinner than in the previous patient.

The low image resolution and the use of a template mesh with few elements led to relevant geometric fitting errors; the reconstructed 3D models underestimated the intracavitary volume measured directly from medical images by 16.4% and 5.5% for RCH-5-1 and RCH-6-1, respectively.

The two different approaches used to get the unloaded reference state were analyzed.

The loaded mesh cavity volume obtained with the Krishnamurthy's algorithm was evaluated and compared with the value computed directly from the MRI model. The error of 0.14% and 0.7% for the two modeled ventricles led to the conclusion that the algorithm allows for error minimization between the fitted mesh and the new loaded geometry. Despite yielding the correct end-diastolic volume, the two models are characterized by an excessively stiff behavior.

The second approach was considered acceptable for HLHS patients. Three combinations of *a* parameters and *b* parameters allowed for obtaining the correct end-diastolic volume, but only the third one (bulk modulus decrease) allows for obtain the passive inflation curves (Figure 1).

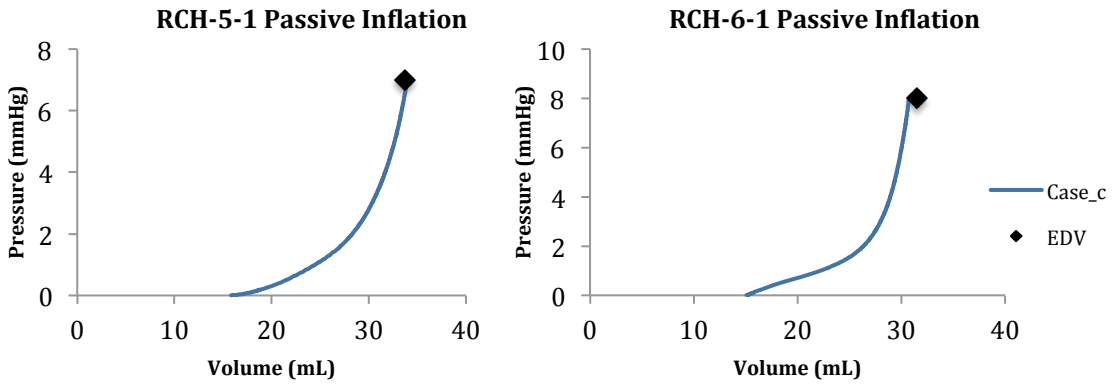

Figure 1 – Passive inflation curve obtained changing the material parameters. These start from the unloaded volume (computed from the reconstructed unloaded geometry) and closely match the EDV of the fitted model.

After the identification of the passive material constitutive parameters allowing for replicating the theoretical pressure-volume behavior during passive inflation, the simulation of an entire cardiac cycle was performed.

In both patients, the diastolic portion of the Pressure-Volume loop replicates the corresponding pressure-volume curve obtained through passive inflation. This evidence means there is a good agreement between the passive and active contraction simulations.

The discrepancy in the end-diastolic and end-systolic volume between clinical measurements and simulation was obtained, probably due to an overly stiff passive behavior in the simulation; the ventricle is less compliant, and hence increases its volume less than it should during diastolic filling.

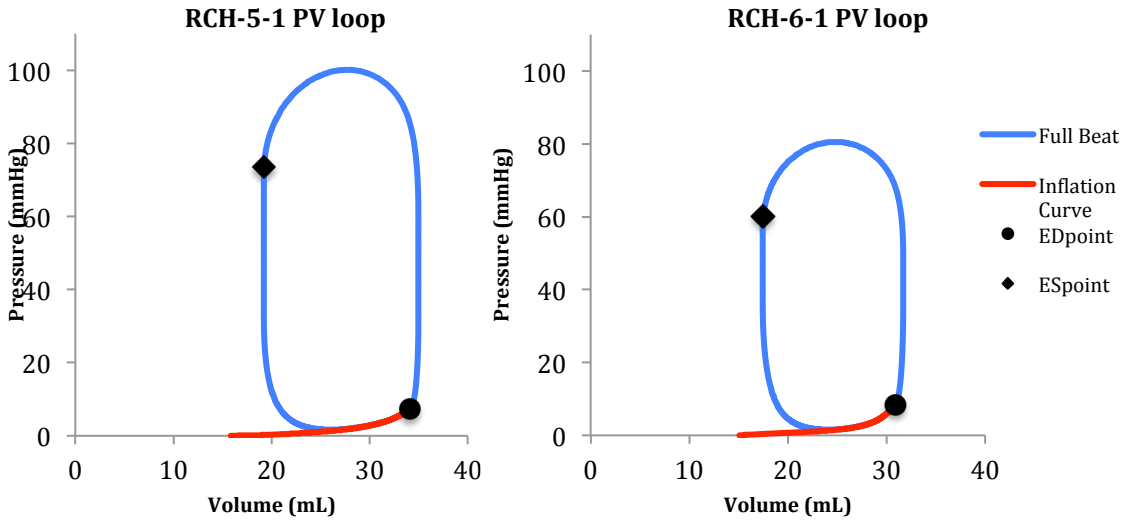

Figure 2 – Pressure-Volume loop. Red: passive inflation curve. Blue: entire cardiac cycle.

Stress and strain distributions over the whole ventricular wall were computed at end-diastole, end-systole, and systolic peak. Similarly, stroke work density and total work were calculated. These values were compared with those from previous studies on mono-ventricular [8-10] or biventricular [11] models. The simulation results are largely comparable with the values reported in these works.

Conclusions

This work focused on patient-specific finite element models construction from cardiac MRIs and consecutive biomechanical simulations.

Some of the methods, such as segmentation, are still performed manually and can lead to systematic errors. In addition, some of the methods such as determination of the hemodynamic parameters are performed independently that might lead to some variation between the estimated and actual parameters. This can be better solved with the help of an optimization algorithm that can find the parameters that match the model output with measurements.

In conclusion, the viability of creating detailed patient-specific models to perform biomechanics simulations was demonstrated. The models are capable of replicating patient-specific global cardiac function. These could be use to study the effect of different interventions with the goal of predicting treatments for heart disease.

References

[1] A. J. Marelli, A. S. Mackie, R. Ionescu-Ittu, E. Rahme, L. Pilote. 2007. *Congenital heart disease in the general population: changing prevalence and age distribution*. Circulation 115: 163-172.

[2] M. E. Brickner, L. D. Hillis, R. A. Lange. 2000. *Congenital heart disease in adults. First of two parts*. N Engl J Med. 342: 256-263.

[3] M. E. Brickner, L. D. Hillis, R. A. Lange. 2000. *Congenital heart disease in adults. Second of two parts*. N Engl J Med 342: 334-342.

[4] S. Piran, G. Veldtman, S. Siu, G. D. Webb, P. P. Liu. 2002. *Heart failure and ventricular dysfunction in patients with single or systemic right ventricles.* Circulation 105: 1189-1194.

[5] A. Krishnamurthy, C. T. Villongco, J. Chuang, L. R. Frank, V. Nigam, E. Belezzuoli, P. Stark, D. E. Krummen, S. Narayan, J. H. Omens, A. D. McCulloch, R. C. P. Kerckhoffs. 2013. *Patient-specific models of cardiac biomechanics*. J Comput Phys 244: 4–21.

[6] S. Klotz, I. Hay, M. L. Dickstein, G. H. Yi, J. Wang, M. S. Maurer, D. A. Kass, D. Burkhoff. 2006. *Single-beat estimation of end-diastolic pressure-volume relationship: a novel method with potential for noninvasive application*. American Journal of Physiology – Heart and Circulatory Physiology 291 (1): H403–H412.

[7] R. C. Kerckhoffs, M. L. Neal, Q. Gu, J. B. Bassingthwaighte, J. H. Omens, A. D. McCulloch. 2007. *Coupling of a 3D Finite Element Model of Cardiac Ventricular Mechanics to Lumped Systems Models of the Systemic and Pulmonic Circulation*. Ann Biomed Eng 35: 1–18.

[8] R. C. P. Kerckhoffs, J. H. Omens, A. D. McCulloch, L. J. Mulligan. 2010. *Ventricular dilation and electrical dyssynchrony synergistically increase regional mechanical non-uniformity but not mechanical dyssynchrony: A computational model*. Circ Heart Fail 3 (4): 528–536.

[9] W. Kroon, T. Delhaas, P. Bovendeerd, T. Arts. 2009. *Computational analysis of the myocardial structure: Adaptation of cardiac myofiber orientations through deformation*. Medical Image Analysis 13: 346–353.

[10] F. Dorri , P. F. Niederer, P. P. Lunkenheimer. 2006. *A finite element model of the human left ventricular systole*. Computer Methods in Biomechanics and Biomedical Engineering 9 (5): 319-341.

[11] M. Pluijmert, P. H. Bovendeerd, W. Kroon. 2014. *Effects of activation pattern and active stress development on myocardial shear in a model with adaptive myofiber reorientation*. Am J Physiol Heart Circ Physiol 306: H538–46.

Sommario

Le malformazioni cardiache rappresentano uno dei più comuni tipi di malattie congenite, e colpiscono circa l' 1% dei neonati. Grazie al progressivo sviluppo nel trattamento delle malattie cardiache congenite (CHDs), attualmente più del 90% dei bambini affetti da CHD sopravvivono fino all'età adulta [1, 2]. Sfortunatamente molti di questi pazienti, principalmente affetti da patologia del singolo ventricolo (SV), sono a rischio di disfunzioni o dilatazione ventricolare con conseguente stato patologico o morte [3]. Spesso, risultato a lungo termine è l'insufficienza cardiaca (HF) che porta a un peggioramento delle condizioni di vita, nonché a una minor aspettativa di vita [4]. Tuttavia, la presenza di HF è fortemente influenzata dallo specifico trattamento chirurgico effettuato sul paziente.

Ad oggi, i modelli computazionali che replicano il comportamento elettro-meccanico del cuore stanno diventando sempre più considerati nelle applicazioni cliniche come metodologia addizionale per l'ottimizzazione di trattamenti e la valutazione di relativi meccanismi terapici.

Il progetto qui descritto si concentra sullo sviluppo di modelli ad elementi finiti paziente-specifici di singolo ventricolo destro per la patologia del cuore sinistro ipoplasico (HLHS). Si tratta di una patologia a ventricolo unico caratterizzata dal sottosviluppo o assenza del ventricolo sinistro e include ipoplasia del ventricolo sinistro, dell'aorta e della valvola mitrale, nonché atresia o stenosi della valvola mitrale.

Lo scopo principale del progetto è l'identificazione e la validazione statistica di nuovi parametri riguardanti la forma e la meccanica ventricolare che possano essere utili per la valutazione di rimodellamento non fisiologico o insufficienza cardiaca in adulti affetti da HLHS.

Materiali e metodi

I modelli cardiovascolari paziente-specifici sono composti da quattro componenti: un modello anatomico del ventricolo, un modello costitutivo che descrive il comportamento passivo del miocardio, un modello attivo che descrive il comportamento contrattile, e un modello emodinamico.

Il modello anatomico è a sua volta composto dalla geometria allo stato scaricato e dal sistema di coordinate locali rappresentante l'architettura delle fibre. Il modello passivo è

rappresentato dalla legge costitutiva del materiale mentre quello attivo dalla legge contrattile che stima la contrazione muscolare. L'ultima componente contiene i parametri emodinamici che permettono di generare le condizioni al contorno per il modello ad elementi finiti.

Per il progetto qui trattato, le immagini cardiache di risonanza magnetica (MRIs) di due pazienti (RCH-5-1 e RCH-6-1) affetti da HLHS sono state raccolte dal Rady Children's Hospital di San Diego. Inizialmente le immagini in asse corto a fine diastole sono state segmentate utilizzando il software *Seg3D*. In seguito, le segmentazioni sono state importate in *Blender* e un mesh template mono-ventricolare è servito per replicare la geometria ventricolare.

Ad ultimo, il software *Continuity* è stato utilizzato per arricchire il modello con fibre e per effettuare simulazioni biomeccaniche.

La stato scaricato è stato stimato mediante due approcci. Inizialmente è stato utilizzato l'algoritmo sviluppato da Krishnamurthy et al. [5]. Il metodo permette la stima della geometria scaricata, noti la geometria e la pressione di fine diastole, nonché le proprietà passive del materiale. Non avendo a disposizione i valori specifici delle proprietà passive del materiale, sono inizialmente stati sfruttati valori da letteratura [5] per effettuare la simulazione. Una volta ottenuta la geometria e il valore di volume ventricolare allo stato scaricato, la relazione empirica descritta da Klotz [6] è stata utilizzata per aggiustare i parametri passivi in modo da ottenere una curva di riempimento passivo che possa ben essere descritta da quella di Klotz. Successivamente è stato testato un secondo metodo. Sono state segmentate le immagini a 1/3 della diastole e in seguito è stata sfruttata una mesh monoventricolare per descrivere la geometri ventricolare. La geometria discretizzata è stata considerata come geometria scaricata del ventricolo. Simulazioni di riempimento passivo a partire da tale geometria hanno permesso la stima dei parametri passivi del materiale.

Una volta trovati le proprietà passive e la geometria allo stato scaricato, i parametri attivi contrattili ed emodinamici sono stati stimati tramite la simulazione di un ciclo cardiaco completo. Così come per la precedente simulazione, inizialmente la simulazione viene eseguita utilizzando parametri di default [7], per poi essere manualmente modificati in modo da ottenere i valori corretti di pressione di picco sistolico e di fine sistole.

I dati ottenuti dalla simulazione sono stati infine utilizzati per stimare il lavoro cardiaco e la distribuzione di sforzo e deformazione nella parete ventricolare.

Risultati

Le immagini cardiache analizzate hanno mostrato un grave sottosviluppo del ventricolo sinistro in entrambi i pazienti. Inoltre, nel primo paziente (RCH-5-1) il ventricolo destro appare allungato e deformato, mentre nel secondo (RCH-6-1) risulta più tondeggiante.

La bassa risoluzione delle immagini a disposizione e l'utilizzo di un mesh template caratterizzato solamente da 28 elementi per descrivere la complessa superficie ventricolare, hanno portato a errori geometrici di 16.4% e 5.5% rispettivamente per i due pazienti.

La geometria scaricata è stata stimata utilizzando due diversi approcci. Il primo approccio prevedeva l'utilizzo dell'algoritmo sviluppato da Krishnamurthy [5]. Il volume di fine diastole ottenuto in seguito a tale simulazione è stato confrontato con quello della geometria a fine diastole costruita direttamente dalle immagini MRI. L'errore di 0.14% e 0.7% per i due modelli ha portato a concludere che l'algoritmo consente la minimizzazione dell'errore tra la geometria costruita e quella simulata.

Nonostante ciò, il successivo tentativo di modificare i parametri costitutivi per ottenere una forma della curva paragonabile a quella empirica di Klotz ha rivelato l'impossibilità di ottenere un buon risultato; la curva infatti risultava avere un comportamento molto più rigido di quello desiderato.

Un secondo approccio è stato quindi testato per questo scopo. Le immagini a 1/3 della diastole sono state segmentate dalle MRI, seguendo lo stesso procedimento utilizzato per la costruzione della geometria a fine diastole. Tre combinazioni di parametri costitutivi permettevano di ottenere un volume di fine diastole simile a quello discretizzato in precedenza, ma sono l'ultima combinazione (la quale prevedeva una diminuzione del modulo di compressibilità) consentiva di ottenere una curva pressione-volume di carattere esponenziale (Figura 1).

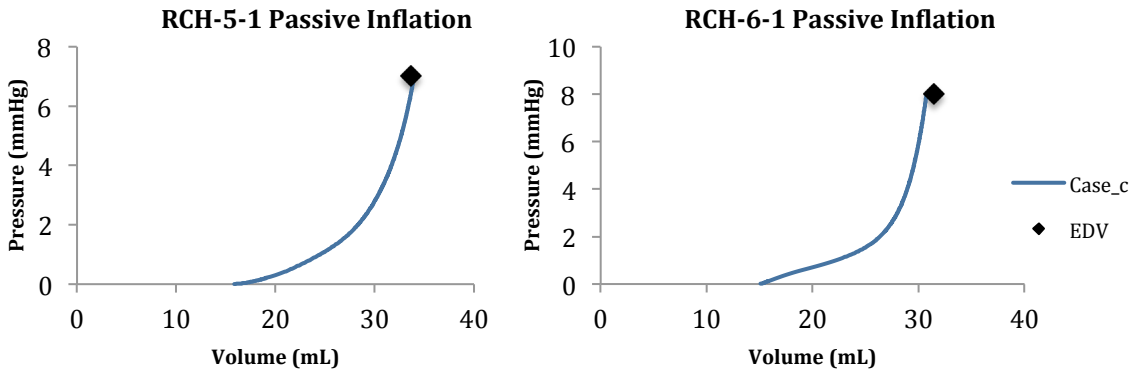

Figura 1 – Curve di riempimento passive ottenute in seguito alla modifica dei parametri costitutivi. Le curve partono dal volume della geometria scaricata ottenuto dalle MRI e raggiungono un volume di fine diastole molto simile a quello ottenuto dalla geometria costruita.

In seguito, è stata effettuata la simulazione dell'intero ciclo cardiaco per stimare i parametri attivi contrattili ed emodinamici. Il ciclo pressione-volume (Figura 2) per i pazienti RCH-5-1 e RCH-6-1 ha mostrato un buon accordo tra la simulazione effettuata e la precedente. La differenza volumetrica tra i dati clinici misurati e quelli simulati nei punti di fine sistole e fine diastole ha rivelato un comportamento più rigido nella simulazione che nella realtà. Il volume ventricolare ottenuto è quindi minore di quello misurato.

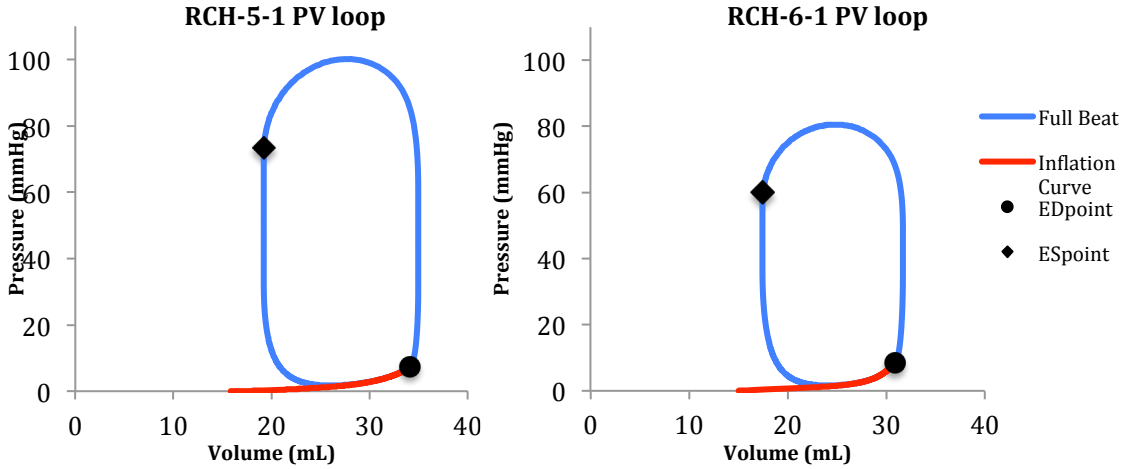

Figura 2 – Ciclo pressione-volume. In rosso la curva di riempimento passivo mentre in blu l'intero ciclo cardiaco.

Infine, sono state calcolate le distribuzioni di sforzo e deformazione nella parete ventricolare nei punti di fine sistole, fine diastole e picco sistolico. Da questi poi, il lavoro cardiaco totale. I risultati ottenuti hanno mostrato buon accordo con i valori riportati in letteratura [8-11].

Conclusioni

Questo lavoro ha trattato lo sviluppo di modelli ad elementi finiti paziente-specifici a partire da immagini di risonanza magnetica, nonché la successiva determinazione di parametri atti a descriverne il comportamento meccanico.

Alcuni metodi utilizzati, come ad esempio la segmentazione, sono ancora effettuati manualmente e questo può portare a errori sistematici. Inoltre, l'utilizzo di alcuni metodi potrebbe essere migliorato tramite un algoritmo di ottimizzazione che stima i parametri in uscita dalla simulazione in modo da confrontarli direttamente con quelli misurati; un esempio è la determinazione dei parametri emodinamici.

In conclusione, si può affermare che con questo lavoro è stata dimostrata quindi la realizzabilità di modelli dettagliati paziente-specifici per la simulazione del comportamento meccanico ventricolare; essi sono infatti in grado di replicare le funzioni cardiache. In seguito, i modelli paziente-specifici realizzati potrebbero essere utili per lo studio degli effetti di differenti interventi con lo scopo di predire trattamenti per le malattie cardiache.

Bibliografia

[1] A. J. Marelli, A. S. Mackie, R. Ionescu-Ittu, E. Rahme, L. Pilote. 2007. *Congenital heart disease in the general population: changing prevalence and age distribution*. Circulation 115: 163-172.

[2] M. E. Brickner, L. D. Hillis, R. A. Lange. 2000. *Congenital heart disease in adults. First of two parts*. N Engl J Med. 342: 256-263.

[3] M. E. Brickner, L. D. Hillis, R. A. Lange. 2000. *Congenital heart disease in adults. Second of two parts*. N Engl J Med 342: 334-342.

[4] S. Piran, G. Veldtman, S. Siu, G. D. Webb, P. P. Liu. 2002. *Heart failure and ventricular dysfunction in patients with single or systemic right ventricles.* Circulation 105: 1189-1194.

[5] A. Krishnamurthy, C. T. Villongco, J. Chuang, L. R. Frank, V. Nigam, E. Belezzuoli, P. Stark, D. E. Krummen, S. Narayan, J. H. Omens, A. D. McCulloch, R. C. P. Kerckhoffs. 2013. *Patient-specific models of cardiac biomechanics*. J Comput Phys 244: 4–21.

[6] S. Klotz, I. Hay, M. L. Dickstein, G. H. Yi, J. Wang, M. S. Maurer, D. A. Kass, D. Burkhoff. 2006. *Single-beat estimation of end-diastolic pressure-volume relationship: a novel method with potential for noninvasive application*. American Journal of Physiology – Heart and Circulatory Physiology 291 (1): H403–H412.

[7] R. C. Kerckhoffs, M. L. Neal, Q. Gu, J. B. Bassingthwaighte, J. H. Omens, A. D. McCulloch. 2007. *Coupling of a 3D Finite Element Model of Cardiac Ventricular Mechanics to Lumped Systems Models of the Systemic and Pulmonic Circulation*. Ann Biomed Eng 35: 1–18.

[8] R. C. P. Kerckhoffs, J. H. Omens, A. D. McCulloch, L. J. Mulligan. 2010. *Ventricular dilation and electrical dyssynchrony synergistically increase regional mechanical non-uniformity but not mechanical dyssynchrony: A computational model*. Circ Heart Fail 3 (4): 528–536.

[9] W. Kroon, T. Delhaas, P. Bovendeerd, T. Arts. 2009. *Computational analysis of the myocardial structure: Adaptation of cardiac myofiber orientations through deformation*. Medical Image Analysis 13: 346–353.

[10] F. Dorri , P. F. Niederer, P. P. Lunkenheimer. 2006. *A finite element model of the human left ventricular systole*. Computer Methods in Biomechanics and Biomedical Engineering 9 (5): 319-341.

[11] M. Pluijmert, P. H. Bovendeerd, W. Kroon. 2014. *Effects of activation pattern and active stress development on myocardial shear in a model with adaptive myofiber reorientation*. Am J Physiol Heart Circ Physiol 306: H538–46.

Chapter 1

Introduction

Cardiac malformations are the most common type of congenital defect, and affect approximately 1% of all newborns. Thanks to the progressive improvements in the management of complex congenital heart diseases (CHDs), currently more than 90% of CHD-affected children survive until the early adult age [1, 2]. Unfortunately, many of these patients, and particularly those affected by functional single ventricle or systemic right ventricle (RV), are at risk of ventricular dilatation and dysfunction with associated morbidity and mortality [3]. Often, even though on the long term, the final outcome is heart failure (HF), with leads to worse quality of life and shorter life expectancy [4]; however, the occurrence of HF is affected by the specific surgical treatment initially performed on the patient.

Nowadays, CHD management approaches are evolving relatively slowly; this process could be supported and accelerated by realistic *in-silico* analyses accounting for ventricular shape, intra-ventricular fluid dynamics, and wall electro-mechanics. Indeed, computational models of cardiac electro-mechanics (EM) are increasingly being considered in clinical applications as an additional modality to optimize therapies or understand therapy mechanisms.

Historically, the development of electrophysiology and mechanical models of cardiac function proceeded rather independently than in tandem. The vast majority of electrophysiology modeling studies ignored any effects due to mechanical deformation, and most mechanical modeling studies did not represent explicitly any electro-physiologic feedback on deformation [5]. More recently, though, multi-physics models that couple these two aspects have been developed [5, 6, 7], as it will be outlined in Chapter 3. These models can be used to study several applications, including the effects of different cardiac resynchronization therapies and of different surgical treatments [8, 9].

On this basis, the thesis project herein described was developed within one of the most active research groups in the computational modeling of cardiac electro-mechanics: the Cardiac Mechanics Research Group, headed by Prof. Andrew McCulloch at the Bioengineering Department of University of California San Diego. The project focuses on the development of patient-specific finite element models of the RV in a preliminary cohort of patients suffering from hypoplastic left heart syndrome. As it will be detailed in Chapter 4, setting these models requires a complex workflow prior to the final simulation of RV mechanics: acquisition and segmentation of tomographic images, generation of an

anatomically accurate computational grid [10], mapping of myo-fibers architecture [11], and identification of RV wall mechanical properties as well as of RV stress-free geometry based on hemodynamic data [8].

The primary goal of the project is to identify and statistically validate new model-derived parameters of ventricular shape and mechanics that may serve as early clinical markers for adverse remodeling and heart failure in adult HLHS patients. All these data, tools, models and results will be collected into the robust sharing infrastructure of the Cardiac Atlas Project. The Cardiac Atlas Project (CAP) is an international collaboration to establish a large-scale standardized database of cardiac imaging examinations and associated clinical data in order to develop a computational, structural and functional atlas of the normal and pathological heart [12]. These models and results will enable clinical and basic researchers to test new hypotheses, reanalyze archived data with new techniques, correlate structure and function with clinical data, and benchmark new techniques against existing results.

Chapter 2

Right ventricle anatomy and pathophysiology

2.1 Background

Understanding the anatomy and the role of the right ventricle in the pulmonary circulation is important to better study the pathology and the surgical treatments. This chapter first reviews the anatomy and physiology of the right ventricle, focusing on the normal dimensions and physiological pressure-volume values. Then, the HLHS pathology is described, together with surgical treatments developed over the years.

2.2 Anatomy and Physiology of the heart

The heart is the muscular organ that functions as the body's circulatory pump. In adults, the heart typically has a mass of 250–350 grams, and is the size of a closed fist: 12 cm in length, 8 cm wide, and 6 cm in thickness [13]. The heart is located between the lungs in the middle of the chest; its upper end, i.e. the base, is located at the level of the third costal cartilage, while the lower end, i.e. the apex, lies just to the left of the *sternum* between the junction of the fourth and fifth ribs near their articulation with the costal cartilages. A double-layered membrane called *pericardium* encloses the heart, with the aim to protect it and anchor it inside the chest (Figure 2.1).

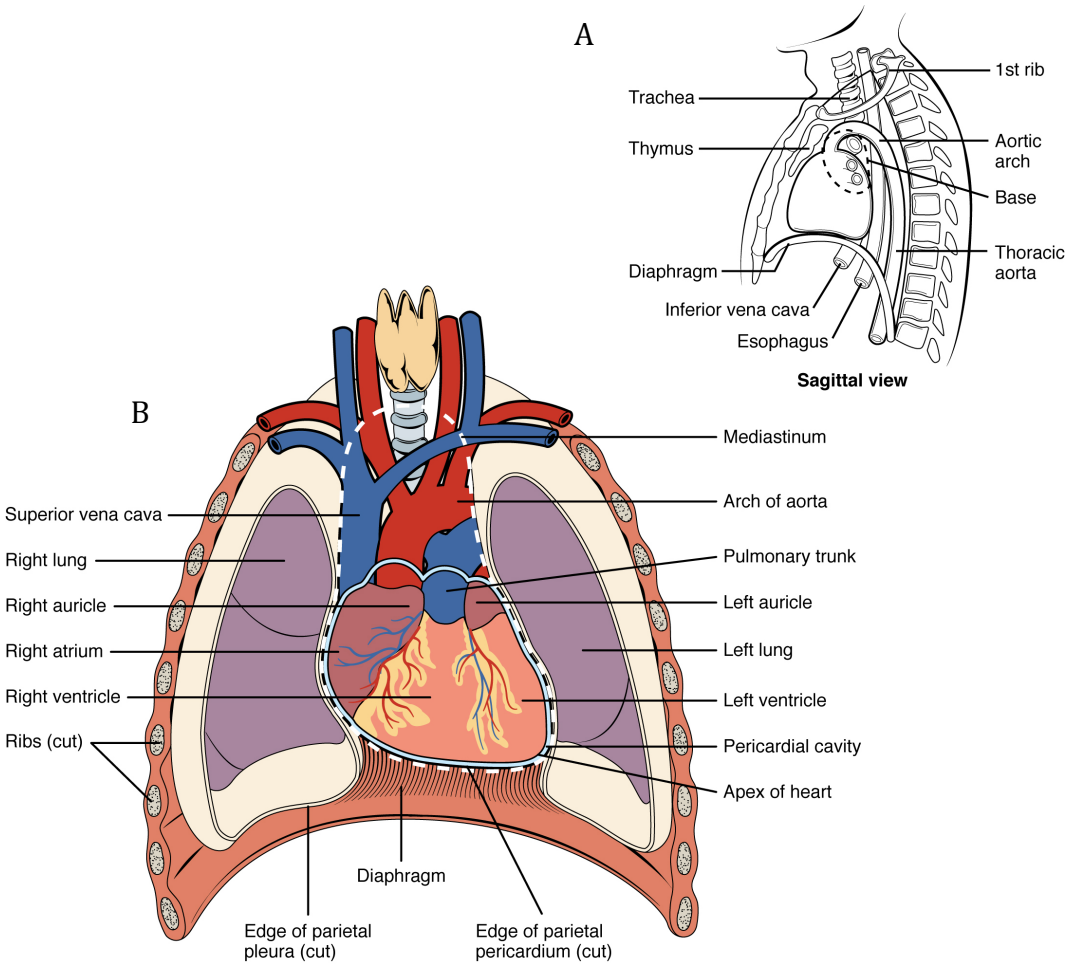

Figure 2. 1 - Position of the heart in the thorax. **A)** Sagittal view. **B)** Anterior view.

Internally, the heart itself is divided into two pumping units: the left heart and the right heart. From a hydraulic standpoint, these are two pumps in series, each one pumping blood though a tract of the circulatory system, i.e. the systemic and pulmonary circulation, respectively. Each unit consists of two chambers: an atrium and a ventricle. De-oxygenated blood returns to the right atrium via the venous circulation, it is pumped into the right ventricle and then to the lungs where carbon dioxide is released and oxygen is absorbed. Oxygenated blood then travels back to the left side of the heart into the left atria and then into the left ventricle, from where it is pumped into the aorta and into the arterial systemic circulation. The unidirectional blood flow through the heart is allowed for by the presence of four valves. Two out of these are located between the atria and the corresponding ventricles; these valves are called mitral and tricuspid in the left and right heart, respectively. The remaining two valves separate the ventricles from the corresponding outflow arteries; these valves are called aortic and pulmonary valve in the left and right heart, respectively (Figure 2.2).

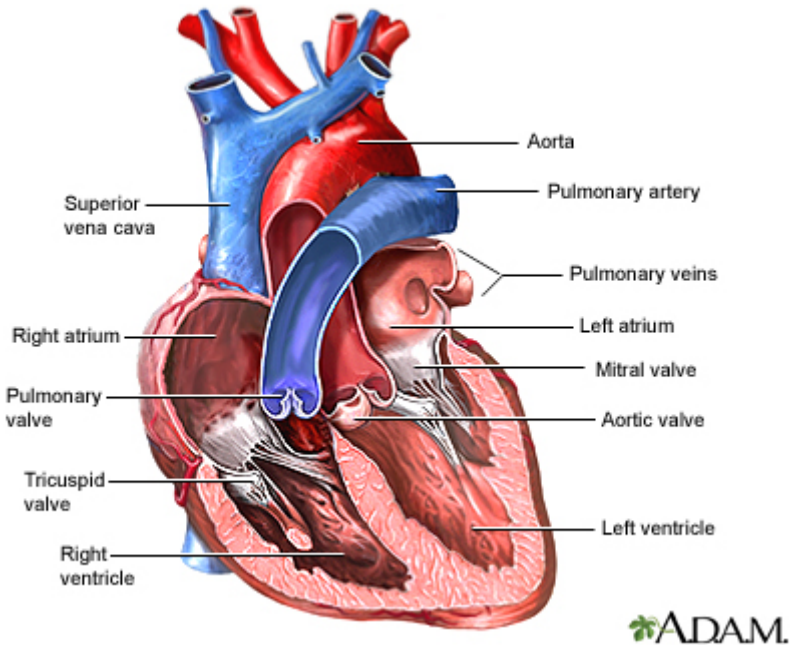

Figure 2. 2 – Heart valves location within the heart.

The heart wall is made of 3 layers: epicardium, myocardium and endocardium (Figure 2.3). The *epicardium* is the outermost layer of the heart wall; it is a thin layer of serous membrane that helps lubricating and protecting the outside of the heart. The *endocardium* is the innermost layer of the wall and consists of smooth endothelium; it plays a key role in

the interaction between the cardiac wall and the blood in the heart chambers, in that it prevents from cloth formation and is responsible for the mechano-transduction of wall shear stresses. The *myocardium* is the middle layer of the heart wall and mostly consists of muscular tissue; it is the thickest layer in the heart wall and plays the key role in heart pumping function.

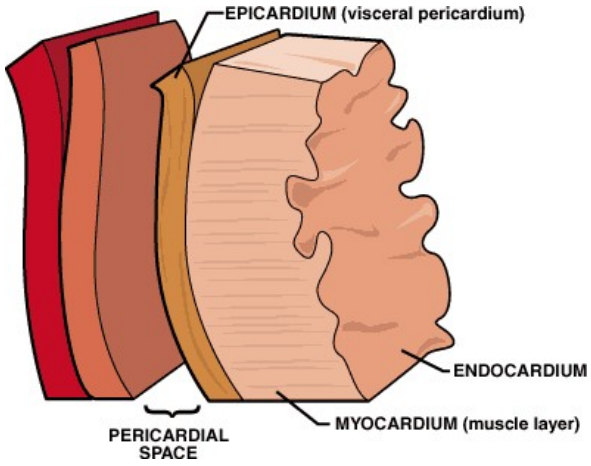

Figure 2. 3 – Pericardial membranes and layers of the heart wall.

The thickness of the *myocardium* is heterogeneous. First, it varies among the four heart chambers. The atrial wall is very thin: blood moves from the atria into the ventricles mostly driven by gravity, since only the blood minimal energy loss across the atrioventricular valves has to be compensated for in this process. The ventricular wall is thick, and is thicker in the left ventricle than in the right one. Indeed, ventricles pump blood into the corresponding portions of the arterial bed, and hence have to pressurize blood so to compensate for the large distributed energy loss associated to the hydraulic impedance of the systemic and pulmonary circulation, respectively. Moreover, wall thickness varies within each heart chamber; for example the left ventricle wall is thinner at the apex and thicker at the base. A simple explanation for this heterogeneity is provided by the pressurized thin-walled shells theory, which allows for relate the stresses in the wall to the fluid pressure in the shell and to the wall thickness and radius of curvature. This theory explains that, for a given pressure value, stresses increase with the wall radius of curvature and decrease with wall thickness. Hence, at the ventricular apex, where the wall radius of curvature is short, the wall is thinner as compared to the base region, where the wall radius of curvature is higher.

The heart pumping activity is cyclic, and is carried out through two basis phases in each cycle (Figure 2.4): diastole and systole. In diastole blood passively flows from the atria to the ventricles, which are relaxed. In systole the ventricular wall actively contracts and blood is ejected into the aorta and pulmonary artery from the left and right ventricle, respectively.

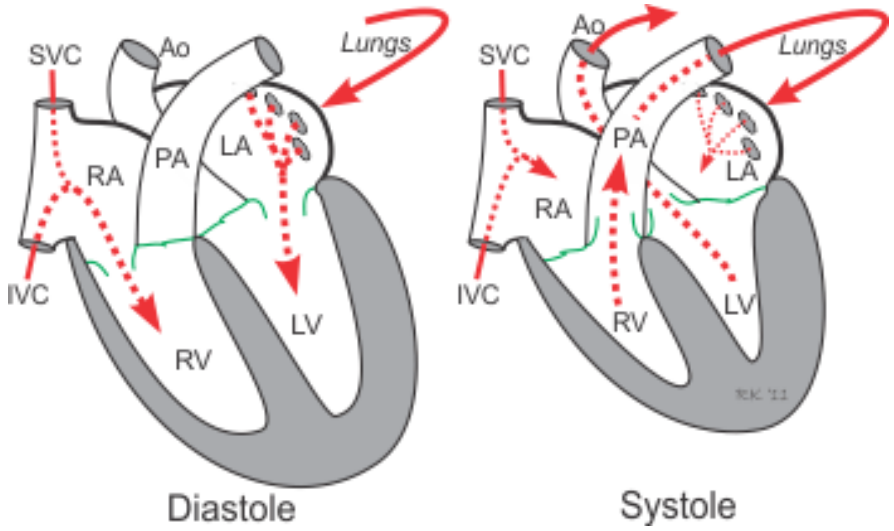

Figure 2. 4 – The two phases of the cardiac cycle. During diastole, the blood flows through atrio-ventricular valves (mitral and tricuspid) that separate the atria from the ventricle. During systole, the aortic and pulmonic valves open to allow for ejection into the aorta and pulmonary artery.

2.2.1 The right ventricle

In 1616, Sir William Harvey was the first to describe the importance of the right ventricular function [14].

The right ventricle (RV) in the normal heart is the most anteriorly situated cardiac chamber, since it is located immediately behind the sternum. The pulmonary and tricuspid valves mark its superior and right margin, respectively.

In contrast to the near conical shape of the left ventricle (LV), the RV is more triangular in shape when viewed from the front and it curves over the left ventricle. Its shape is also influenced by the position of the inter-ventricular septum (Figure 2.5).

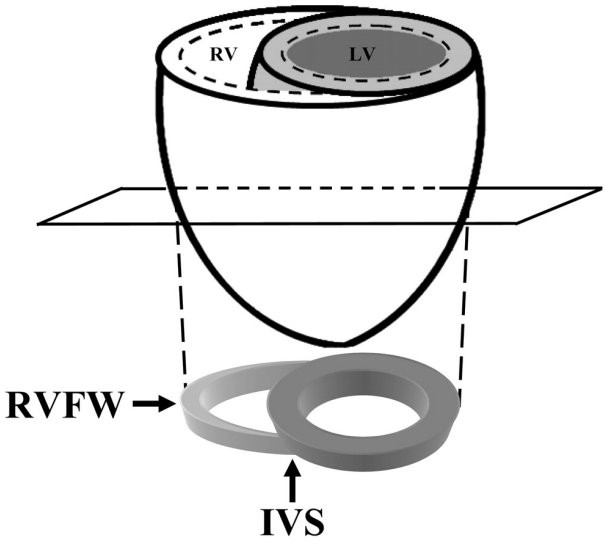

Figure 2.5 – Right and left ventricular geometry. RVFW = Right Ventricular Free Wall, IVS = Inter-Ventricular Septum.

The primary function of the RV is to receive systemic venous return and to pump it into the pulmonary arteries. Under normal circumstances, the RV is connected in series with the LV and is, therefore, obligated to pump on average the same effective stroke volume but with 25% of the stroke work because of the low impedance of the pulmonary vasculature. As compared to the systemic circulation, the pulmonary circulation has a much lower vascular resistance, greater pulmonary artery distensibility, and a lower peripheral pulse wave reflection coefficient [15, 16]. Under normal conditions, right-sided pressures are significantly lower than comparable left-sided pressures. Therefore, based on the Laplace relationship, the RV is thin walled and compliant [4].

Normal pressure-volume loop during the cardiac cycle, as well as the pressure and volume curves over time, are shown in Figure 2.6.

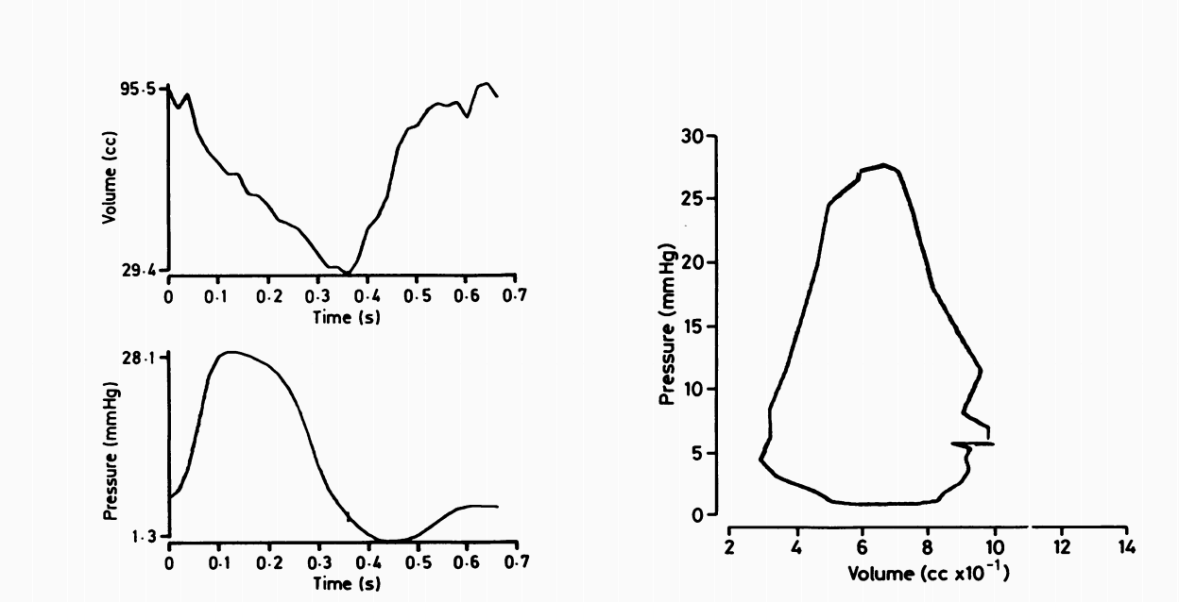

Figure 2.6 – Normal right ventricular pressure-volume relation obtained using biplane angiography and simultaneous micromanometer pressure measurements [17]. **On the left:** plots showing right ventricular volume and pressure curves. **On the right:** normal right ventricular pressure-volume loop.

The cavity of the chamber can be subdivided into three regions [18]: (1) the inlet, which consists of the tricuspid valve, chordae tendineae, and papillar muscles, (2) the trabeculated apical myocardium, (3) the infundibulum, which corresponds to the smooth myocardial outflow region.

In all hearts, the second region allows for the direct morphologically-based distinction between the RV and the LV; the muscular trabeculations in the apical part of the RV are coarser than those in the LV.

As described by Ho and Nihoyannopoulos [19], the RV wall is composed of multiple layers that form a 3-dimensional (3D) network of fibers. The superficial or sub-epicardial myofibres are arranged more or less circumferentially in a direction that is parallel to the atrio-ventricular groove. The deep myofibres are longitudinally aligned, apex to base (Figure 2.7). In the normal heart, the myocardial wall of the RV not including trabeculations is 3–5 mm thick. In this relatively thin wall circumferential and longitudinal orientations predominate.

In contrast, the thicker LV wall contains obliquely arranged myofibres superficially, and longitudinal myofibres in the subendocardium, but these sandwich predominantly circular myofibres inbetween.

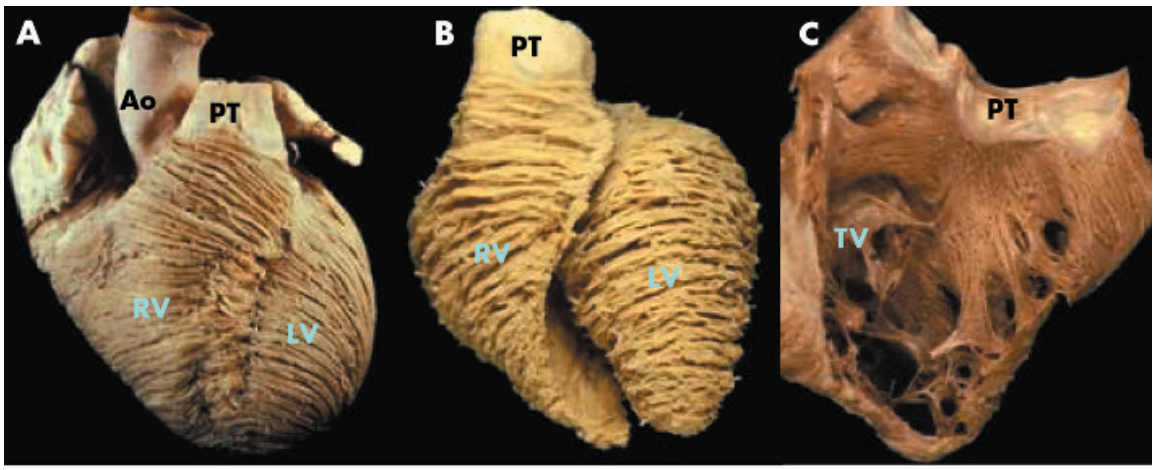

Figure 2. 7 – (A) A normal heart viewed from the front shows the circumferential to oblique arrangement of the myofibres in the subepicardium. **(B)** Myofibres lying deeper than the subepicardium retain the circumferential arrangement in the right ventricle but change from oblique to circumferential in the left ventricle. **(C)** The right ventricle is opened to show the longitudinally arranged subendocardial myofibres.

In the human ventricle the muscle fiber angle, usually defined as the angle between the fiber axis and the transverse plane cutting the ventricle, makes a smooth transmural transition from epicardium to endocardium. There are also small changes in fiber orientation from end-diastole to systole (7-19°), with greatest changes at the epicardium and apex [19].

2.3 Congenital Heart Disease

Congenital heart disease (CHD) is a category of heart defects that includes abnormalities in cardiovascular structures that occur before birth. The defects can involve the structure of the heart and/or great vessels. CHD happen because of incomplete or abnormal development of the fetus heart during the very early weeks of pregnancy, and its cause is still unknown.

The number of children affected by CHD doubled since 1985 to 2000 ad this will increase adult rates. Advances in pediatric care have resulted in improved long-term survival of these pediatric patients, and in an increasing number of adults with CHD. In U.S. there are now more adults with CHD than children and the rate is estimated to be increasing of about 5% per year [2, 20].

Common types of CHD are:

- Atrial Septal Defect (6-10%): there is a “hole” in the wall (septum) between the two atria. Blood from pulmonary veins enters in the left atrium and then it crosses the ASD into the right atrium and ventricle [2].
- Ventricular Septal Defect (14-17%): it is the most common congenital cardiac abnormality in children and it consists of a “hole” in the wall between the two ventricles. Blood can travel across the hole from the left ventricle to the right ventricle and out to the lung arteries [2].
- Patent Ductus Arteriosus (5-10%): the ductus arteriosus connects the descending aorta to the left pulmonary artery. In the fetus it permits blood to bypass the lungs and to get oxygenated in the placenta. When the baby is born this hole is supposed to close but in some infants it does not close spontaneously and there is continuous flow from the aorta to the pulmonary artery [2].
- Aortic/Pulmonary Valve Stenosis (8-15%): the valve does not open and close properly so when the blood flowing out from the heart is trapped by a poorly working valve [2].
- Coarctation of the Aorta (6-8%): It is a narrowing of the major artery that carries blood to the body [2].
- Single Ventricle (30-40%): They are rare disorders affecting one lower chamber of the heart; the chamber may be smaller, underdeveloped, or missing a valve. They include Hypoplastic Heart Left Syndrome (HLHS), Pulmonary Atresia (PA), and Tricuspid Atresia (TA).
- Tetralogy of Fallot (7-10%): It is a cyanotic heart defect that is characterized by a large VSD, an aorta that overrides the left and right ventricles, pulmonary stenosis, and RV hypertrophy [3].
- Ebstein’s Anomaly (less than 1%): It is a defect of a tricuspid valve in which the septal leaftlets are displaced into the RV and the anterior leaflet is abnormally attached to the RV free wall [3].
- Transposition of the Great Arteries (5-7%): In the D-ToGA, aorta and pulmonary artery are reversed, therefore there is a complete separation of the pulmonary and systemic circulation. In the L-ToGA the right and left lower chambers of the heart are switched [3].

- Eisenmenger's Syndrome (4-5%): There is a large left-to-right shunt that causes severe pulmonary vascular disease and pulmonary hypertension, with resultant reversal of the direction of shunting [3].

Sign and symptoms are related to type and severity of the heart defect and often CHD are associated with an increased incidence of some other symptoms.

2.3.1 Hypoplastic Left Heart Syndrome

Single ventricle (SV) refers to a group of congenital heart defects in which the heart has only one pumping chamber. The latter ventricle has to pump blood both in the pulmonary and the systemic circulations, and thus has to counteract an abnormally increased afterload. Also, the oxygenated blood returning from the lungs mixes with the de-oxygenated blood returning from the systemic veins and this affects the blood saturation, thus hampering the oxygen supply to the peripheral organs (Figure 2.8). Hence, the infant can become cyanotic with insufficient blood flow to the lungs and inadequate oxygen supply to the body.

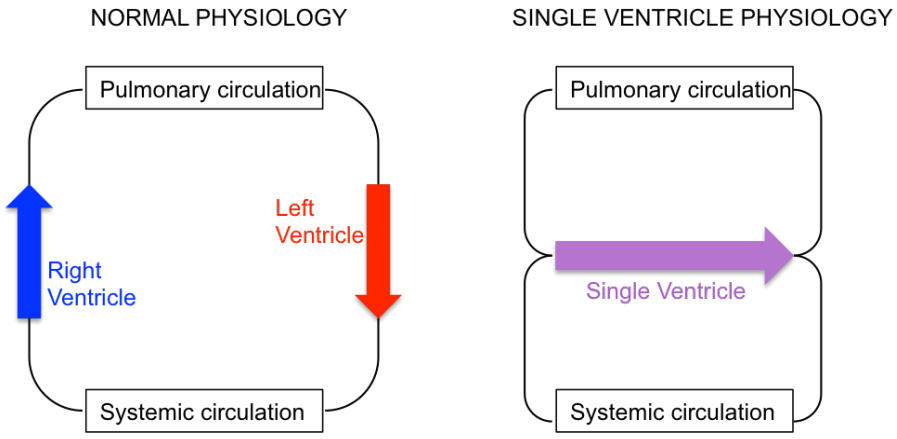

Figure 2. 8 – Schematic showing a normal and single ventricle heart physiology. In normal heart both ventricles work in parallel while there is a serial connection in single ventricle hearts.

The Hypoplastic Left Heart Syndrome (HLHS) is a SV defect characterized by underdevelopment or absence of the left ventricle. It was first described by Lev in 1952 [20] and named in 1958 by Noonan and Nadas [21]. It has been reported that each year

approximately 640 to 1440 infants in the United States are born with HLHS [22]. The 15% of neonates die on the first day of life, the 70% during the first week and 91% within 30 days [23].

HLHS usually includes hypoplasia of the left ventricle and ascending aorta, mitral and aortic valve atresia or stenosis (Figure 2.9).

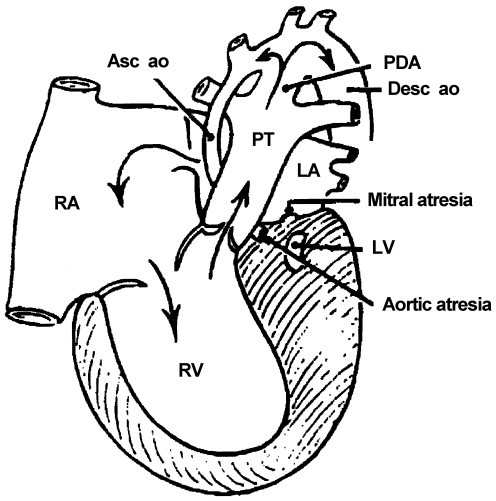

Figure 2. 9 – Illustration of the HLHS. The hypoplastic left ventricle is associated with aortic and mitral atresia.

The growth impairment between left and right ventricle is caused by a perturbation of flow into or out of the LV during fetal life. In fact it has been observed that fetuses with HLHS has a smaller *foramen ovale* than fetuses with a physiological heart [24]. Figure 2.10 shows that the LV initially appears dilated, larger than the RV, and poorly contractile; then it becomes hypoplasic.

In fetal life, the communication between systemic and pulmonary circulation is guaranteed by *foramen ovale* and ductus arteriosus. If one ventricle is hypoplasic, the contralateral one can compensate allowing for the development of all the other organs. After birth, it is necessary to maintain the patency of the ductus arteriosus with an intravenous prostaglandin E1 infusion before proceeding to surgery or to heart transplantation.

The major limitations of transplantation are the shortage of donors and the difficult size matching between donor and recipient. Also, management during the waiting period can be challenging.

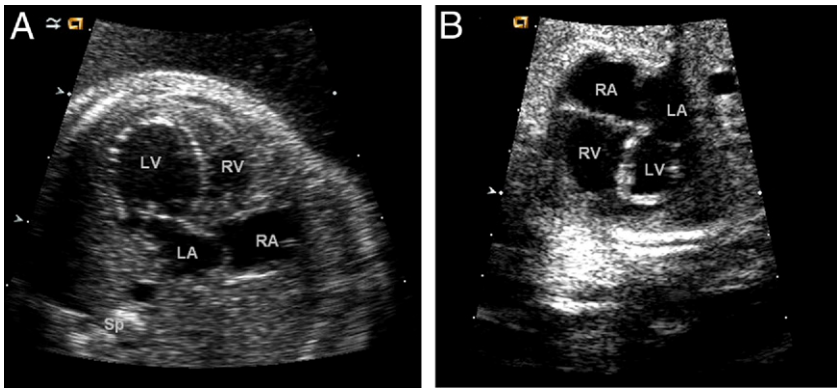

Figure 2. 10 – Four-chamber view of a fetal echocardiogram: **A)** At 22 weeks. The LV is dilated an larger than the RV. **B)** At 33 weeks. The LV has become hypoplasic.

2.3.2 Surgical treatments for HLHS

The overall goal of the correction techniques of the CHD is obtaining a physiologically normal circulation, with a biventricular heart. However, in patients with SV that is not possible. Surgical techniques developed over the years have tried to bypass, first partially and then completely, the failing portion of the heart, connecting the systemic venous return directly to the pulmonary arterial flow [25].

In the mid-40s was developed a palliative procedure to connect the pulmonary arteries to systemic arteries [26]: this gave rise to a series of experimental procedures with the purpose to develop the best surgical solutions for the SV treatment.

Nowadays, surgical treatment of HLHS through the Fontan procedure is the gold standard.

The original Fontan procedure (Figure 2.11), implemented for the first time in 1971 for the treatment of tricuspid valve atresia [27], was intended to bring together the blood coming from the cava veins to the pulmonary arteries, resulting in the connection in series of the systemic and pulmonary circulation.

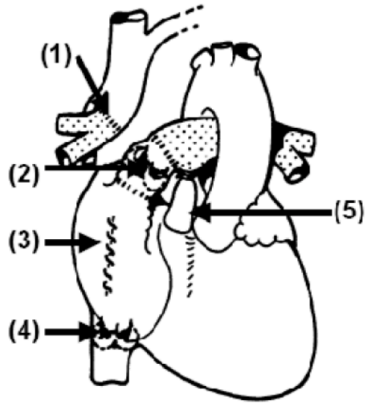

Figure 2. 11 – Original Fontan procedure. **(1)** End-to-side anastomosis of the distal end of right pulmonary artery to Superior Vena Cava. **(2)** End-to-end anastomosis of the right atrial appendage to proximal end of right pulmonary artery by means of an aortic valve homograft. **(3)** Closure of atrial septal defect. **(4)** Insertion of a pulmonary valve homograft into Inferior Vena Cava level with right atrium. **(5)** Superior Vena Cava is transected at its entry into right atrium and main pulmonary artery is ligated. [27]

Over the years there have been made many changes to the Fontan technique, to overcome the valve stenosis problems and damage to the duct caused by the presence of a valve in the Inferior Vena Cava (IVC), found in the first interventions.

Today, the Fontan procedure is a three-staged surgery (Figure 2.12) performed starting from few days after birth.

1. Norwood procedure: it consists in the construction of an unobstructed systemic blood flow from the RV to the aorta and a restricted pulmonary flow through a systemic to pulmonary shunt. The shunt can be from the innominate or subclavian artery to the pulmonary arteries (Blalock-Taussig shunt), from the aorta to the pulmonary arteries (Central shunt) or from the right ventricle to the pulmonary arteries (Sano shunt).
2. Hemi-Fontan or Glenn procedure: the goal of this stage is the connection of the superior vena cava (SVC) to the undivided pulmonary arteries to decrease the blood flow that goes from the right atrium to the RV. The shunt is removed.
3. Fontan procedure: this is the last step; also the inferior vena cava (IVC) is connected to the undivided pulmonary arteries. In this way, the RV pumps oxygenated blood through a reconstructed aorta and venous blood returns directly to the lungs.

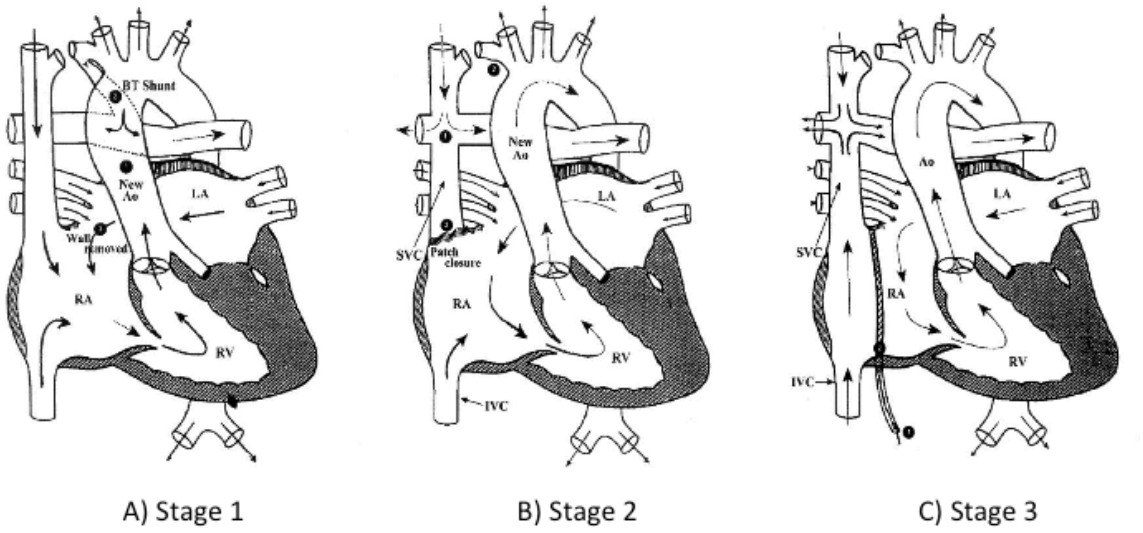

Figure 2. 12 – Illustration of the three-staged surgery. **A)** Norwood procedure. **B)** Hemi-Fontan procedure. **C)** Fontan procedure.

According to literature, the perioperative survival rates range from 47% to 85% for the Norwood operation [28, 29], from 94% to 98% for the following stage, and from 86% to 94% for the Fontan procedure [28, 30, 31].

2.4 Cardiac magnetic resonance imaging

HLHS children are usually monitored using cardiac magnetic resonance imaging (cMRI). In particular cMRI is performed to help physicians detect or monitor the disease by:

- evaluating the anatomy and function of heart chambers and valves, as well as blood flow;
- planning patient's treatment;
- monitoring the progression of the pathology over time.

Magnetic resonance imaging (MRI) is a non-invasive medical tool that uses a powerful magnetic field, radio frequency pulses, and a computer to produce detailed pictures of organs, soft tissues, bone, and virtually all other internal body structures (Figure 2.13). MRI does not use ionizing radiation (x-rays).

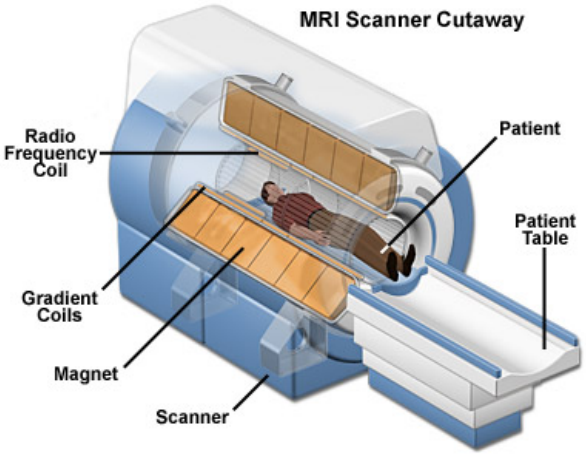

Figure 2. 13 – Scheme of the Magnetic Resonance. It makes use of the property of Nuclear magnetic resonance (NMR) to image nuclei of atoms inside the body.

A contrast agent, such as gadolinium, might be injected into a vein during cMRI; the substance travels to the heart and highlights the heart and blood vessels on the MRI pictures.

Compared with other techniques, MRI gives the chance to study the complex geometry of the heart considering also its orientation with the body longitudinal axis.

Three type of view are used (Figure 2.14) for tracking the geometry of left and right ventricles and atria.

- Vertical long axis (two chambers): This view takes in consideration the axis parallel to interventricular septum. The operator can choose to obtain images of the two chambers of the right or left heart, useful above all for the assessment of the apex and the anterior ventricular wall.
- Horizontal long axis (four chambers): This view is on a long axis perpendicular to interventricular septum, it shows the four chambers at the same time. It is useful to evaluate the apex of the ventricle and septal and lateral walls, the right ventricular free wall, and chamber size.
- Short axis: This view is perpendicular to both the axis considered previously. Generally at least three plan on the short axis are acquired, one under the submitral valve level, the second on traspapillary level and the last on periapical level. This view is used for volumetric measurements.

Long axis and short axis views may be combined to get a more exhaustive description of ventricular geometry, producing a 3D model of the area of interest.

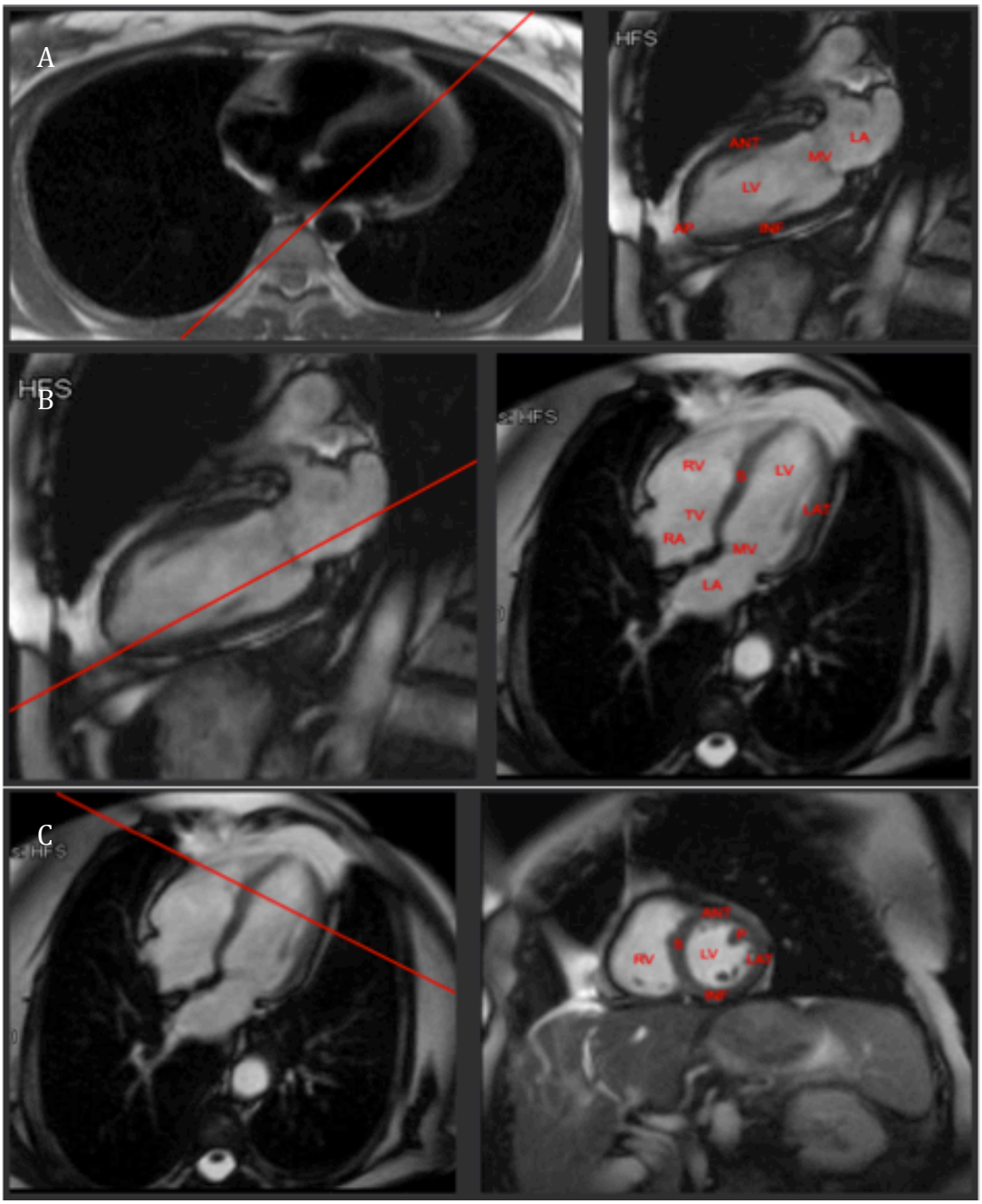

Figure 2. 14 – Cardiac MRI: **A)** Vertical long axis view; **B)** Horizontal long axis view; **C)** Short axis view. In all the three view the red line in the figure on the left represents the plane through which the image on the right is obtained. (ANT=Anterior wall; INF=Inferior wall; LAT=Lateral wall; S=Septum; LA=Left Atrium; LV=Left ventricle; RA=Right atrium; RV=Right ventricle; AP=Apex; MV=Mitral valve; TV=Tricuspid valve; P=Papillary muscle).

The acquisition sequence is usually triggered by an on-line ECG. Images are acquired at a given ECG phase and then averaged to increase the signal-to-noise ratio. With this method a lot of information regarding the dynamic of the heartbeat can be lost. To overcome this problem, in the last couple of years, MR research has come up with real-time magnetic resonance. Cine images are short movies that are able to show heart motion throughout the cardiac cycle. By coordinating the fast gradient-echo MRI sequence with retrospective ECG-gating, numerous short time frames evenly spaced in the cardiac cycle are produced. These images are laced together in a cinematic display so that wall motion of the ventricles, valve motion, and blood flow patterns in the heart and great vessels can be visualized.

Chapter 3

State of the art

3.1 Background

The combination of computational models and biophysical simulations can help interpreting an array of experimental data and contribute to the understanding, diagnosis and treatment of complex diseases such as cardiac arrhythmias. For this reason, three-dimensional (3D) cardiac computational modeling is currently a rising field of research. The advance of medical imaging technology over the last decades has allowed for the evolution from generic to patient-specific 3D cardiac models that faithfully represent the anatomy and different *in vivo* cardiac features of a given subject.

This chapter reviews the current state of the art in the numerical modeling of cardiac mechanics and electro-mechanics. In this overview, the key aspects of such models will be emphasized: i) the realistic description of geometry and structure of the myocardium (3D model), ii) the continuum balance law and the boundary conditions, and iii) the constitutive equations to describe the material properties of the myocardium.

3.2 Patient-specific cardiac modeling

3.2.1 Cardiac 3D geometry reconstruction and discretization

First step of the 3D cardiac model development is the complex anatomy reconstruction.
In early models, 3D geometries were simplistic, based on idealized shapes and mostly including only the left ventricle (LV) [32, 33]. Among these models, the one including the most quantitative information was based on canine heart anatomy [32], and described the LV as a thick ellipsoid of revolution truncated at the base (Figure 3.1). Hence, LV geometry in the dog can be defined by the major and minor radii of two surfaces, which define the LV endocardium, and the free wall epicardium together with the septal endocardium of the right ventricle, respectively.

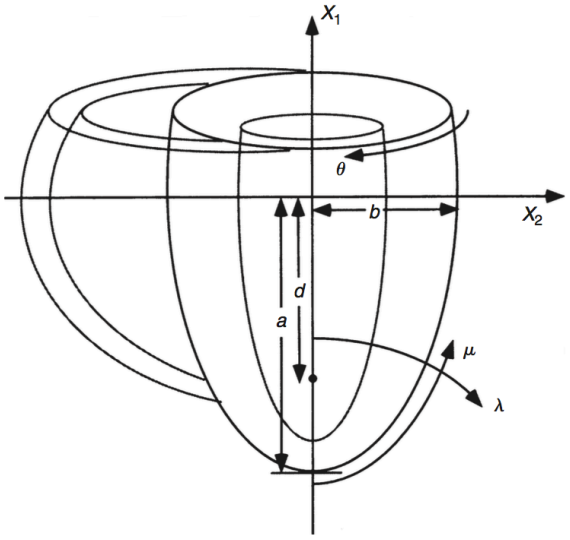

Figure 3. 1 – Truncated ellipsoid representation of ventricular geometry, showing major left ventricular radius (a), minor radius (b), focal length (d) and prolate spheroidal coordinates (lambda, mu, theta).

Subsequent models accounted more realistically for the cardiac anatomy. However, being based on poor quality data, these models did not capture fine anatomical details. The two most representative examples of this generation of models are the two bi-ventricular models developed at the University of California San Diego, based on rabbit hearts, [33] and at the University of Auckland, based on canine data [32]. The main innovation of these two models consisted in realistically capturing the spatial orientation of myocardial fibers based on experimental measurements.

Over the last 15 years, the evolution of medical imaging technologies, such as magnetic resonance imaging (MRI) and computed tomography (CT), gave the possibility of building realistic 3D cardiac models based on either *in vivo* or *ex vivo* images. In particular, the increasing availability of *in vivo* cardiac images resulted in the definition of patient-specific models, whose geometry fits the endocardial and epicardial contours traced on medical images. Building this kind of model requires imaging techniques synchronized with the ECG and breathing in order to overcome the noise and motion arte- facts due to the cardiac cycle and breathing movements. This has also enabled building dynamic models that include the intra-subject anatomical variations of the heart due to the cardiac cycle [34,35].

Cardiac atlases also emerged thanks to the increasing availability of in-vivo images. They are assembled by averaging several 3D cardiac image datasets from a population of subjects, thus generating a mean 3D cardiac image or shape.

A relevant aspect of geometrical modeling is the discretization of the 3D domain for the subsequent numerical analyses. In models aimed to simulating the mechanics of the myocardial wall, the latter is discretized into hexhaedrals or tetrahedric elements, often of high order. An example of mesh fitting is provided by the work by Krishnamurthy et al. [8]. Hexahedral cubic-Hermite finite element meshes of the ventricular geometries for each patient and the explanted host heart were constructed from the clinical and non-clinical image data. Endocardial and epicardial contours (left ventricle, right ventricle, septum, and epicardium) of the patient hearts at end-diastole were manually segmented from the CT images. (See Appendix A for cubic Hermite mesh).

Aguado-Sierra et al. [9] used a similar approach starting from Echo images. They modeled the ventricular geometry with prolate-spheroidal coordinates, and fitted surface measurements using least square optimization of only the transmural coordinate interpolated with high-order bicubic-Hermite elements.

In Figure 3.2 a schematic view of the 3D cardiac geometry generation process.

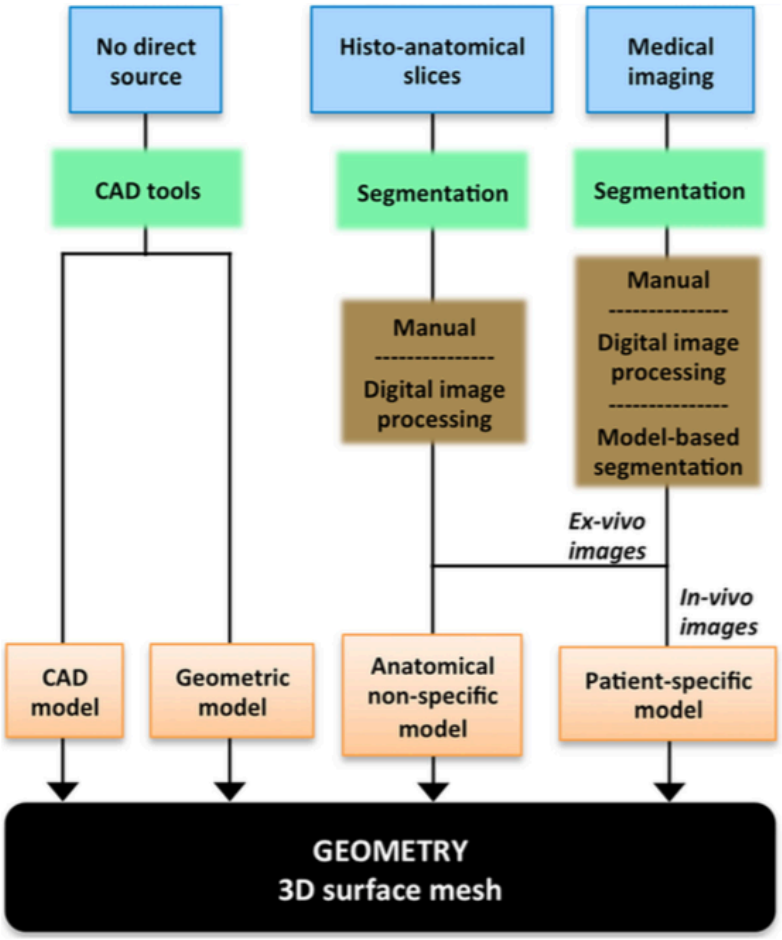

Figure 3. 2 – 3D cardiac geometry generation stage of the development process of a 3D cardiac computational model. Diagram depicting the main alternatives to generate the 3D surface mesh that represents the cardiac geometry, showing the sources of anatomical information (blue) and the methods (green) with their possible options (brown) used for this task, as well as the kind of model (orange) obtained by each method.

To perform realistic electrophysiology and/or mechanical computational simulations, the space-dependent organization of myofibres in the bulk of the LV wall has be modeled. In particular, the local orientation of myofibres must be defined in every mesh element. Figure 3.3 shows the methods to get fiber orientation. To this aim, two main strategies have been adopted, as schematized in Figure 3.3. The most common approach consists in applying pre-established paradigmatic patterns that define local myofibres orientation based on the position of the element with respect to reference points in the heart [34-36].
The alternative approach consists in reconstructing the patient-specific spatial organization of myofibres based on diffusion tensor-MRI (DT-MRI). It is a MRI modality capable of showing the diffusion of water molecules within the biological tissues, which is an

anisotropic phenomenon in tissues organized as fiber bundles. The principal direction for water diffusion in the myocardium can be used as a surrogate for the local mean myofibres direction. Krishnamurthy and colleagues used this approach, combined with large deformation differomorphic mapping, in order to account for differences among patients [8]. Diffeomorphic transformations are smooth one-to-one mappings of one anatomical model domain to another that preserve geometric features. Smoothness and bijectivity ensure that contours remain contours, surfaces remain surfaces, and volumes remain volumes through the transformation.

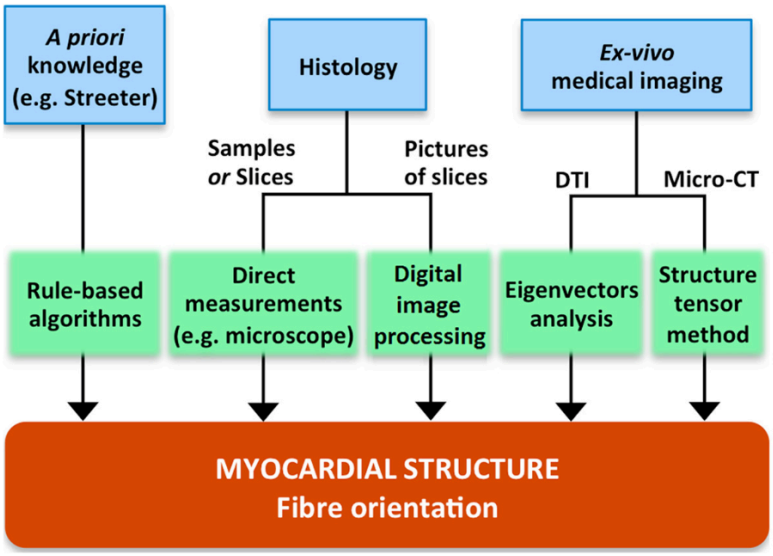

Figure 3. 3 – Possible approaches to the modeling of myocardial structure. In blue the main sources of structural information at tissue level, and in green the methods used to obtain the fiber orientation.

3.2.2 Passive material properties and Unloaded geometry

The typical approach to the modeling of the stress-strain behavior of myocardial tissue consists in superimposing the passive mechanical properties of the tissue to the effects of its active contraction.

As regards passive mechanical properties, these are modeled through finite strain elasticity or hyperelasticity, so to account for large deformations and non-linear stress-strain behavior. Hence, constitutive models are based on the concept of strain energy function, which expresses the elastic energy per unit volume stored by the material throughout a

deformation process as a function of strains. Stresses within the material can then be computed as derivatives of the strain energy function with respect to strains.

In literature a number of constitutive models have been proposed.

Some authors [35, 37-40] described the material as a transversely isotropic, where the strain energy function contained four, five, or six material parameters obtained from biaxial tests [41-43].

Later, new models were implemented [44, 45] in which the myocardium was considered as an orthotropic material with at least seven material parameters. This class of models is well represented the model by Holzapfel & Ogden [46], which assumed the following strain energy function:

$$\psi = \frac{a}{2b} exp[b(I_1 - 3)] + \sum_{i=f,s} \frac{a_i}{2b_i} \{exp[b_i(I_{4i} - 1)^2] - 1\} + \frac{a_{fs}}{2b_{fs}} \left[\exp\left(b_{fs} {I_{8fs}}^2\right) - 1\right] \qquad (1)$$

Where a, b, a_{f}, a_{S}, b_{f}, b_{S}, a_{fS} and b_{fS} are eight positive material constants, the a parameters having dimension of stress, whereas the b parameters are dimensionless. The strain energy ψ consists of four terms. The first one depends I_1, i.e. first invariant of the right Cauchy-Green tensor $\boldsymbol{C}$, and accounts for the isotropic part of the mechanical response associated to the non-collagenous and non-muscular matrix in the tissue. The second and third terms depend on I_{4f} and I_{4s}; these are the fourth pseudo-invariants of $\boldsymbol{C}$ associated to the myofibres direction and to the cross-fiber direction in a sheet, or layer, of myocardium. I_{4f} and I_{4s} quantify the stretch of the material in these two directions; hence the second and third term of the strain energy function superimpose two transversely responses, whose respective main direction are mutually orthogonal, thus obtaining orthotropy. These two terms allow for correctly capturing the effects of normal tensile or compressive strains. The fourth term depends on I_{8fs}, which is the eighth pseudo-invariant of $\boldsymbol{C}$ and accounts for shear in the myocardial layer.

It is worth noting that the above described strain energy function does not account for pre-strains nor pre-stresses. Hence, it should be combined to the stress-free configuration of the studied system in order to yield a correct quantification of stresses. However, when modeling ventricular mechanics based on medical imaging it not possible to directly reconstruct the stress-free geometry of the ventricles corresponding to a zero pressure load.

This configuration hence should be identified starting from the one obtained from medical imaging, which usually corresponds to end-diastole.

Indeed, some previous studies have neglected this issue, assuming the ventricle to be unloaded either at end-systole, as in Walker et al. [47], or at mid-diastole, as in Sermesant et al. [48].

Klotz et al. [49] proposed an empirical approach to estimate the unloaded reference volume and the end-diastolic pressure-volume relationship (EDPVR). Early studies [50] have shown that the EDPVR can be described by a nonlinear analytical expression (with different coefficient values):

$$EDP = \alpha EDV^{\beta} \tag{2}$$

In his paper, Klotz tested the hypothesis that the EDPVR normalized could be described with a single universal set of parameter values (A_n, B_n) and predicted from a single point on the curve.

The procedure starts with the measurement of EDP and EDV on a single beat (P_m and V_m). The normalized measured volume is defined as:

$$V_{m,n} = \frac{(V_m - V_0)}{(V_{30} - V_0)} \tag{3}$$

Where V_{30} is the ventricular volume corresponding to a 30 mmHg pressure.

$$V_{30} = V_0 + (V_{m,n} - V_0)/(\frac{P_m}{A_n})^{\frac{1}{B_n}} \tag{4}$$

To predict the EDPVR, a reasonable estimate of V_0 is required. The volume of 80 explanted human hearts was measured at pressure values of 10, 15, 20, and 25 mmHg. These were separately plotted versus the V_0. Then, the linear regression equation was determined and Equation 5 was obtained.

$$V_0 = V_m(0.6 - 0.006\, P_m) \tag{5}$$

The entire EDPVR of an individual heart can then be predicted from analytical determination of α and β to force the curve through the measured point on the EDPVR and the predicted V_0 and V_{30}.

$$\beta = \frac{Log(P_m/30)}{Log(V_m/30)} \tag{6}$$

$$\alpha = 30/(V_{30}{}^{\beta}) \tag{7}$$

Based on the equation (5), Krishnamurthy et al. [8] developed an algorithm to find the unloaded geometry of the ventricle. It is based on an iterative estimation scheme that minimizes the difference between the measured end diastolic geometry and the computed geometry when the unloaded model is inflated to the measured end-diastolic pressure (Figure 3.4).

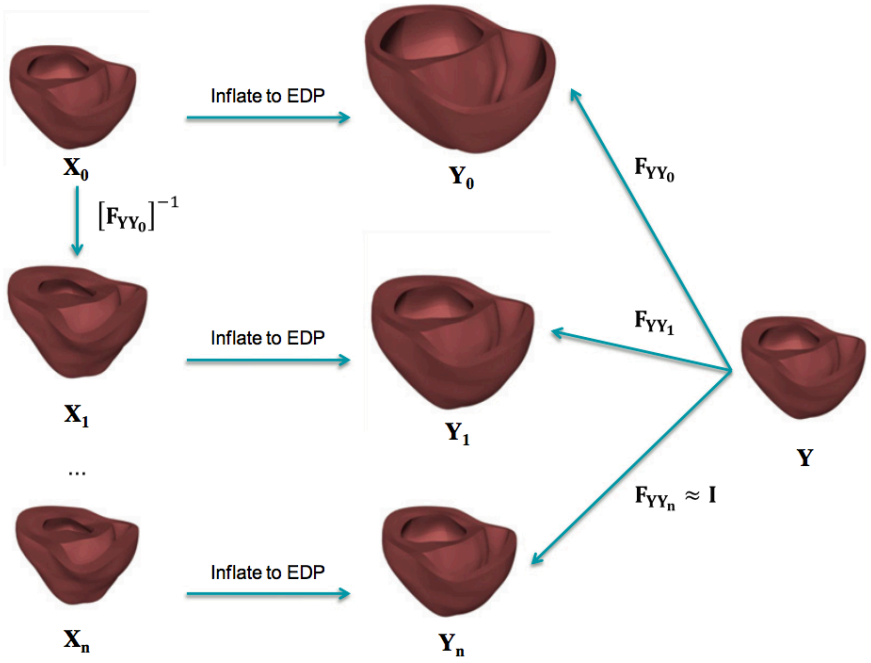

Figure 3. 4 – Algorithm to find the unloaded geometry. The initial geometry X0 is first inflated to the measured end-diastolic pressure. The deformation gradient between the inflated mesh (Y0) and the fitted end-diastolic (Y) is computed. This is applied inversely to X0 to get a new unloaded geometry estimate. The process is iterated until the projection error between the surfaces of the measured and loaded geometries is lower than the fitting error.

3.2.3 Active material parameters

The myocardium is inherently multi-scale, in that microscopic events at the subcellular level generate emergent properties at the macroscopic tissue level. In fact, many phenomena at the whole heart level can be correlated with similar behaviors in myocytes.
Generally, engineers use the active tension generated by the myocytes to compute the deformation of the organ. The models of active tension development in cardiac muscle proposed over the years may be grouped into three categories [51]:

1. Time-varying elastance models: they include the essential dependence of cardiac active force development on muscle length and time;
2. Hill-type models: the active force of the contractile element comes from the force generated by the actin and the myosin cross-bridges at the sarcomere level;
3. Fully history-dependent models: based either on system of partial differential equations as functions of time and cross-bridge position, or on myofilament activation models as functions of time and shortening velocity.

In this project, the generation of active stress in the fiber direction is a Hill-type model. In particular, the three-wall segment (TriSeg) model described by Arts et al. [52] and later used by Lumens et al. [53] is used to describe the mechanics and hemodynamics of ventricular interaction. In this model the sarcomere is described as a passive element in parallel with a series combination of a contractile element and series elastic element. This empirical representation of sarcomere contraction simulates experiments on isolated rat cardiac muscle. The length of the contractile element (L_{sc}) and a time-variant contractility parameter (C) are state variable.
In the model the natural myofibres strain is converted to sarcomere length by:

$$L_s = L_{s,ref} e^{\varepsilon_f} \tag{8}$$

and then the normalized length of the series elastic element is calculated:

$$L_{sNorm} = (L_s - L_{sc})/L_{SerEl} \tag{9}$$

Where:

L_s: Sarcomere length;

$L_{s,ref}$: Reference sarcomere length at zero strain;

ε_f: Myofibres strain;

L_{sNorm}: Normalized length of the series elastic element;

L_{sc}: Length of the contractile element (state variable);

L_{SerEl}: Length of the series elastic element during isometric contraction.

The contractile element velocity (dL_{sc}/dt) and the contractility (C) are calculated by:

$$\frac{dL_{sc}}{dt} = \begin{cases} \frac{L_{sNorm}-1}{b_{Hill}\,L_{sNorm}+1} * v_{max} & L_{sNorm} \leq 1 \\ \frac{L_{sNorm}-1}{b_{Hill}\,L_{sNorm}+1} * v_{max} * e^{a_{Hill}(L_{sNorm}-1)} & L_{sNorm} > 1 \end{cases} \quad (10)$$

$$\frac{dC}{dt} = \frac{1}{\tau_r} * C_L * f_{rise} + \frac{1}{\tau_d} * \frac{C_{rest}-C}{1+e^{(T-t)/\tau_d}} \quad (11)$$

Where t is time elapsed since electrical activation, C_L regulates contractility dependence on contractile element length, f_{rise} regulates rise of contractility, and T regulates twitch duration as function of contractile element length. The full set of equations underlying the model is reported in Appendix B.

The active myofibres stress, $\sigma_{f,act}$, is computed as dependent on length of series elastic elements, and mechanical activation. In the Equation (12), σ_{act} represents the active myofibres stress scaling factor.

$$\sigma_{f,act} = \sigma_{act} * C * L_{sNorm} \quad (12)$$

The value of $\sigma_{f,act}$ is added to the passive stress ($\sigma_{f,pass}$) to get the total Cauchy myofibres stress σ_f:

$$\sigma_f = \sigma_{f,pass} + \sigma_{f,act} \quad (13)$$

3.2.4 Circulation model and boundary conditions

The ventricle is an open system, in that it ejects blood into the circulation bed and receives blood from it. Hence, the pressure-volume behavior of the ventricle, and the associated wall strains and stresses, depend on the hydraulic properties of the circulatory system. In order to model ventricular mechanics throughout a complete cardiac cycle, including systolic ejection and diastolic filling, without imposing both the time-dependent pressure within the ventricular chamber and the time-dependent geometry of the LV wall, it is hence mandatory to couple the 3D ventricle model with a lumped-parameter model of the circulation a circulatory model is needed to ensure realistic diastolic filling and ventricular–vascular coupling.

Several models have been designed to simulate the closed-loop circulation on a beat-to-beat basis. One is the three-element Windkessel model [54] (Figure 3.5 A). This model relates pressure to flow using two parameters: arterial compliance, representing the extensibility of the major arteries, peripheral resistance, the resistance to flow encountered by the blood as it flows from the major arteries to the capillaries, and characteristic impedance of the aorta, for the local inertia and local compliance of the proximal aorta. Although yielding realistic waveforms, estimates of compliance and impedance values, after fitting, are different from values obtained from (Figure 3.5 C). A fourth parameter in the four-element Windkessel model (Figure 3.5 B), the inertia of the whole arterial system, resolves this problem [55].

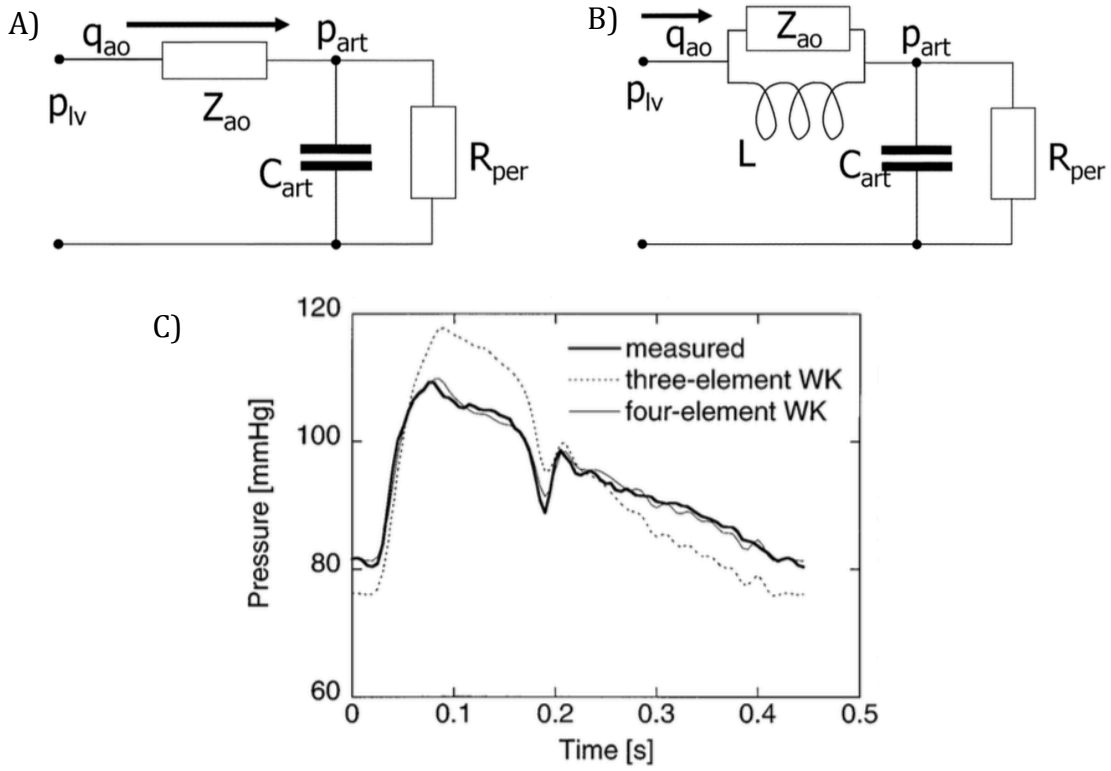

Figure 3. 5 – Electrical circuit analogues of three-, and four-element Windkessel model (**A** and **B** respectively). Cart: arterial compliance; L: arterial inertance; Part: arterial pressure; Plv: left ventricular pressure; qao: aortic flow; Rper: peripheral resistance; Zao: aortic impedance. **C)** Comparison of measured aortic pressure and aortic pressure predicted by 3- and 4-element Windkessel models on basis of compliance and characteristic impedance derived from standard methods [55].

The circulation can be represented in more detail by identifying individual components and assembling them in a more complex lumped circulatory model [52, 56-58]. As already said, the problem with these models is the high number of parameters, some of which need to be estimated or collected from different species. For example, in the CircAdapt model (Figure 3.6) the whole circulation is composed of four module types: compliant blood vessels, actively contracting chambers, valves with inertia, and peripheral resistance.

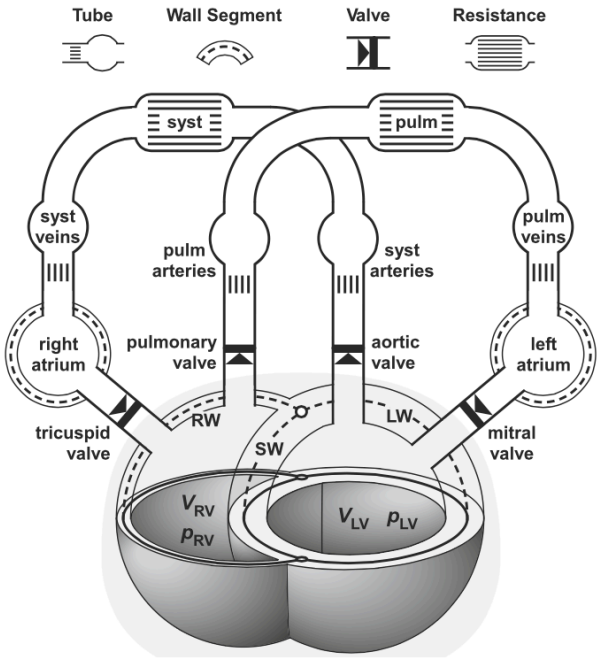

Figure 3. 6 – CircAdapt model of the systemic (syst) and pulmonary (pulm) circulations.

3.3 Cardiac electromechanical models

Computational models of cardiac electro-mechanics (EM) are increasingly being considered in clinical applications as an additional modality to optimize therapies or understand therapy mechanisms.

Historically, the development of electro-physiological and mechanical models of cardiac function proceeded rather independently than in tandem (Figure 3.7). The vast majority of EP modeling studies ignored any effects due to mechanical deformation, and vice versa, most mechanical modeling studies did not represent explicitly any feedback of deformation on EP [5].

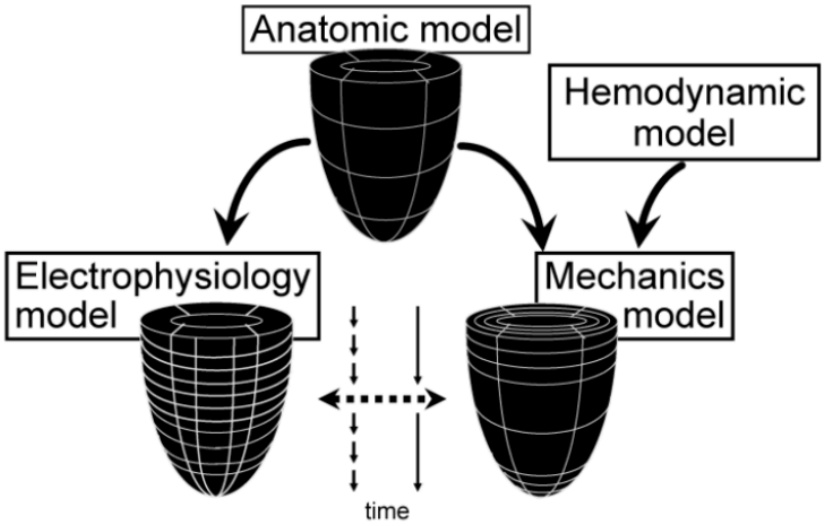

Figure 3. 7 – The four most important components for models of cardiac electro-mechanics: anatomy, electrophysiology, mechanics, and hemodynamics. Mechanics and electrophysiology models are considered independent.

However, the electrophysiological function of the heart does not exist separately from its mechanical function. The incorporation of mechanical function into such simulations is of fundamental interest. The most common approach in designing models of cardiac electro-mechanics is coupling existing models of cellular electrophysiology and active mechanics.
Whole-heart models of cardiac electro-mechanics have been used to study the influence of local disturbances in electrical propagation or cellular electrophysiological pathologies on regional contraction and global heart function [7, 35, 59-63].
In this work the attention is on single ventricle mechanical models.
To date, numerous computational mechanics models exist to simulate the behavior of the left ventricle [33, 64-66]. They have been mostly used to understand the distribution of myofibres stress and strain under a variety of circumstances.
An example of single ventricle model is the work of Vetter et al. [33]. They used a finite element model to determine regional stress and strain distributions in rabbit left ventricular myocardium during passive filling.
Also, Choi et al. [66] tested the hypothesis that LV shape and wall thickness influence regional mechanics directly. Using a finite element model, fiber stress and strain distributions at the end of the passive filling phase were compared for different LV shapes and wall thickness.

Chapter 4

Materials and methods

4.1 Project workflow

This chapter explains the necessary steps for the 3D reconstruction of the right ventricle anatomy for two patients with Hypoplastic Left Heart Syndrome (HLHS) and previously surgically treated with the Fontan procedure.

Patient-specific cardiovascular model consists of four main components, as described in Chapter 3;

an anatomic model of the ventricle, a passive constitutive model, an active contractile model, and an hemodynamic model (Figure 4.1).

The anatomic model of the ventricles consists in the unloaded ventricular geometry and in a fiber-sheet local material coordinate system, that represent the myofibers and sheet architecture.

The second component of the patient-specific model consists in the constitutive law for the resting myocardial material properties. The third component is the active-contractile law that simulates muscle contraction. The last component is the lumped-parameter closed-loop hemodynamic model that generates the boundary condition for the ventricular finite-element model.

For this project, the realization of patient-specific anatomic models was initially provided by a semi-automatic segmentation of short axis MRI images, using the software *Seg3D*. Subsequently, a manual fitting in *Blender* was used to adjust a mono-ventricular mesh template to the patient-specific segmentation data.

The software *Continuity* was used to enrich the model with fibers and to run biomechanics simulations. First, unloaded ventricular geometry was estimated using two different approaches. The passive material model was described by the Ogden-Holzapfel formula [46]. Art's model [52] was used to describe the active contraction model. Passive and active models were introduced in the finite element model. Here, the parameters were adjusted to match the patient's end-diastolic pressure–volume relation, and the left and right-ventricular cavity pressures measured in the patient, respectively.

In order to study the accuracy and reliability of the models, the stroke work density and the total right ventricle work were computed and compared with values from literature.

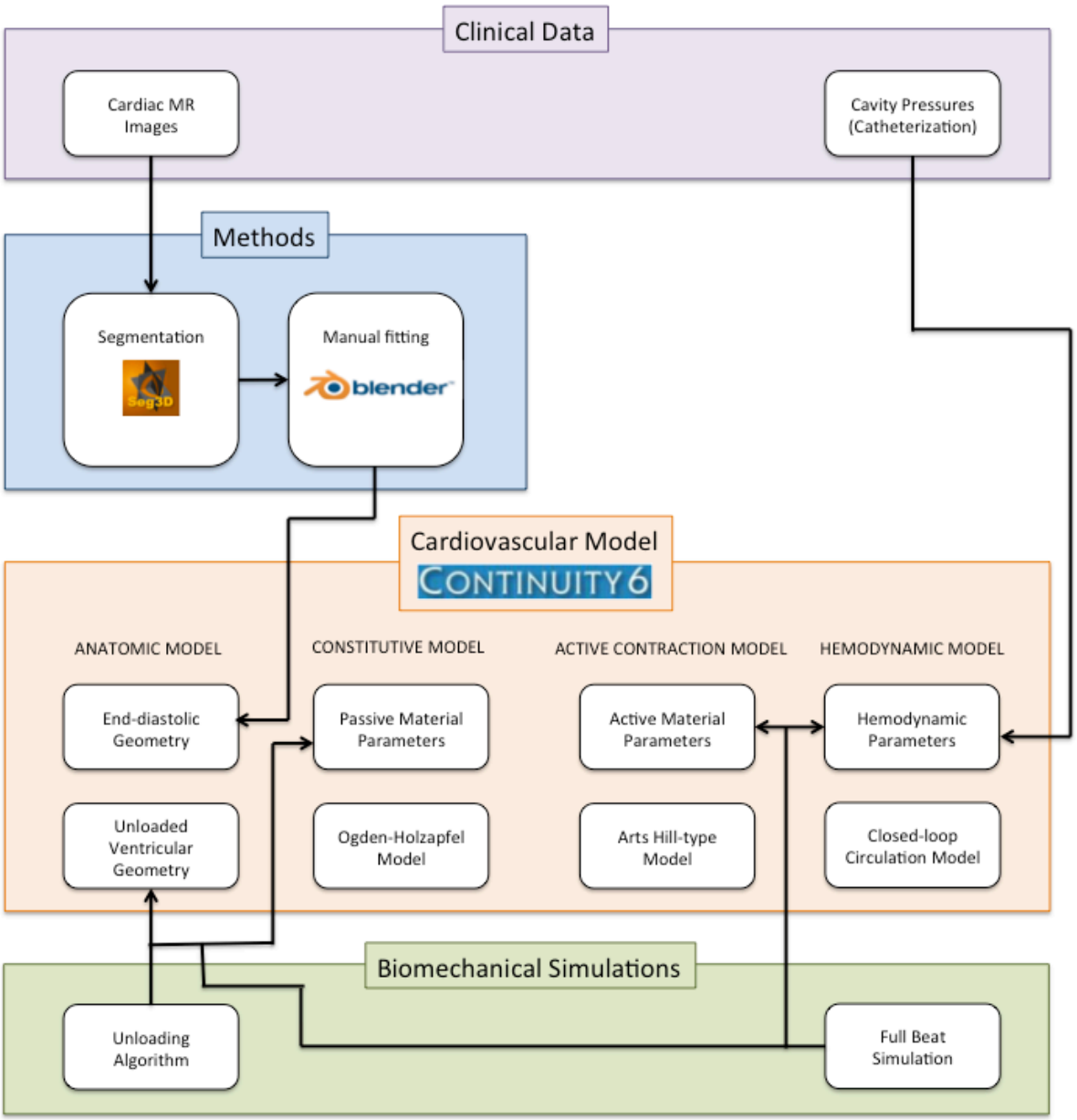

Figure 4. 1 – Project workflow. From the Clinical data to the Cardiovascular model.

4.2 Acquisition and analysis of the clinical data

Clinical data acquisition is an important step of the whole modeling process. Single ventricle (SV) patients represent a particularly challenging population to study, du to their young age range and the unstable nature of their physiology, thereby limiting the number of potential participants.

Clinical data of two infants affected by HLHS were collected from the Rady Children's Hospital San Diego (Table 4.1). Heart MRI with and without contrast, and Cardiac Catheterization were performed after Stage 3 of the Fontan procedure.

Associated to SV defects, the following pathologies affected these two patients:

1. RCHSD-00005-01: Severe hypoplasia of the left ventricle and mitral atresia.
2. RCHSD-00006-01: Mitral atresia and severe aortic stenosis, severe hypoplasia of the left ventricle with very small ventricular septal defect.

	RCHSD-00005-01	**RCHSD-00006-01**
Date of Birth	2010	09/09/2011
Date of Acquisition	2012	03/14/2012
Gender/Age	Female/2Y	Female/6M
HR (bpm)	95	94
LV End-diastolic Volume (cc)	4	3.4
LV EDV indexed to BSA (cc/m2)	8	10
LV End-systolic Volume (cc)	2	1
LV Stroke Volume (cc/beat)	2	2.4
LV Cardiac Output (cc/min)	170	200
LV Ejection Fraction (%)	48	70
RV End-diastolic Volume (cc)	47	39
RV EDV indexed to BSA (cc/m2)	110	144
RV End-systolic Volume (cc)	23	21
RV Stroke Volume (cc/beat)	24	18
RV Cardiac Output (L/min)	2.8	2.5
RV Ejection Fraction (%)	51	54
RV End-diastolic pressure (mmHg)	7	8
RV Systolic peak pressure (mmHg)	100	80

Table 4. 1 – Personal data and ventricular function/ dimensions for the analyzed patients.

The client side software of the *Cardiac Atlas Project (CAP Client*) was used to visualize the cardiac MRI. DICOM images can be opened from the main window and the different views labeled to allow for their analysis (Figure 4.2).

Digital Imaging and Communications in Medicine (DICOM) is a standard for handling, storing, printing, and transmitting information in medical imaging. It includes a file format definition and a network communications protocol.

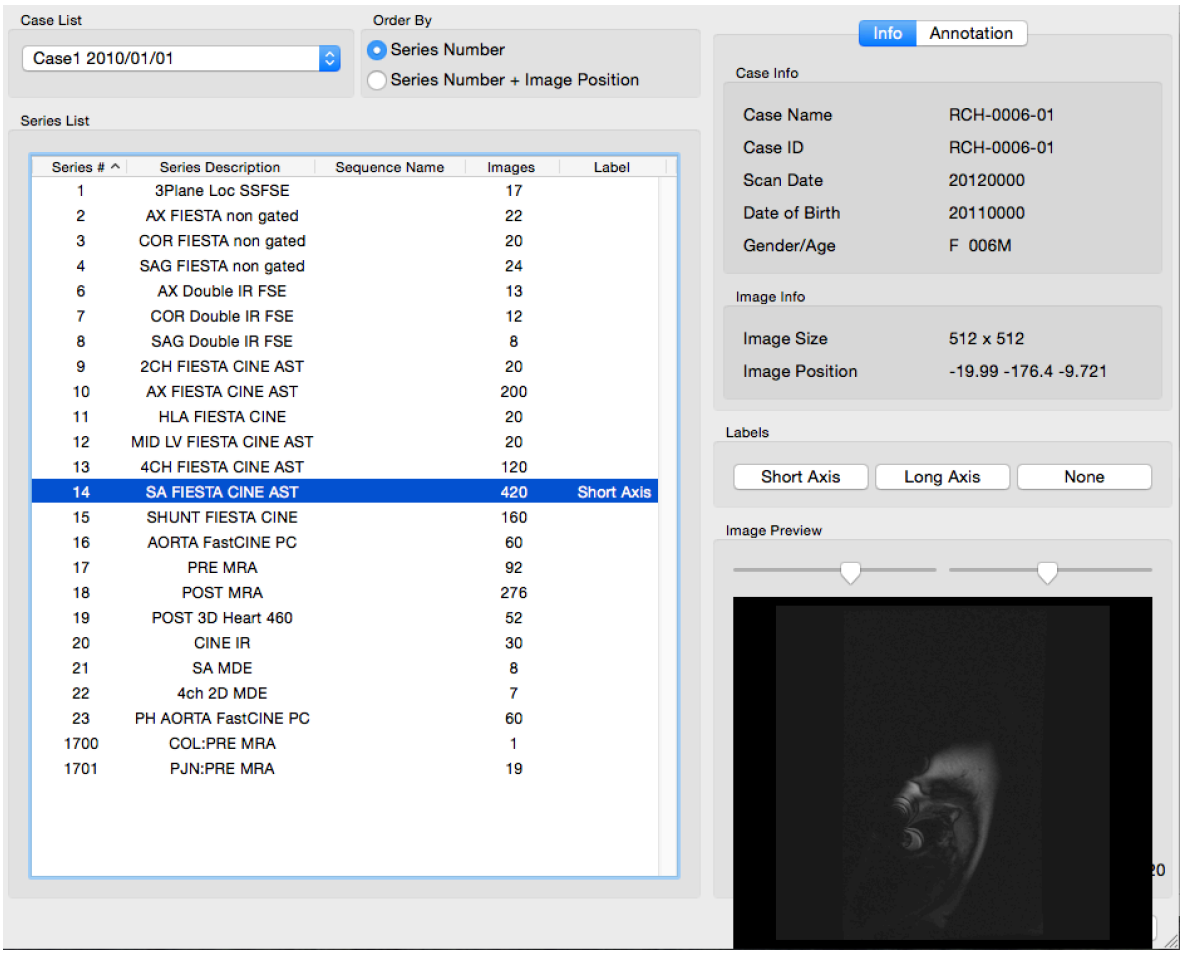

Figure 4. 2 – Main window of the CAP Client tool. It consists of different panels: on the left the Series List with all the possible views, on the right the Case info, the Labels, and the Image Preview.

The platform allows the user to control the brightness, the contrast, and the animation speed. At the bottom of the window, an arrow can be moved to visualize each moment of the cardiac cycle for every slice (Figure 4.3).

For the project, only short axis images were selected. Eleven slices on the short axis plane were acquired, in 30 different points of the cardiac cycle, for a total of 330 images.

The short-axis imaging plane has several advantages: most of the left or right ventricle, except the most basal and apical portion, can be very easily studied. The major limitation is the difficulty in assessing the valve plane, and the interface between ventricle and atrium. Inclusion or exclusion of the basal slice can lead to changes in volume of 13-15% [67].

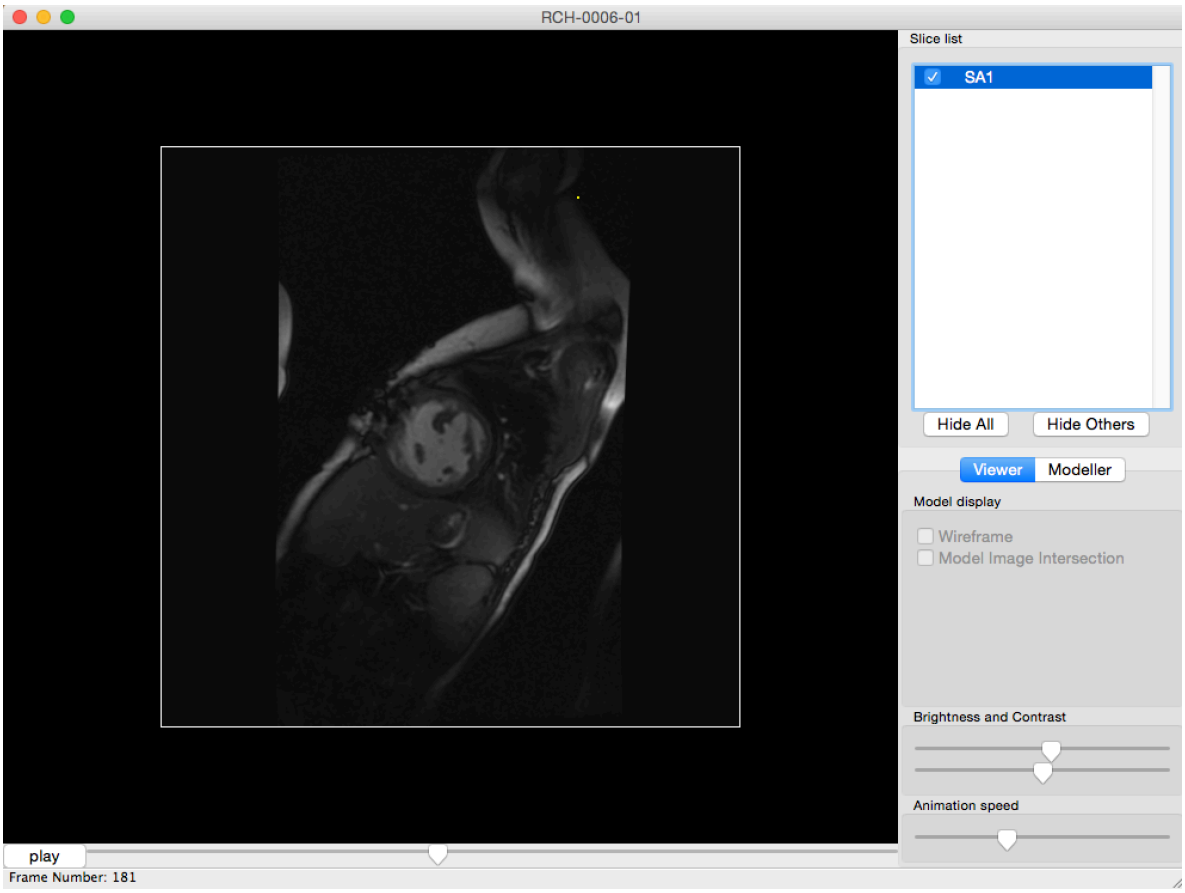

Figure 4. 3 – Short axis view of the cardiac MRI for a patient affected by HLHS. On the right the slice list with the views previously selected and in the main black window the image. At the bottom the user can run the animation with the '*Play*' button or move the arrow on the interested frame.

4.3 Segmentation process

4.3.1 The software: *Seg3D 2.1*

Seg3D is a lightweight software tool developed for visualizing and segmenting image data. The main intended use of Seg3D involves loading 3D scalar data, such as MRI or CT scans, and generating labels mask to identify various regions of interest in the original image data.

The default layout when Seg3D is opened and a new project is created is shown in Figure 4.4. The interface for Seg3D consists of a number of viewers (both 2D and 3D), windows to control the functionality of Seg3D, and a tool bar at the bottom of the screen.

Figure 4. 4 – Seg3D interface.

- **Viewer panels:** There are four type views options, 2D or 3D. The 2D slice viewer can be used to control the visualization and manipulation of image and segmentation data (axial, sagittal and coronal). The 3D volume viewer allows the user to see the 3D representation of the original and segmented data (volume).
- **Tools window:** This window houses the current tools that the user has selected from the '*Tools*' drop down menu.

- **Layer manager window:** This window contains all of the mask and volume files involved with the session. The masks colors correspond to the label masks seen in the viewer windows.

4.3.2 Segmentation of cardiac MRI

Seg3D is used to segment the cardiac MRIs at end-diastole of the two patients described above.

Images are segmented in NIfTi format. The Neuroimaging Informatics Technology Initiative (NIfTI) has the purpose to support service, training, and research to develop and enhance the utility of informatics tools used in neuroimaging, with a focus on functional magnetic resonance imaging.

It is first necessary to convert all the images from DICOM to NIfTi format. To do that, the DCM2NII software was used.

All the images were converted, but only the eleven slices at the end of diastole (ED) were imported in Seg3D. This choice was based on the biomechanics simulations. In fact, the ED geometry is the one most commonly used in literature [8, 9, 68] to get the unloaded reference state.

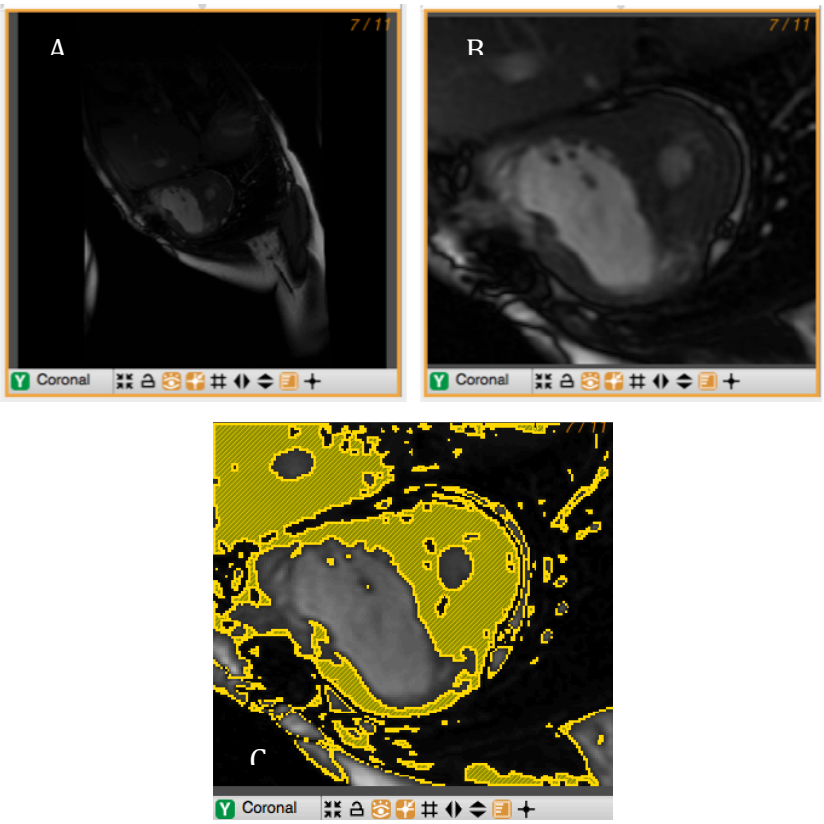

Figure 4. 5 – A) Coronal view in Seg3D**. B)** Same view after using the 'crop' tool. **C)** 'Threshold' tool is used to create a mask label.

MRIs were segmented in four different views: volume, axial, sagittal, and coronal. The main view used for short axis images was the Coronal one because it allows for clearly seeing the two ventricular chambers (Figure 4.5 A). At the end the volume view was used to manage the 3D segmentation.

First, the images were cropped to focus the view on the two heart chambers (Figure 4.5 B). Subsequently, a mask label was generated. The maximum and minimum threshold values were adjusted through the tool options to get a rough segmentation of the region of interest (Figure 4.5 C). Excess regions in the mask were removed manually (Figure 4.6 D). The same procedure was repeated for all of the slices.

The final result was visualized in the Volume frame to get an overall view of the 3D segmentation (Figure 4.6 A).

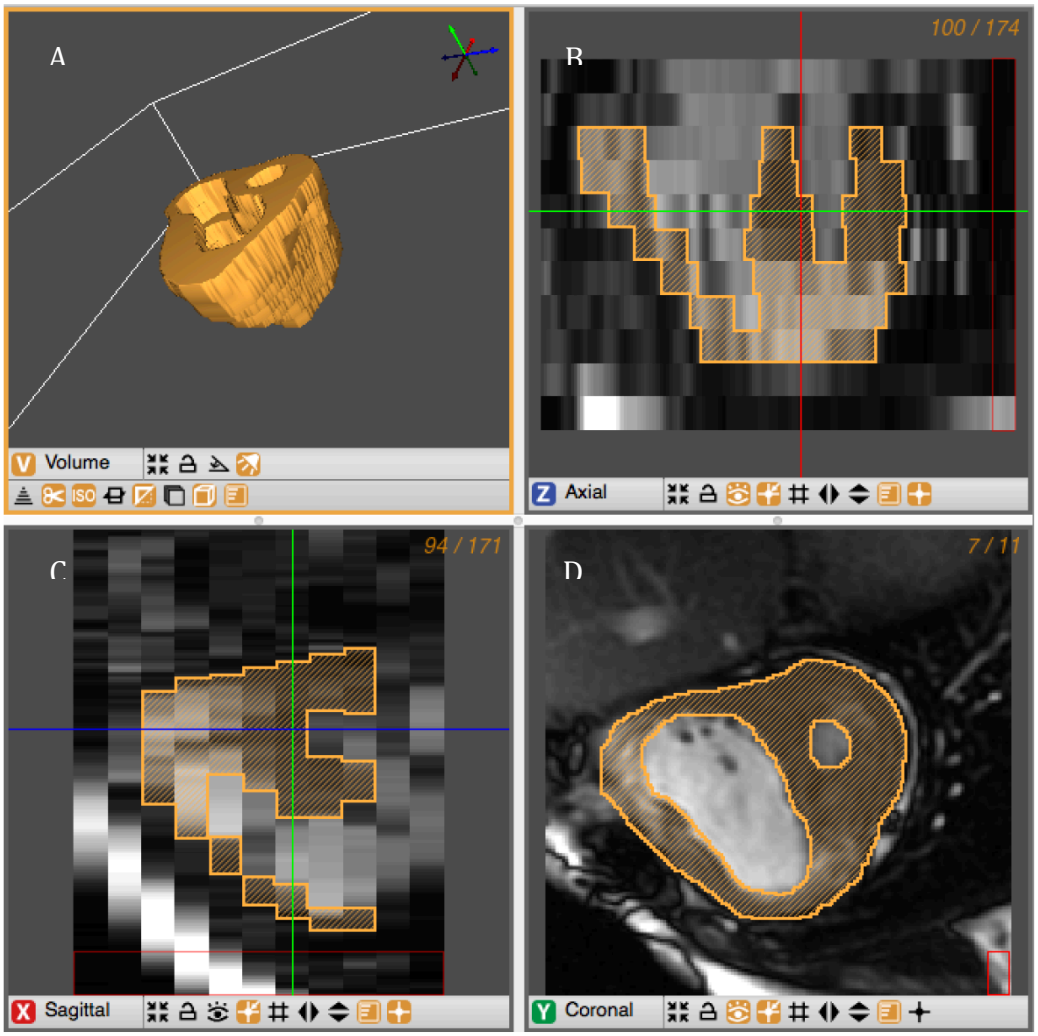

Figure 4. 6 – Viewer window at the end of segmentation. **A)** Volume view. **B & C)** Axial and Sagittal views show the two ventricular cavity. **D)** Coronal view after the use of '*Paint Brush'*.

4.4 Mesh fitting

4.4.1 The software: *Blender 2.49*

Blender is a professional free and open-source 3D computer graphics software product used for creating animated films, visual effects, art, 3D printed models, interactive 3D applications and video games.

Blender's features include 3D modeling, texturing, raster graphics editing, rigging and skinning, fluid and smoke simulation, particle simulation, soft body simulation, sculpting, animating, match moving, camera tracking, rendering, video editing and compositing.

The software provides cross-platform interoperability, extensibility, and incredibly small footprint, and a tightly integrated workflow.

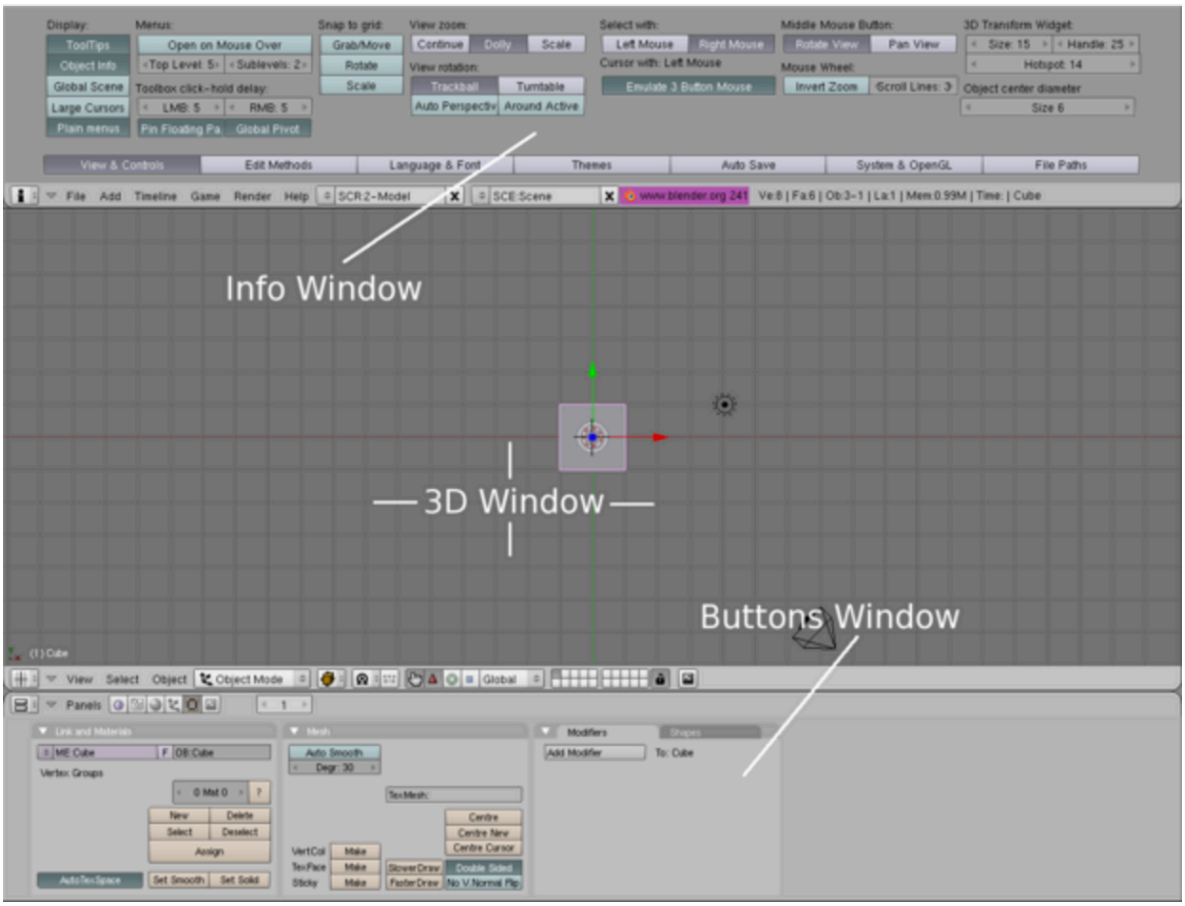

Figure 4. 7 – Blender's default screen layout with the main windows: Users interface (Info), 3D and buttons window.

Three window types are provided in Blender's default screen (Figure 4.7):

- 3D view: It provides a graphical view into the scene you are working on. You can view your scene from any angle with a variety of options.
- Buttons window: It contains most tools for editing objects, surfaces, textures, lights, and much more.
- User preferences: It contains global configuration settings.

In Blender there are two primary modes of work: *Object Mode* and *Edit Mode* (Figure 4.8).

Object mode is used to manipulate individual objects as a unit (move, scale, and rotate entire polygon mesh), while Edit mode is used to manipulate the actual object data (for example individual vertices of a single mesh).

Once the mode is selected, the user can start working using the buttons window.

Each button on the Buttons header group panels is group together into what is called a context (Figure 4.8). There are six main contexts: Logic, Script, Shading, Object, Editing, and Scene. Each of these might be subdivided into a variable number of sub-contexts, determined on the basis of the active object.

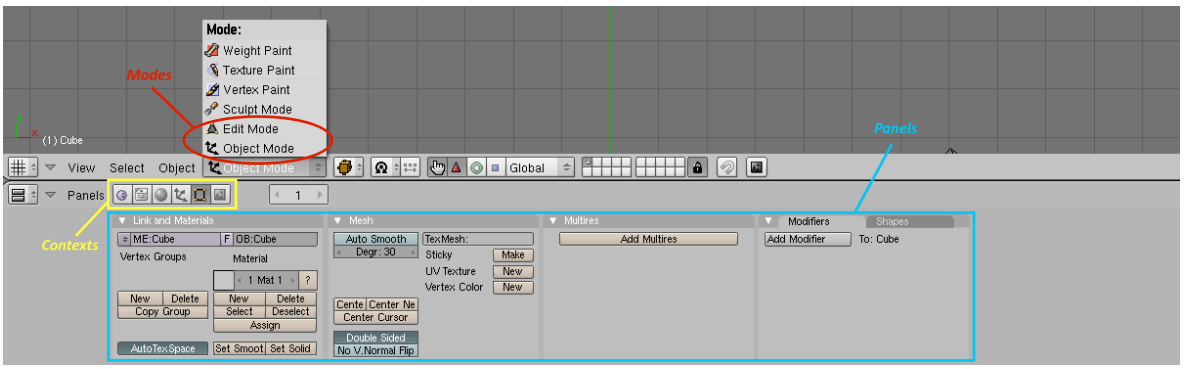

Figure 4. 8 – Blender's main features: Modes (red), Contexts (yellow), and Panels (blue).

4.4.2 Fitting the mesh with the patient-specific data

Blender is used to fit the mesh template with the patient-specific data. The model was then used for biomechanics simulations.

To start, segmentation outputs were imported in Blender. Here patient-specific data were separated into three different materials represented with colors (Figure 4.9 A): epicardium (red), right ventricle (green), and left ventricle (blue). This process is useful to fit correctly the mesh template with the patient data. In fact, it helps the placement of the mesh vertices on the correct surface.

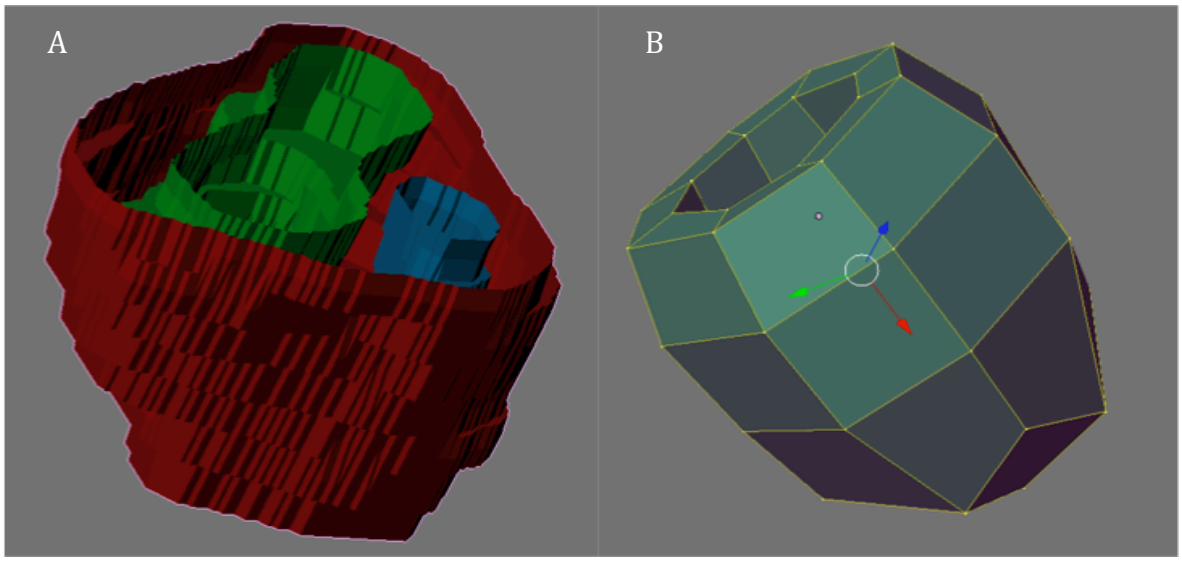

Figure 4. 9 – A) Patient-specific data separated into three different material: myocardium (red), right ventricle (green) and left ventricle (blue). **B)** Mono-ventricular mesh template.

Then, a mono-ventricular mesh template was used to model the right ventricle (Figure 4.9 B). It was previously carried out by the Cardiac Mechanics Research Group (CMRG) at UCSD, and made up of 28 elements and 66 nodes.

The template was uploaded in Blender and scaled, then rotated and translated to align it with the patient-specific data. The inner surface of the template was fitted with the right ventricle endocardium (green), while the outer surface with the epicardium (red).

During the process, it is important to keep the element close to being cubic in order to avoid distortion errors during biomechanics simulations. Figure 4.10 shows the final fitting result.

The critical aspect of the process was the use of a mono-ventricular mesh template to fit a bi-ventricular segmentation. This led to an inaccurate fitting in the septal side of the right ventricle.

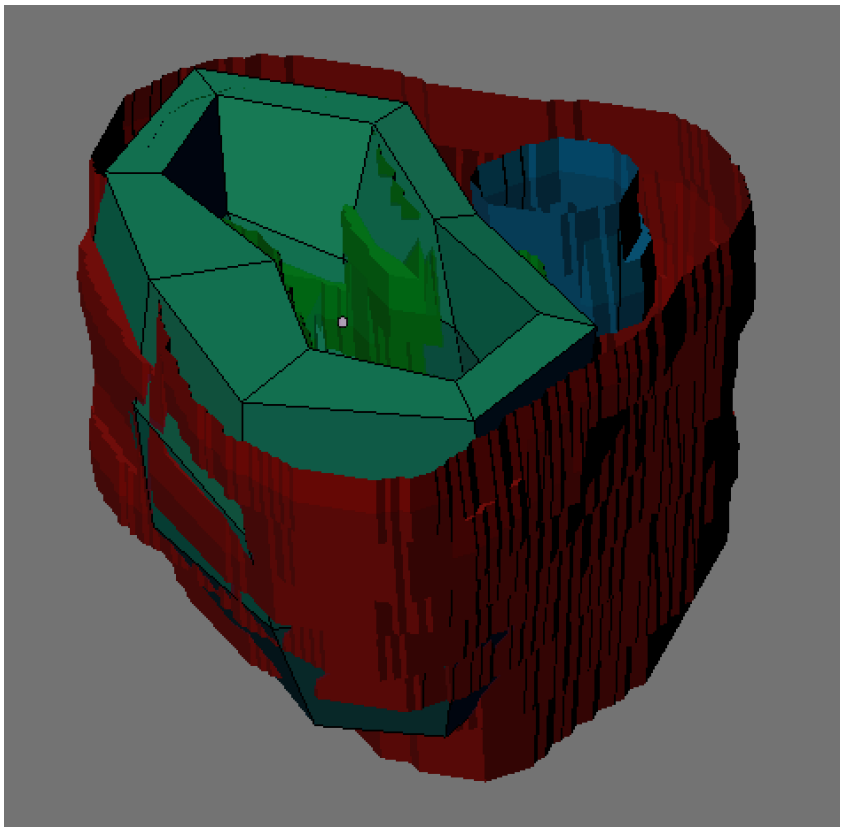

Figure 4. 10 – The mesh template fits the patient-specific data.

The '*Hex Blender'* tool (Figure 4.11 A) has been used to convert elements and nodes information into text file, which is a format that Continuity can recognize. Then, the *'Tricubic Hermite'* tool was used to refine the mesh. This tool increases the number of elements in the mesh and makes it smoother by computing the derivatives at each node. The refined mesh was composed of 1792 elements and 2325 nodes (Figure 4.11 B).

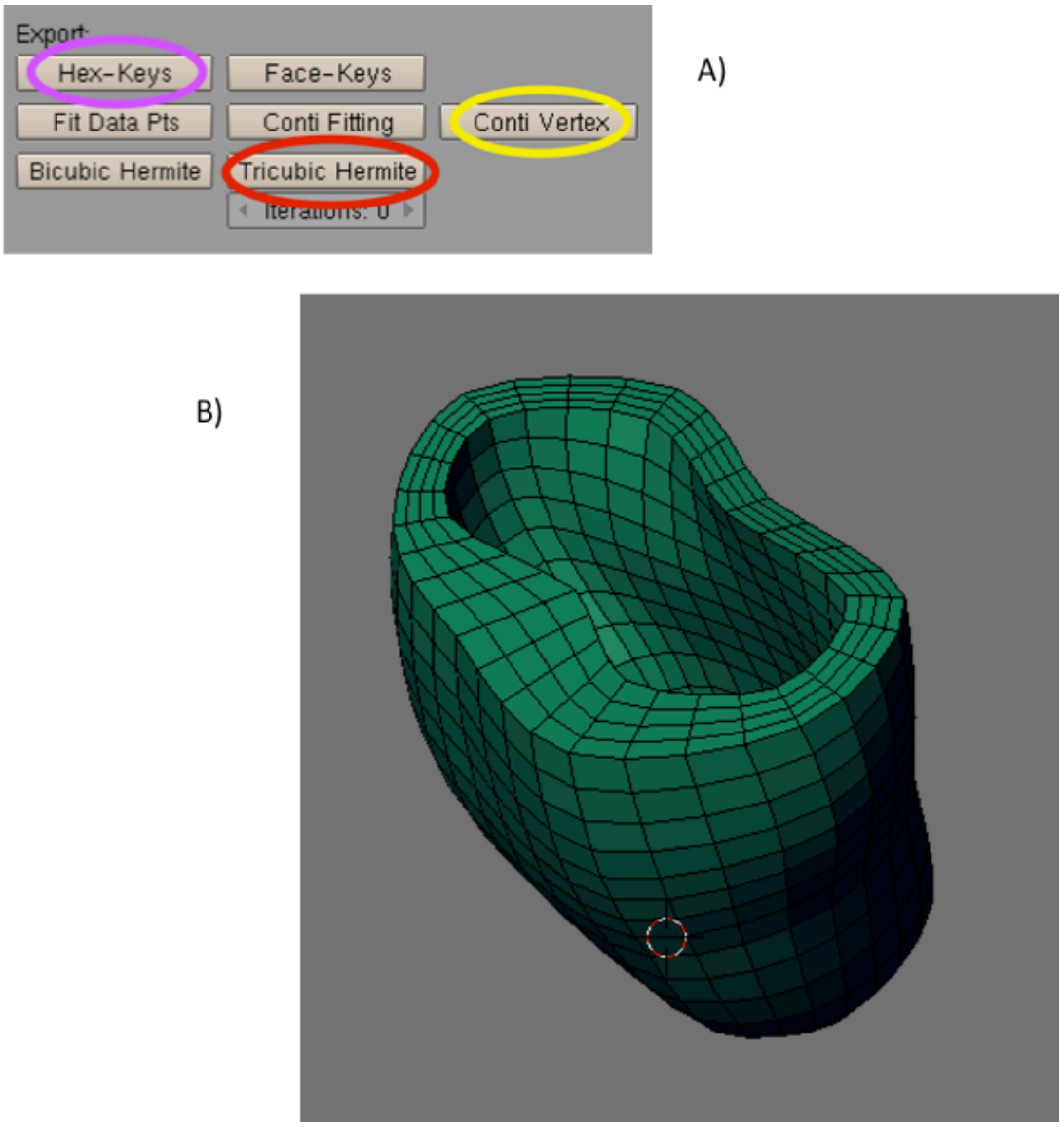

Figure 4. 11 – A) Hex Blender tool used to convert elements (Hex-Keys) and nodes (Conti-Vertex) in text file. **B)** Refined mesh after the use of Tricubic Hermite tool.

4.5 Patient-specific mono-ventricular model

4.5.1 The software: *Continuity 6*

Continuity 6 is a problem-solving environment for finite element analysis in bioengineering and physiology. It is freely available for academic use under the license provided by UCSD. The software has been developed by CMRG (Cardiac Mechanic Research Group) in order to support its own research on cardiac physiology and pathophysiology. For this reason the software represents the best choice in this study, since it perfectly suits the multi-scale problems in cardiac electrophysiology and biomechanics including coupled, multi-physics, multi-scale models of the heart.

Continuity 6 includes tools for least-squares fitting of geometric meshes and parametric models to experimental data including medical, morphological and histological images, physiological and biomechanical measurements.

Continuity 6 is portable and object-oriented; making use of the very high-level open-source language Python for scripting and component integration. It is designed to facilitate interoperability with desktop tools such as Microsoft Excel and MATLAB.

The server has dynamically fillable and loadable numerical analysis functions for mesh handling, data fitting and image handling, biomechanics, electrophysiology, and transport processes (Figure 4.12).

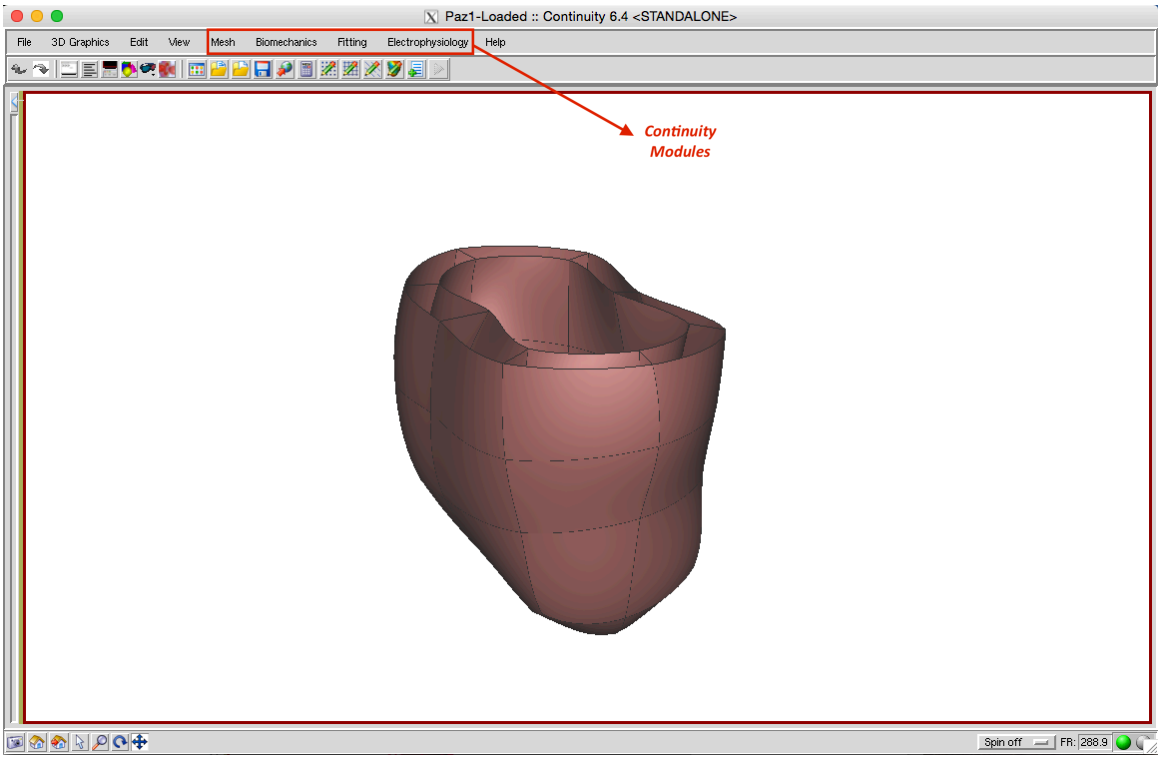

Figure 4. 12 – Continuity standard workspace. Modules bar is located in the upper part of the screen (red). At the bottom, manipulator tools allow the zoom, the translation, and the rotation of the object.

4.5.2 Anatomic model

Before importing nodes, elements, and scale factors from Blender, Continuity has to be set. As first step, Coordinates and Basis function module have been compiled. For the project, Global Rectangular Cartesian coordinates and 3D cubic Hermite basis function were selected (Appendix A).

At this point nodes, elements, and scale factor files were imported in Continuity. It is important to change the basis to cubic-cubic-cubic per each coordinate, and radians for the angles in the Nodes Form.

The path **Send → Calculate Mesh → Render Nodes/Elements** (Figure 4.13) was used to render elements lines and surfaces.

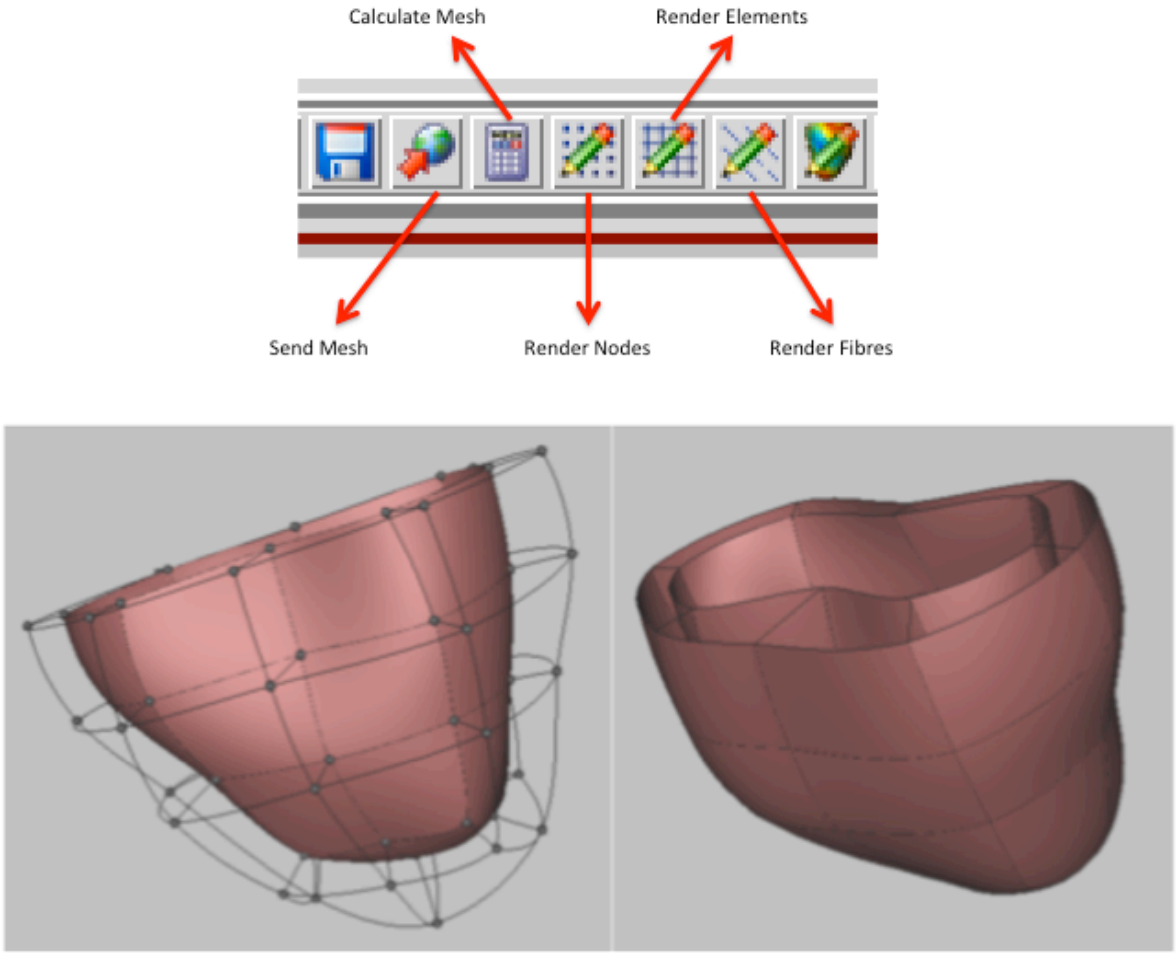

Figure 4. 13 – Top: tools used to render the mesh. **Bottom:** on the left nodes and lines of the mesh; on the right rendered surfaces of the endocardium and the epicaridium.

The active element was included in the model; adding fiber to both the epicardium and the endocardium surface.

Following the morphology and the passive behavior of the myocardium described by Holzapfel and Ogden [46], two different angles were set in the model: -60° for the endocardium, about 0° in the myocardium and finally + 60° to the endocardium (Figure 4.14). Fiber angles were manually added per each node.

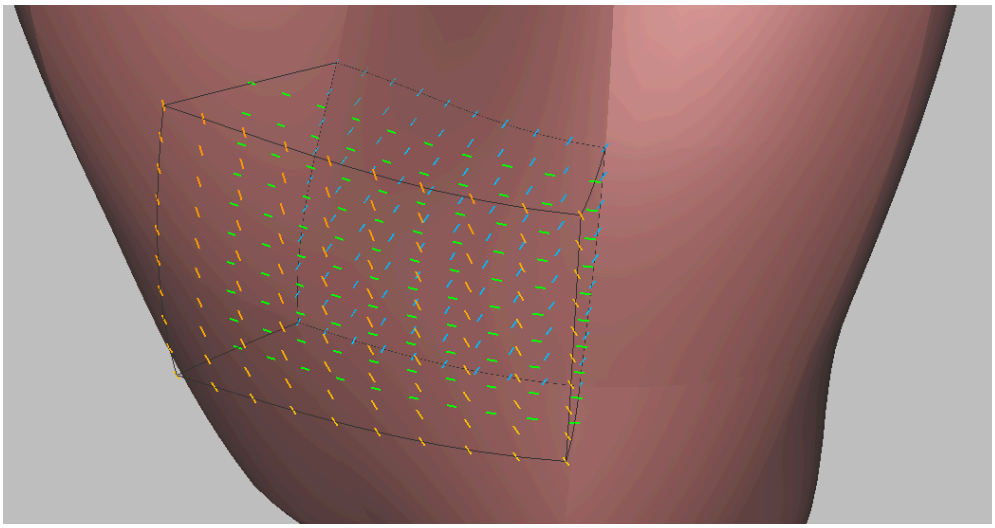

Figure 4. 14 – In the figure it is highlighted a single element of the model to show the fiber angle of endocardium (blue), myocardium (green), and epicardium (orange).

KINEMATIC BOUNDARY CONDITIONS

In order to prevent undesired rigid body motions (i.e. displacement or rotation), boundary conditions were imposed to the 3D models.

Nodes constraints were placed at the epicardial base in order to simulate atrial physiological bonds. Displacements in the base-to-apex-direction (X axis) of the nodes at the ventricular base were suppressed. In addition, two nodes in the anterior and posterior sides of the right ventricle were constrained from shifting along the *Z* axis. Similarly, other two nodes in the septum and freewall sides were constrained from shifting along the *Y* axis (Figure 4.15). Furthermore, rotations of the nodes at the ventricular base were suppressed.

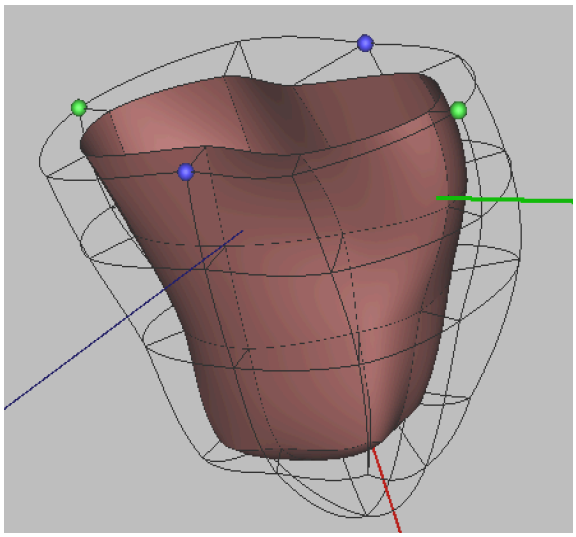

Figure 4. 15 – Nodes constraint at the epicardium base. Displacements along the X axis and rotations of all the nodes at the ventricular base were suppressed. In addition, two nodes on the Y axis (green) are constraint in Z direction. At the same way, two nodes of the Z axis (blue) are constraint in Y direction.

4.5.3 Constitutive model

In this study, the myocardium was considered as a slightly compressible material with an assumed decoupled isochoric and volumetric material behavior. The strain energy function results as:

$$\psi = \psi_{iso} + \psi_{vol} \tag{1}$$

For what concerns the isochoric component, the transversely-isotropic form of the Holzapfel and Ogden model was used [46] (Chapter 3, Section 3.2.2).

$$\psi_{iso} = \frac{a}{2b} e^{b(I1-3)} + \frac{a_f}{2b_f}(e^{b_f(I4_f-3)^2} - 1) \tag{2}$$

Where a, b, a_f, b_f are four positive passive material constants. The a parameters having dimension of stress, whereas the b parameters are dimensionless.

Systolic intra- and extra-vascular fluid displacements were taken into account by adding the volumetric part of the strain energy function.

$$\psi_{vol} = K(J-1) * \ln(J)/2 \tag{3}$$

Here, *K* represents the bulk-modulus. It measures the resistance to uniform compression.

4.5.4 Active contraction model

Active material properties are necessary to simulate an entire cardiac cycle.

The dynamic model described by Arts [52] (Chapter 3, Section 3.2.3) was used to describe active myocardial contraction. Here, the sarcomere is modeled as a passive element in parallel with a series combination of a contractile element and series elastic element.

The governing differential equations for sarcomere length and contractility are calculated by:

$$\frac{dL_{sc}}{dt} = \begin{cases} \frac{L_{sNorm}-1}{b_{Hill}\,L_{sNorm}+1} * v_{max} & L_{sNorm} \leq 1 \\ \frac{L_{sNorm}-1}{b_{Hill}\,L_{sNorm}+1} * v_{max} * e^{a_{Hill}(L_{sNorm}-1)} & L_{sNorm} > 1 \end{cases} \tag{4}$$

$$\frac{dC}{dt} = \frac{1}{\tau_r} * C_L * f_{rise} + \frac{1}{\tau_d} * \frac{C_{rest}-C}{1+e^{(T-t)/\tau_d}} \tag{5}$$

Specific parameters and equations are collected in Appendix B.

The active myofibres stress is then calculated as dependent on length of series elastic element, contractile element length, and mechanical activation.

This value is summed to the passive stress to get the total Cauchy myofibres stress.

4.6 Biomechanics simulations

4.6.1 Unloaded geometry simulation

As already said in Chapter 3, the *in-vivo* cardiac images usually refer to the end diastolic point of the cardiac cycle where the pressure is not zero. This requires the determination of the unloaded reference geometry. Two different approaches were tested to estimate the unloaded reference geometry.

The first one consisted in the Krishnamurthy's algorithm [8]. It was implemented in an iterative python script from the CMRG and it was modified to fit a mono-ventricular model.

The developed method can estimate the unloaded state given the end-diastolic geometry, pressure, and passive material properties.

Passive material properties were unknown for HLHS patients considered in the project. Optimized patient-specific parameters from Krishnamurty et al. [8] have been used to run the simulation (Table 4.2).

Passive Material Parameters	Default values
a (kPa)	0.3192
af (kPa)	0.236
b	9.726
bf	15.779
K (kPa)	350

Table 4. 2 – Passive material parameters used for the unloaded geometry simulation [8].

The algorithm (Figure 4.16) consists of two iterative steps. First, a linear increment in pressure is applied to reach the measured end-diastolic pressure (Inflation step). Second, the inverse of the deformation gradient, calculated during the inflation phase to the initial mesh, is applied thus creating a new unloaded state (Deflation step).

Time step and pressure increments per time step were set depending on patient-specific end-diastolic pressure.

Time step = 1 msec

$$PstepRV = \begin{cases} \frac{EDPrv}{4000} & 0 < RVP < \frac{EDPrv}{25} \\ \frac{EDPrv}{200} & \frac{EDPrv}{25} < RVP < EDPrv \end{cases} \quad (6)$$

Where RVP was the current right ventricular pressure.

The increment step was set on a smaller value at the beginning to facilitate the passive filling.

During all the Inflation or Deflation steps, the nodes form in the Continuity file, which is updated with the new values. Only nodes coordinates are updated, while nodes derivatives are not modified. This is a limit which was not yet been solved by the Cardiac Mechanics Research Group and led to problems during the simulation.

To overcome the drawback, the entire procedure was carried out with 3D Linear Lagrange basis functions. These only consist of nodes coordinates without derivatives. The model appeared less smooth than the one with 3D Cubic Hermite basis function.

This choice affected also the ventricular volume. With the use of Linear basis function there was a significant reduction of the cavity volume.

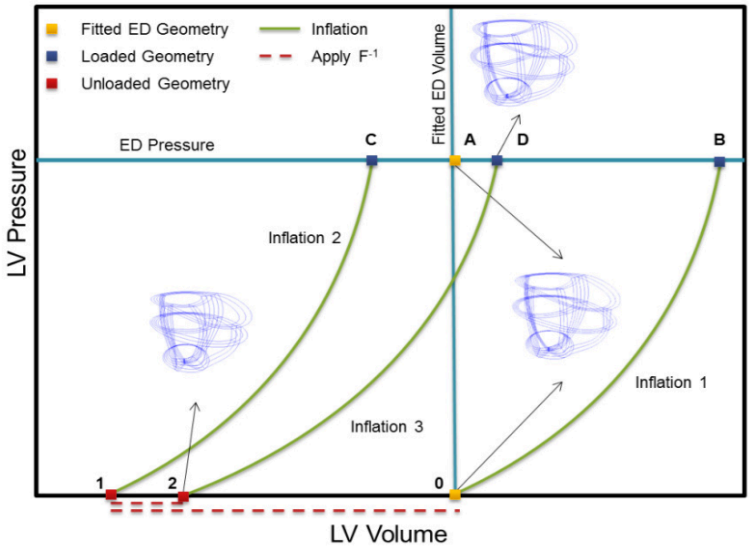

Figure 4. 16 – Algorithm to find the unloaded geometry. The initial geometry (point A in the graph) is first set to zero pressure (point 0). Then, it is inflated to the measured end-diastolic pressure (B). The deformation gradient between the inflated mesh and the fitted end-diastolic is computed (from A to B). This deformation gradient is then applied inversely to the initial estimate to get a new unloaded geometry estimate (point 1). This process is iterated until the projection error between the surfaces of the measured and loaded geometries is lower than the fitting error (final point D).

At this point, Klotz's empirical relationship [49] was used to scale the passive material parameters so that the right-ventricular cavity volume of the unloaded model matched the empirical value predicted by Klotz relation (Chapter 3, Section 3.2.2).

The second approach used to get the unloaded geometry consisted in the segmentation of MRIs at 1/3 of the diastolic timeframe, followed by the mono-ventricular mesh fitting.

Passive inflation was simulated starting from the unloaded geometry to reach the end-diastolic one. Material parameters were manually changed to get an exponential pressure-volume curve. The same factor was used to scale the isotropic stiffness (a) and the fiber stiffness (a_f), as well as for b and bf.

4.6.2 Full beat simulation

After the passive material parameters and unloaded geometry were obtained, the contractile parameters and the hemodynamic parameters were determined to match the measured peak right ventricular pressures and end-systolic volume.

In order to simulate the cardiac cycle, pressure boundary conditions were added to the cardiovascular model. The '*single closed loop for LV only'* hemodynamic model was used for the simulation. It consists of a closed RC circuit dependent on single ventricle pressure (Figure 4.17).

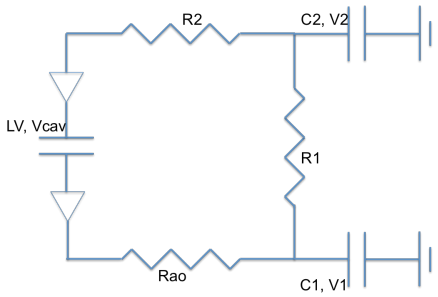

- LV = left ventricle
- Vcav = cavity volume
- Rao = aortic resistance
- qart = arterial flow
- C1,V1,R1,q1 = compliance, volume, resistance, flow of vessel 1
- C2,V2,R2,q2 = compliance, volume, resistance, flow of vessel 2

Figure 4. 17 – Schematic representation of the circulatory model.

The volume of blood circulates through two vessels in series. These represent the aorta (1) and the pulmonary vein (2). The ventricle (whose functioning is simulated by the finite element model) has two one-way valves, one at each opening.

The model has always been used for a single left ventricle. For the project, the right ventricle acts as a left ventricle, so the model was used without any change.

Similarly to the unloaded geometry simulation, the hemodynamic and active parameters were unknown. First, the simulation was performed with the default parameters (Table 4.3) from Kerckhoffs et al. [69].

These were then manually adjusted to match the simulated values of pressure and volume with those obtained from clinical measurements (at the end of systole and diastole).

		Default parameters
Hemodynamic model	**V1**	347
	V2	1062
	R1	245
	C1	33
	R2	51
	C2	433
Active model	**Lsi (μm)**	2
	Con	0
	SfAct (kPa)	80

Table 4. 3 – List of hemodynamic and active parameters used for the full beat simulation [69].

The simulation was performed using a Python script. It requires the loaded geometry (from passive inflation) and the unloaded geometry and performs the biomechanics simulation iteratively until it is reached the stable state. Sarcomeres length and contractility values are updated each time step, as described in the active contraction model.

Two different output files were obtained from the simulation. First, an Excel file containing all the components of two tensors for each Gaussian point: the second Piola-Kirchhoff stress tensor and the Lagrangian Green's strain tensor. These are 3x3 matrices that present on the diagonal, respectively, stresses and strains in the fiber direction [0,0], in the sheet direction [1,1], and in the radial direction [2,2]. Second, an Excel file containing all the hemodynamics information:

- Systolic peak pressure
- End systolic volume
- End diastolic pressure
- End diastolic volume
- Max contraction velocity index
- Min contraction velocity index
- Stroke volume
- Stroke work
- Pressure-time graph
- Volume-time graph
- Pressure-Volume loop

4.7 Data analysis

The output files of the full beat simulation were the starting point for the stroke work density and the total cardiac work analysis.

Local work density was computed using a Matlab function (*PolyArea*). It takes stress and strain tensors values, and Gaussian point coordinates and weights as input. Then, it computes the total work density as a sum of work contributions in fiber [0,0], cross fiber [1,1], and normal sheet [2,2] directions.

At the end, volumetric work was calculated by multiplying the stroke work density with the element volume. Elements were separated, according to anatomical areas, in septum and free wall side. The volumetric works of the same area were summed, and the percentage contribution on the total work was analyzed.

To further evaluate the computation of the cardiac work, it was compared with the computed P-V loop area.

Chapter 5

Results and discussion

5.1 Background

The methods described in the previous chapter have been applied to data from two children affected by Hypoplastic Left Heart Syndrome (HLHS). Cardiac MRI are collected from the Rady Children's Hospital of San Diego and used to build up the mono-ventricular patient-specific model.

This chapter shows the results for those two datasets in terms of model construction and biomechanics simulations.

In order to evaluate models' reliability, consistency between the models' intracavitary volume and the corresponding clinical measurements is quantified. Also, following the identification of the unloaded geometry and of myocardial passive mechanical properties, passive pressure-volume curves were computed by simulating passive inflation and analyzed.

As a last step, a full beat simulation was performed. Pressure-volume loops were compared vs. clinical data. The stress and strain distribution and the cardiac work were also estimated and compared vs. values extrapolated from literature in order to assess the reliability of biomechanical simulations.

5.2 Mono-ventricular model construction

In this project, MRI of two HLHS patients were collected and analyzed.

SSFP (Steady State Free Precession) cine images were obtained using a 5-element cardiac coil using breath-holds and retrospective gating. The sequence parameters for SSFP sequence were: repetition time (TR) 2.7ms, echo time (TE) 1.36ms, flip angle 60 degrees, field of view (FOV) 400mm, slice thickness 8mm, image matrix 192x256 and 30 heart phases.

Figure 5.1 clearly shows the severe underdevelopment of the left ventricle in both patients. On the other hand, the right ventricle is different in shape and bigger than the physiological one. For RCH-5-1 the right ventricle is completely deformed, elongated, and lumpy, showing a very thick ventricular wall. This evidence is consistent with the fact that it is a right ventricle that pumps blood onto the systemic circulation; it therefore plays the role of the left ventricle, and it has been deformed as a result of the high pressure levels (systolic peak pressure of 100 mmHg). Conversely, RCH-6-1 has a more spherical right ventricle and the ventricular wall is thinner than in the previous patient. This may be due to the fact that RCH-6-1 is younger than RCH-5-1, and the ventricle is deformed to a lesser extent (systolic peak pressure of 80 mmHg).

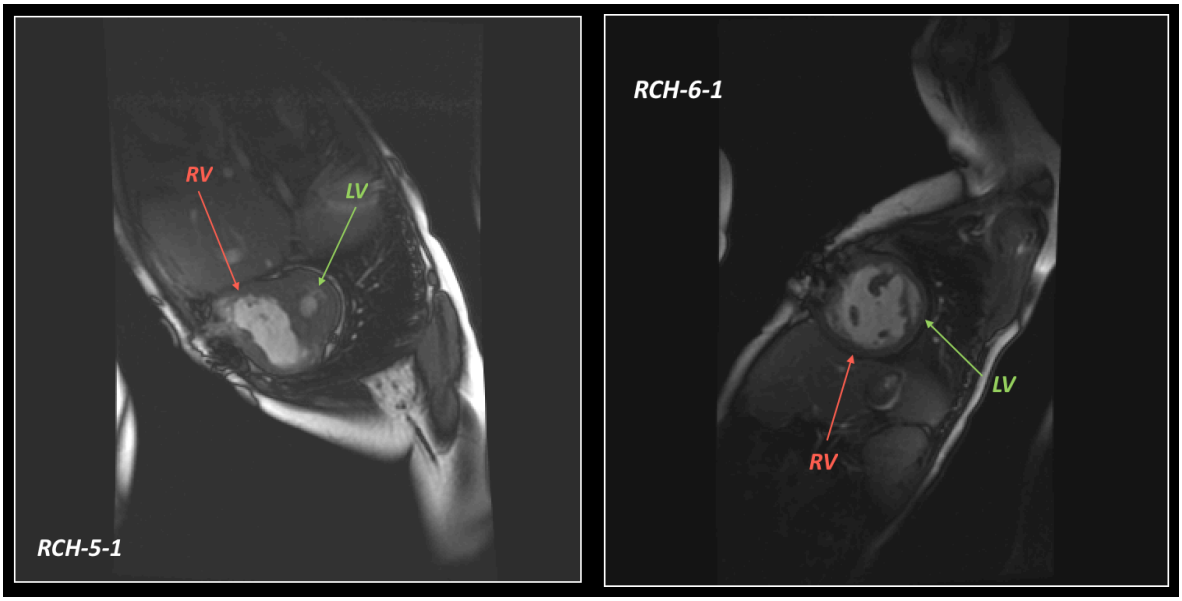

Figure 5. 1 – Cardiac MRI of two HLHS patients. On the left RCH-5-1: the RV is deformed and the ventricular wall is very thick. On the right RCH-6-1: the RV is roundish and the ventricular wall is thinner.

Only short axis images were selected, because they were considered more useful to study the right ventricle. In fact, using the short axis plane, extent and shape of the right ventricle are clearly visible. As a drawback, the ventricular apex and the valvular plane may be too poorly visible in the images or not captured at all, eventually resulting in the underestimation of the actual ventricular volume.

Due to the low resolution and the bad quality of the images, the manual segmentation of endo- and epicardium was likely affected by errors, even though great care was taken to minimize these (Figure 5.2 A-B, 5.2 E-F).

Subsequently, a template mesh characterized by only 28 elements was used for the fitting process. Due to the few elements of the mesh, it was not possible to replicate accurately the shape of the right ventricle (Figure 5.2 C, 5.2 G). The model was then imported in Continuity (Figure 5.2 D, 5.2 H).

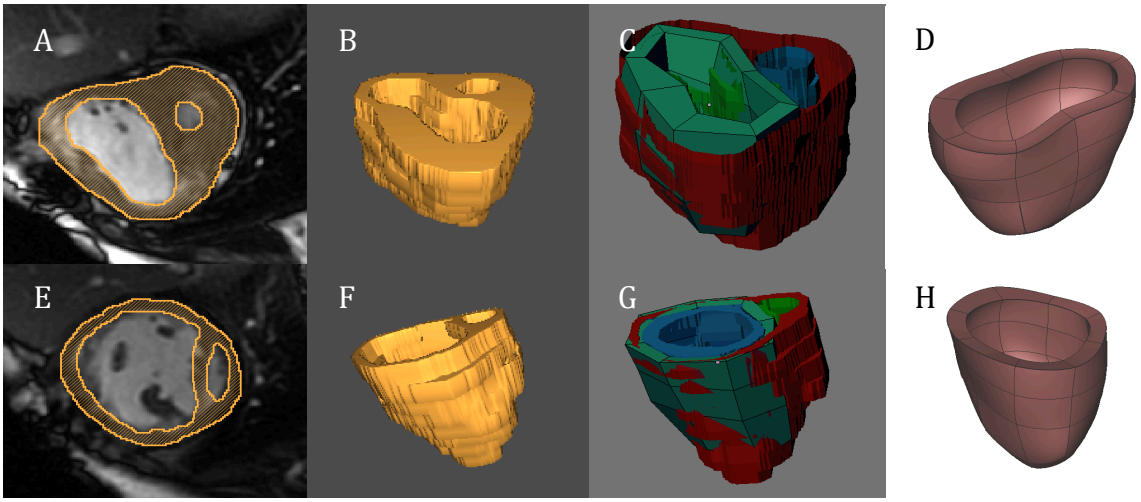

Figure 5. 2 – The figure summarizes the process to get the ED model. RCH-5-1 above and RCH-6-1 below. Starting from the left the short axis segmentation with Seg3D, the segmented patient-specific data, the fitting in Blender, and the mono-ventricular model in Continuity.

Altogether, the low image resolution and the use of a template mesh with few elements led to relevant geometric fitting errors; the reconstructed 3D models underestimated the intracavitary volume measured directly from medical images by 16.4% and 5.5% for RCH-5-1 and RCH-6-1, respectively (Figure 5.3). Of note, this error is notably smaller in the second patient; this result is likely due to the fact that the template mesh is originally a truncated prolate ellipsoid, and hence is more likely to capture the more spherical shape of RCH-6-1 better than the partially concave one characterizing patient RCH-5-1.

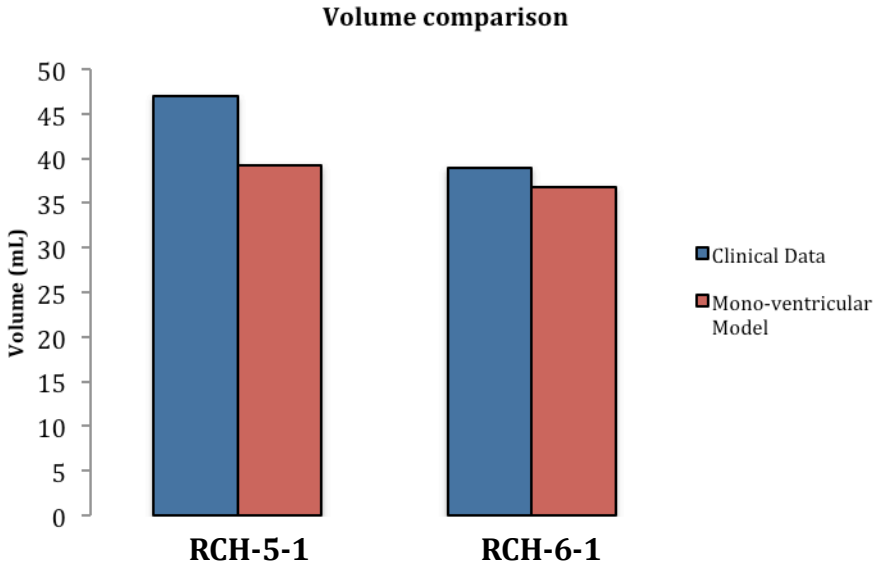

Figure 5. 3 – Bar graph showing the volume discrepancy between clinical measurements and mono-ventricular model.

5.3 Unloaded geometry

5.3.1 Unloaded algorithm analysis

The Krishnamurthy's algorithm [8] was tested to estimate the unloaded reference state. Five and six iterations were run for RCH-5-1 and RCH-6-1, respectively.

At each iteration, the pressure-volume curve of the model during passive inflation was obtained.

In order to test the convergence of the method, the loaded mesh cavity volume was evaluated.

In the last step, the end-diastolic volume obtained through the simulated inflation closely matched the value computed directly from the MRI model; the error was 0.14% and 0.7% for the two modeled ventricles (Figure 5.4), thus suggesting that the algorithm allows for error minimization between the fitted mesh and the new loaded geometry.

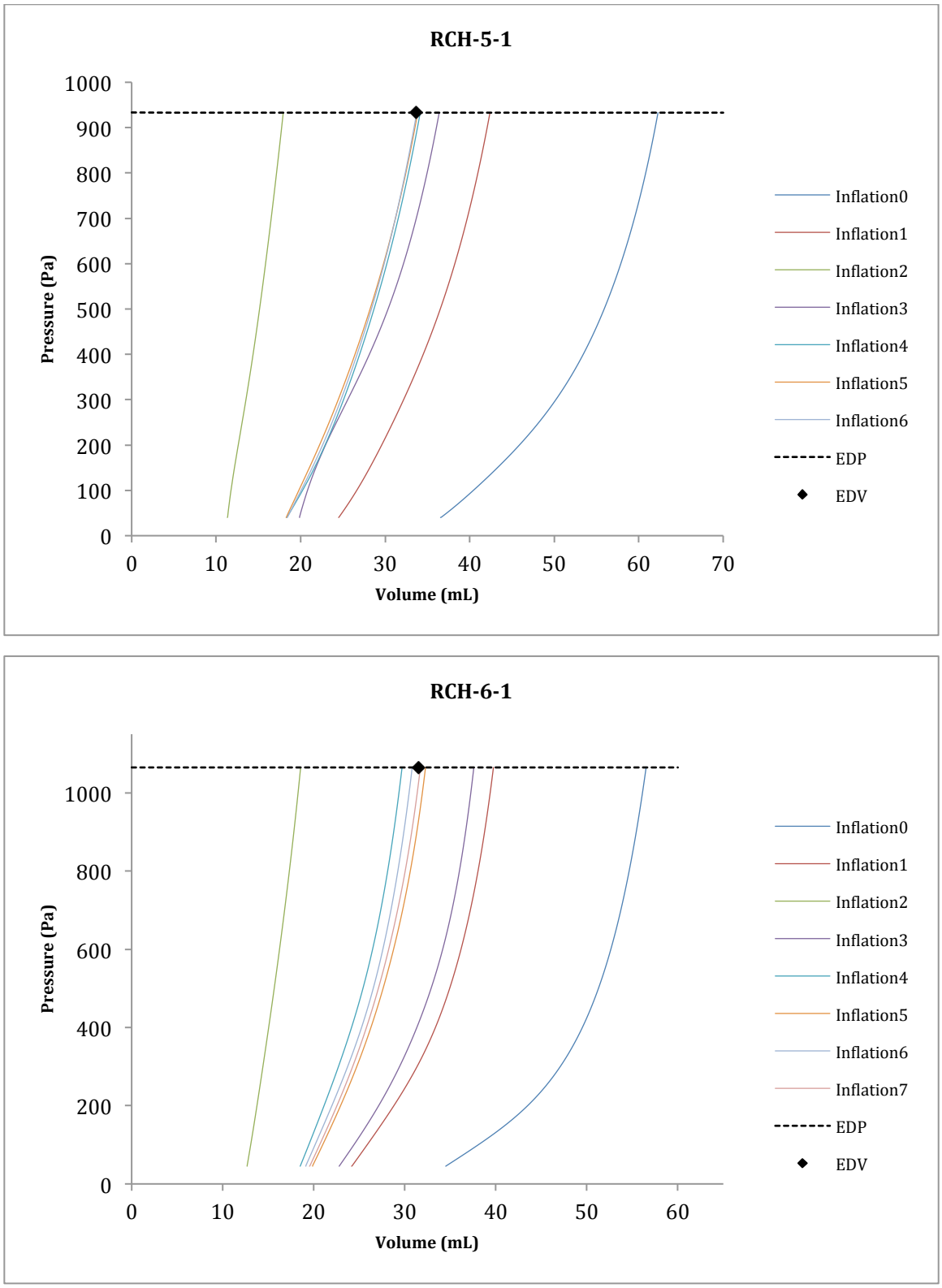

Figure 5. 4 – Pressure-volume curves of passive inflations. The black dot represents the end-diastolic volume of the constructed mesh. The last inflation curve (Inflation 6 for RCH-5-1 and Inflation 7 for RCH-6-1) closely matches that value.

The Klotz's empirical relationship [49] was used to scale the passive material parameters so that the right-ventricular cavity volume of the unloaded model matched the empirical value predicted by Klotz relation (Chapter 3, Section 3.2.2). The same factor was used to scale the isotropic stiffness (a) and the fiber stiffness (a_f), as well as for b and bf.
Table 5.1 shows the passive material parameters used to run the unloaded geometry simulation.

Passive Material Parameters	Default parameters	RCH-5-1 (modified)	RCH-6-1 (modified)
a (kPa)	0.3192	0.016	0.016
af (kPa)	0.236	0.0118	0.0118
b	9.726	19.452	19.452
bf	15.779	31.558	31.558

Table 5. 1 – Passive material parameters table. Default parameters represents the values used to get the unloaded volume. Patient-specific values (used to match Klotz) are reported in the other two columns.

The comparison between the computed pressure-volume curves and the Klotz one clearly shows that, despite yielding the correct end-diastolic volume, the two models are characterized by an excessively stiff behavior (Figure 5.5). Such issue was very pronounced before scaling the passive constitutive parameters of the myocardium, and scaling them reduced only slightly this issue. Two possible reasons may have caused this result.
The first one is that the Klotz equation holds for an adult and healthy left ventricle, which has a different shape and different material properties as compared to pediatric right ventricles affected by HLHS. As a result, the Klotz curve might be not fully adequate as term of comparison.
The second possible cause of mismatch is that the Krishnamurthy's algorithm has been conceived for the left ventricle, whose shape is very different from the shape of the right ventricle. Hence, the unloaded configuration of the model may have been estimated incorrectly. This potential issue is strongly suggested by the result obtained for patient RCH-5-1, whose unloaded ventricular wall looks completely buckled, with two opposite sides unrealistically overlapping each other (Figure 5.6 A-1).

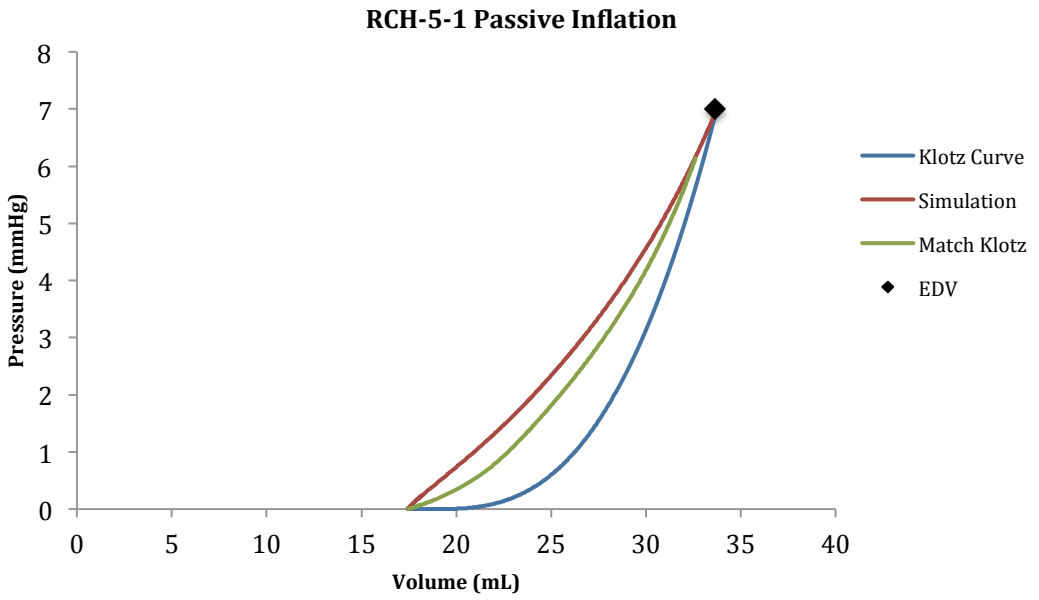

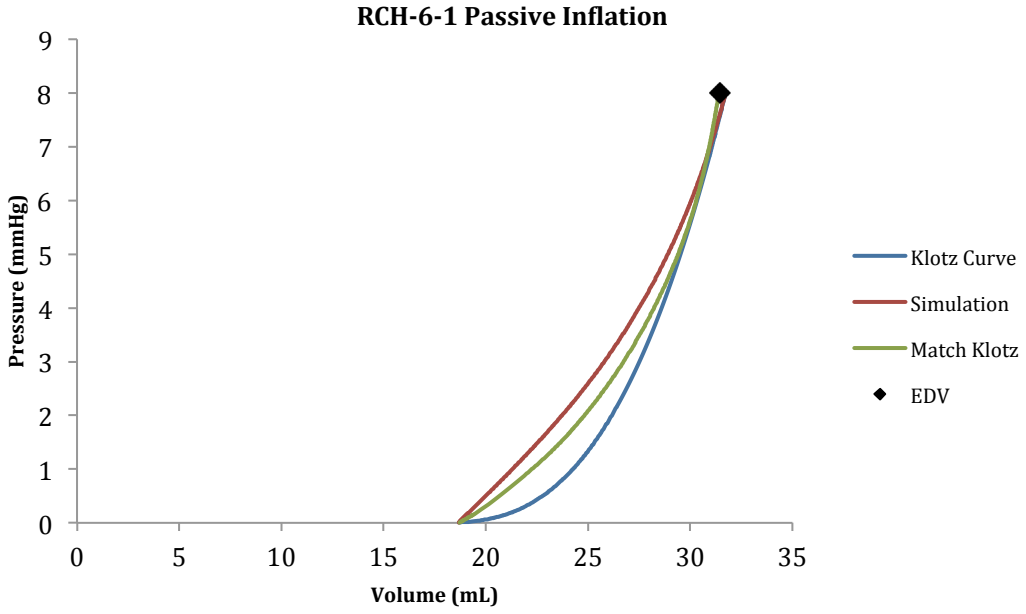

Figure 5. 5 – Passive inflation curves. In blue the empirical Klotz curve, in red the curve obtained using the default material parameters and in green the one after changing the passive material properties. The EDV volume refers to the fitted model volume.

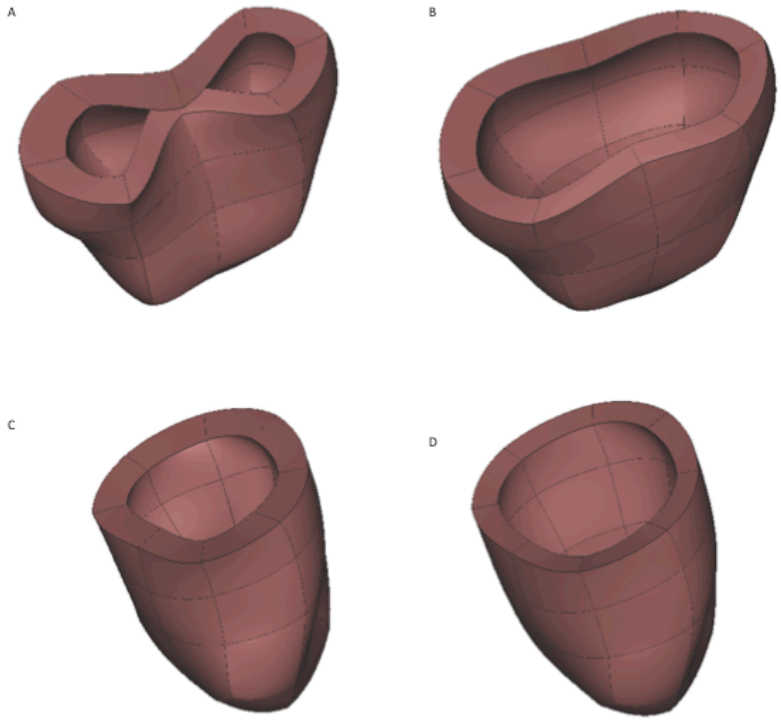

Figure 5. 6 – Unloaded and loaded geometries after the algorithm. **A-B)** Unloaded and loaded geometries for RCH-5-1; **C-D)** Unloaded and loaded geometries for RCH-6-1.

5.3.2 Unloaded volume from MRI

Because of the stiffer passive inflation curves and the mesh overlapping for RCH-5-1, the Krishnamurthy method was considered not acceptable for HLHS patient. Another approach was used to get the unloaded geometry. The entire process of MRIs segmentation and mesh fitting is shown in Figure 5.7. The resulting discretized geometry was considered as the unloaded configuration of the ventricle.

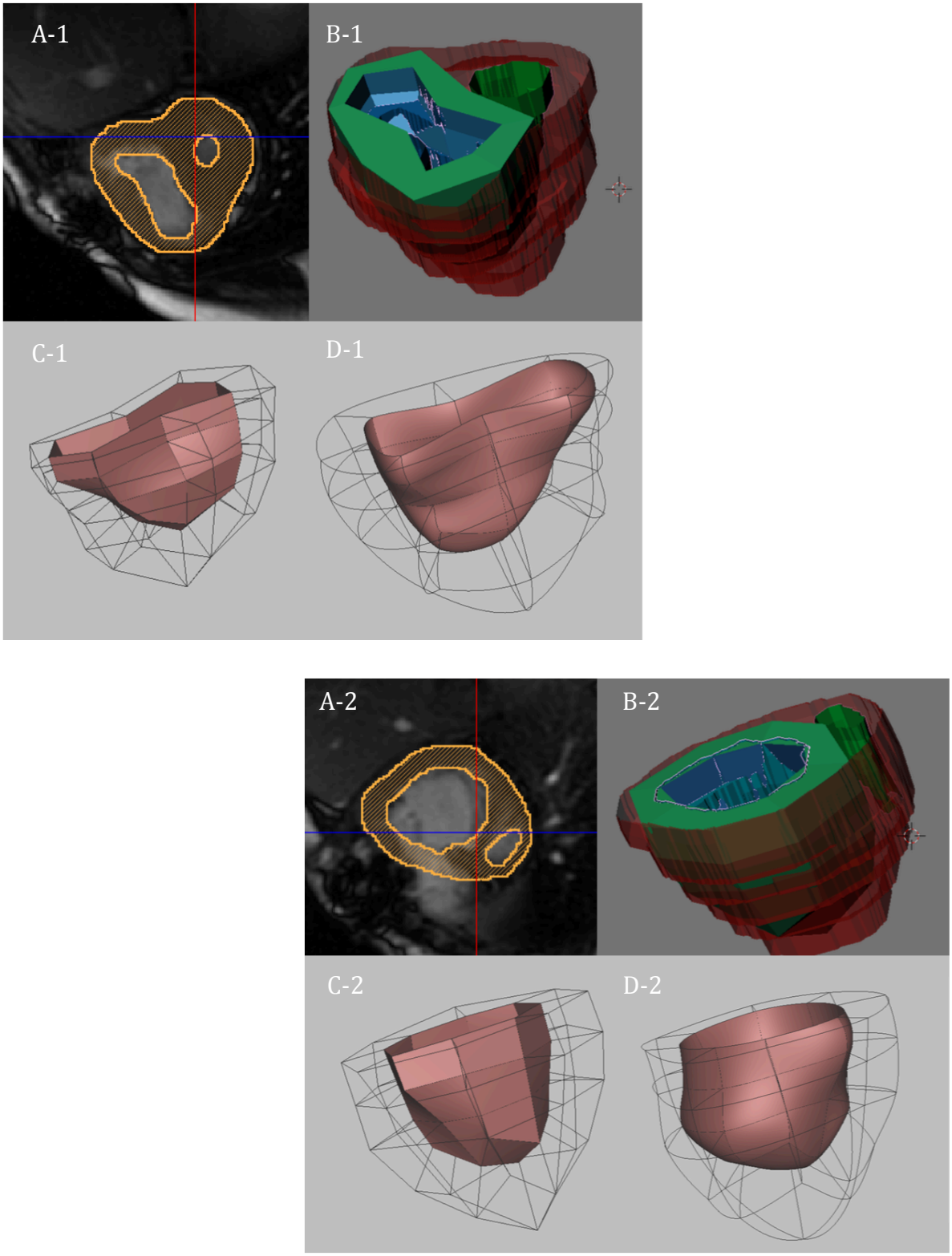

Figure 5. 7 – From the MRI segmentation to the mono-ventricular unloaded model. **A)** Segmentation (Seg3D) of images at 1/3 of diastole. **B)** Fitting process (Blender) of a mesh template with patient-specific data. **C)** Model in Continuity using 3D-Linear basis functions. **D)** Model in Continuity using 3D-Hermite basis function. Numbers 1 and 2 represent patients RCH-5-1 and RCH-6-1, respectively.

Table 5.2 lists the passive material parameters used for the simulations. Only three combinations of *a* parameters and *b* parameters allowed for obtaining the correct end-diastolic volume:

Case 1) Material with negligible stiffness (a and a_f close to zero).

Case 2) Non-physiological behavior of the myocardium (change in concavity).

Case 3) Decrease in bulk modulus.

The last case was selected to describe passive material parameters of the right ventricle for HLHS patients. It consisted of a more compliant myocardium than the normal one (see default parameters in Table 5.1). In fact, default parameters refer to a child physiologic left ventricle. Right ventricle is less rigid than the left one [4]. Passive inflation curves of case 3 are shown in Figure 5.8.

	RCH-5-1			**RCH-6-1**		
Passive Material Parameters	**Case 1**	**Case 2**	**Case 3**	**Case 1**	**Case 2**	**Case 3**
a (kPa)	0.00003	0.019	0.0032	0.00003	0.019	0.0016
af (kPa)	0.00002	0.015	0.0024	0.00002	0.015	0.0012
b	11.67	4.86	16.53	11.67	3.24	15.56
bf	18.93	7.89	26.82	18.93	5.26	25.25
Bulk modulus (kPa)	350	350	50	350	350	40

Table 5. 2 – Passive material parameters used for the passive inflation simulations starting from the unloaded geometries segmented and fitted from MRI.

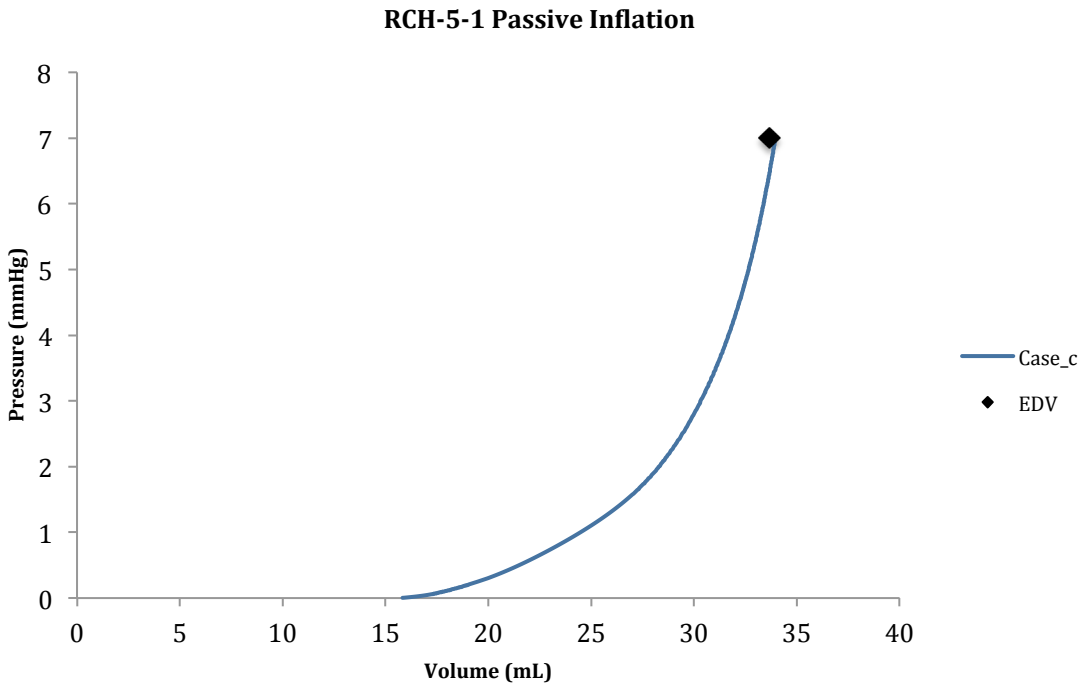

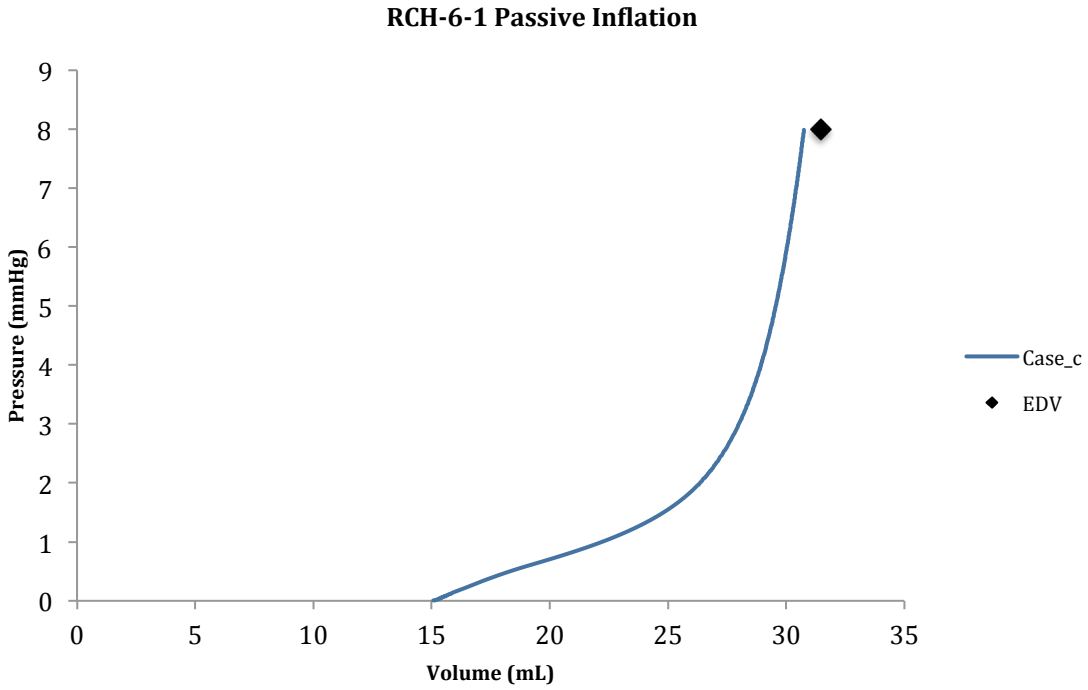

Figure 5. 8 – Passive inflation curves in case 3. These start from the unloaded volume (computed from the unloaded model) and closely match the EDV of the fitted model.

5.4 Full Beat simulation

After the identification of the passive material constitutive parameters allowing for replicating the theoretical pressure-volume behavior during passive inflation, the simulation of an entire cardiac cycle was performed.

Passive material constitutive parameters found in the diastolic simulation (Table 5.2, case 3) were used in the constitutive model. For what concerned the hemodynamic and dynamic model, Kerckhoffs' parameters [69] were first scaled accordingly with the ventricular volume. Then, these were adjusted to get patient-specific values matching the clinical data (end-diastolic and end-systolic pressure and volume). Table 5.3 lists all the hemodynamic and active contractile values.

In particular, it was noticed that the changes in volume between diastole and systole were mostly influenced by vascular resistances; these were hence tuned to match clinically measured end-diastolic and end-systolic volumes. Instead, systolic peak pressure was mostly influenced by the active scaling factor, which was tuned to match the clinical measurement from catheterization.

		Default parameters	**RCH-5-1**	**RCH-6-1**
Heart Rate		70	95	94
Circulation model (Hemodynamic parameters)	**V1**	347	100	100
	V2	1062	430	580
	R1	245	800	1000
	C1	33	12	15
	R2	51	80	100
	C2	433	100	120
Dynamic model (Active parameters)	**Lsi (μm)**	2	2.04	1.96
	Con	0	$6.62\ e^{-8}$ (mean value)	$8.94\ e^{-8}$ (mean value)
	SfAct (kPa)	80	170	100

Table 5. 3 – This table shows all the values used for the full beat simulation. In the circulation model, resistance, compliance and volume of vessel 1 and 2 were adjusted. In the dynamic model, the active scaling factor (SfAct), the length of the sarcomeres (Lsi) and the contractility parameter (Con) were changed.

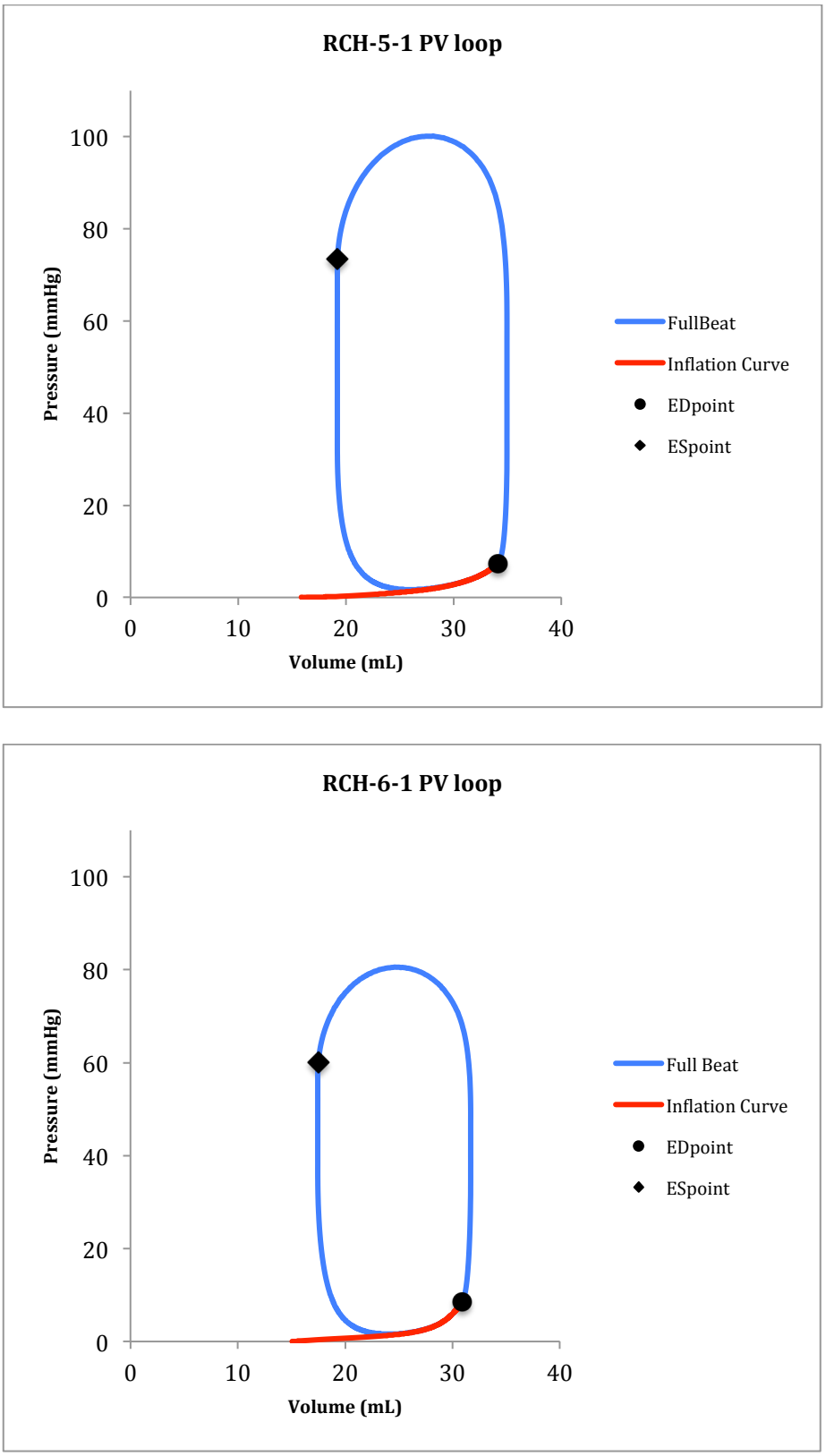

Figure 5. 9 – Pressure-Volume loop after the full beat simulation. In red the passive inflation curve and in blue the cardiac cycle. ED and ES point are highlighted.

For the first beat, default values were used for the length of contractile element (Lsi) and contractility (Con). Then, these were updated and saved in an Excel file, referring to each node (equations for sarcomere length and contractility are shown Chapter 4, Section 4.5.4). The Python script uploaded the updated values as input for the following cardiac cycle. In Table 5.3 the mean values are presented for Lsi and Con.

Figure 5.9 shows the closed Pressure-Volume loops for RCH-5-1 and RCH-6-1. In both cases, the diastolic portion of the P-V loop replicates the corresponding pressure-volume curve obtained through passive inflation. This evidence means there is a good agreement between the passive and active contraction simulations.

Furthermore, Table 5.4 points out that the ventricular pressure computed at different time-points throughout the cardiac cycle was consistent with clinical measurements, whereas a discrepancy in the end-diastolic and end-systolic volume between clinical measurements and simulation was obtained, probably due to an overly stiff passive behavior in the simulation; the ventricle is less compliant, and hence increases its volume less than it should during diastolic filling.

Pressure-time and volume-time charts (Figure 5.10) were also computed from hemodynamic data. The curves behavior is credible if compared with the curves presented in Chapter 2.

	RCH-5-1		**RCH-6-1**	
	Measured	*Simulated*	*Measured*	*Simulated*
EDV (mL)	47	34.13	39	30.9
EDP (mmHg)	7	7.37	8	8.52
Systolic peak (mL)	100	100.16	80	80.48
ESV (mL)	23	19.23	21	17.5

Table 5. 4 – Simulated pressure and volume values are compared with the clinical measurements.

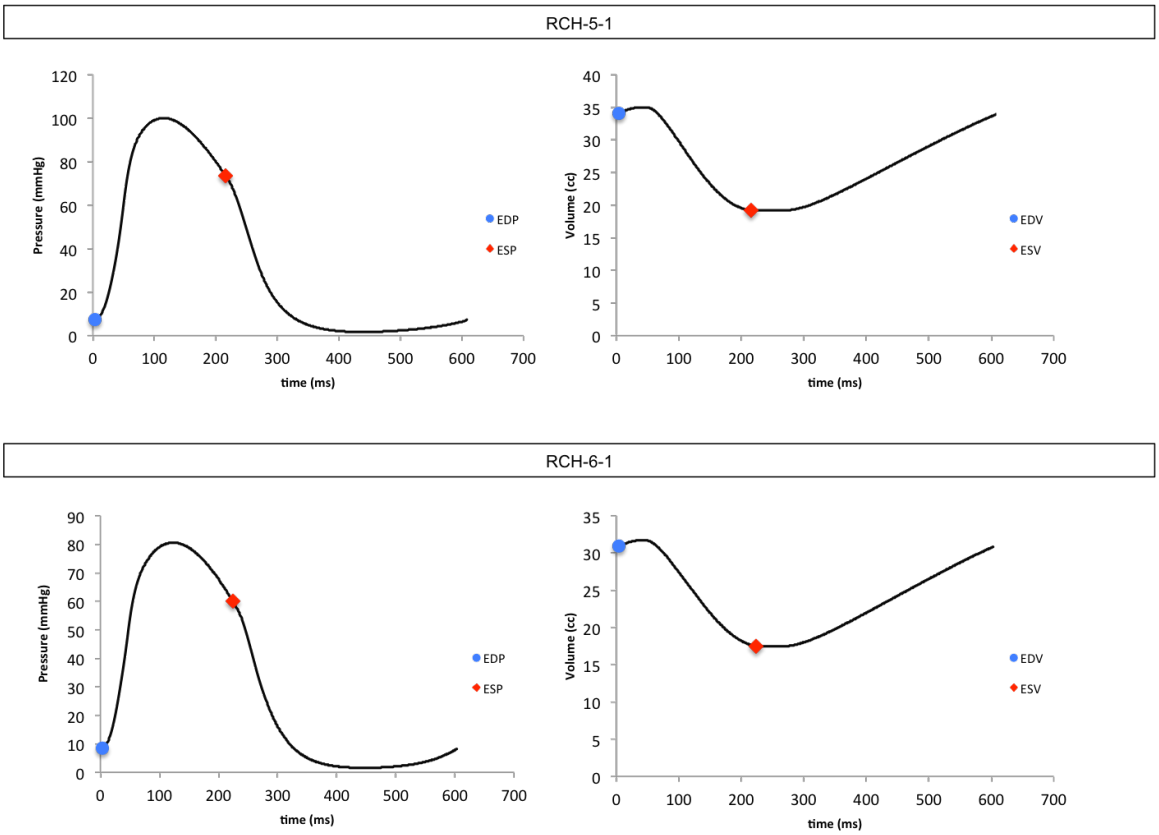

Figure 5. 10 – Pressure vs time on the left and Volume vs time on the right for both patients. Highlighted the ED volume and pressure (blue) and ES volume and pressure (red).

5.5 Stress and strain distribution

Stress and strain distributions over the whole ventricular wall were calculated at end-diastole, end-systole, and peak systole. All of the components of the second Piola-Kirchhoff stress tensor and of the Lagrangian Green strain tensor were collected. Then, using Continuity, the normal component in the fiber direction was rendered on the screen (Figure 5.11). Table 5.5 lists the maximum, minimum, and average value for both tensors.

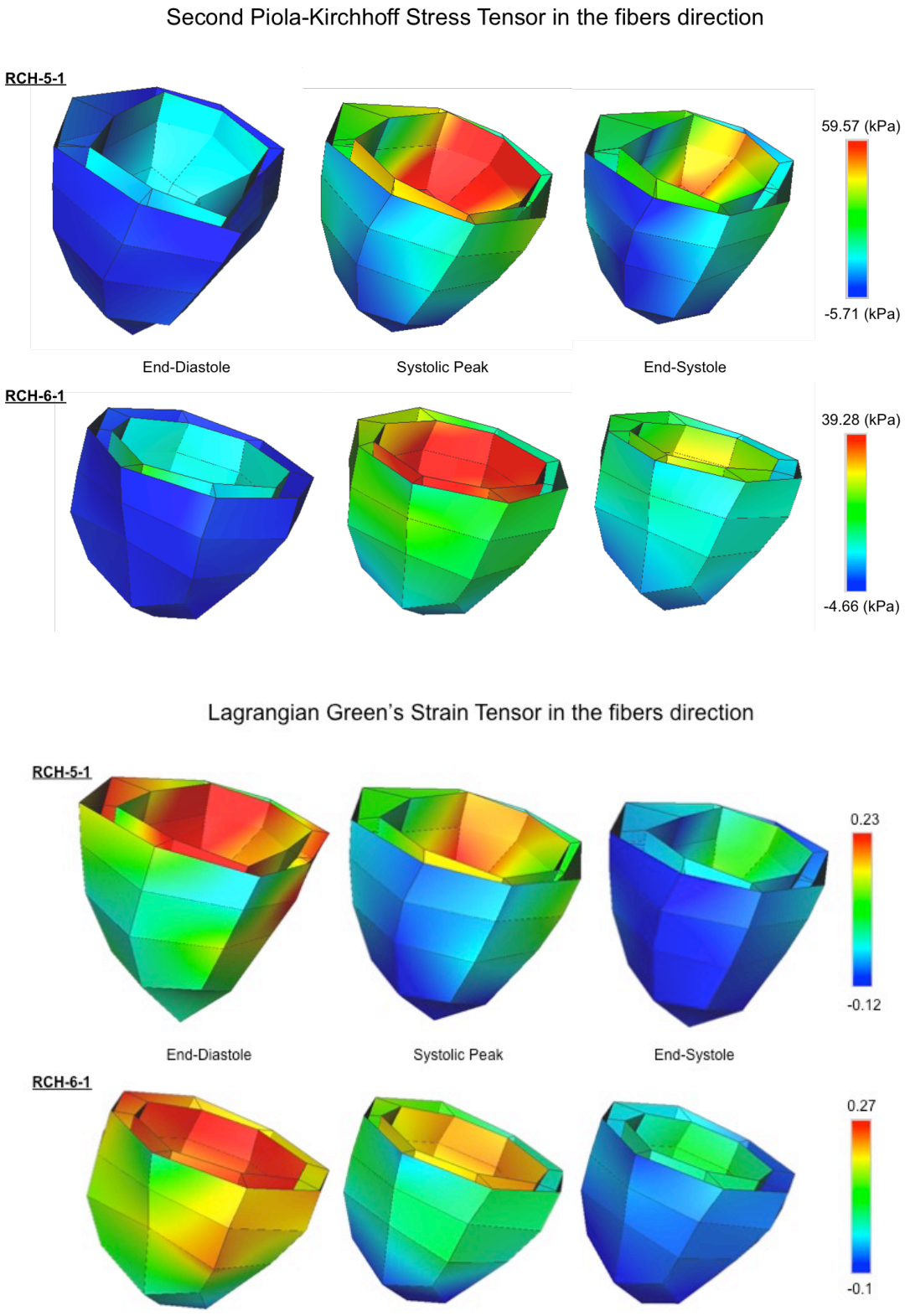

Figure 5. 11 – Colour-coded maps of calculated stress and strain tensors distributions in the fibers direction at end-diastole, systolic peak, and end-systole.

	RCH-5-1			RCH-6-1		
	ED	*SP*	*ES*	*ED*	*SP*	*ES*
Stress_max (kPa)	9.93	59.57	38.44	8.46	39.28	24.14
Stress_min (kPa)	-5.71	0.07	-2.12	-4.66	4.42	1.37
Average stress (kPa)	1.45±5.9	28.91±21.2	17.23±14.4	2.63±5.6	22.53±12.7	13.26±8.3
E_max	0.23	0.16	0.01	0.27	0.21	0.05
E_min	0.002	-0.11	-0.12	0.04	-0.08	-0.04
Average strain	0.13±0.08	0.12±0.09	-0.06±0.04	0.18±0.08	0.08±0.1	0.03±0.05

Table 5. 5 – Maximum, minimum, and average value of the Second Piola-Kirchhoff stress tensor (Stress) and the Lagrangian Green's strain tensor (E) in the fibers direction.

Maximum stress is mostly located in the anterior ventricular wall in all of the three considered time-points of the cardiac cycle, except for the end-diastolic point for RCH-6-1 that presents the maximum value in the posterior wall. Instead, the minimum stress is located in the Septum and Lateral side of the ventricle for both patients.

For RCH-5-1, the strain distribution follows the same values of the myofibres stress. For RCH-6-1, instead, the strain distribution is homogeneous on the endocardial and epicardial surfaces. The difference between the two subjects could be due to the elongated shape of the first analyzed ventricle, as compared to the more spherical shape of the second one.

The computational values of stress and strain were compared with literature values [70-72]. These are mostly referred to as myofibres stress and strain in the left ventricle. For HLHS patients, it is important to consider that the right ventricle pumps blood into the systemic circulation. It plays the role of the left ventricle, with comparable systolic peak pressure. Hence, comparison between simulated right ventricle and literature left ventricle values was considered adequate.

Myofibres averaged stress value at end-diastole, end-systole, and systolic peak was compared with the myofibres stress-strain loop computed by Kerckhoffs et al. [70]. Here, fiber stress and strain are evaluated in different areas of the ventricular wall at the midwall equator. Figure 5.12 shows that the maximum systolic peak stress was located in the

anterior ventricular wall. Its value was around 23 kPa. The end-diastolic and end systolic stress range between 2 - 5 kPa, and 16 - 20 kPa, respectively.

These values are in agreement with the computational simulations made in this project.

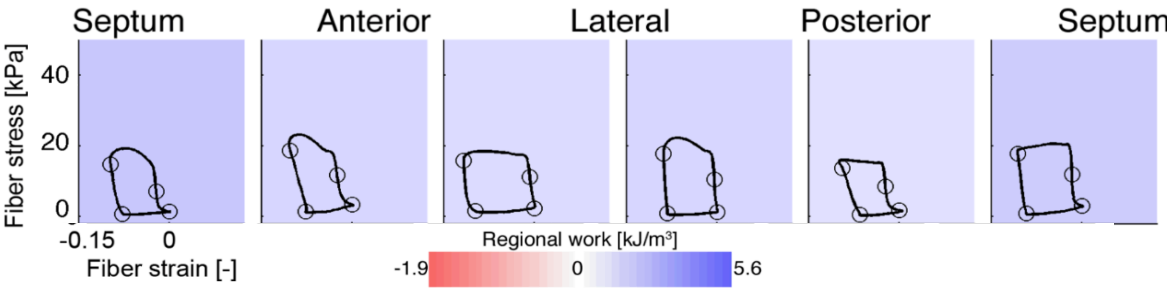

Figure 5. 12 – Left ventricle fiber stress as a function of fiber strain during the cardiac cycle at the midwall equator. The areas of the loop represent fiber regional work. Circles denote opening and closing of valves [70].

Strain values were then compared with the work of Dorri et al. [72]. They estimated the average values of the principal strain in basal, equatorial, and apical areas during ventricular systole of a left ventricular model with effective compressibility (K = 70 kPa). In most regions the maximum strain was found to vary around 0.20, the minimum strain around -0.27, both within a standard deviation of 0.07 (Figure 5.13). These values are compatible with the computational results from the full beat simulation.

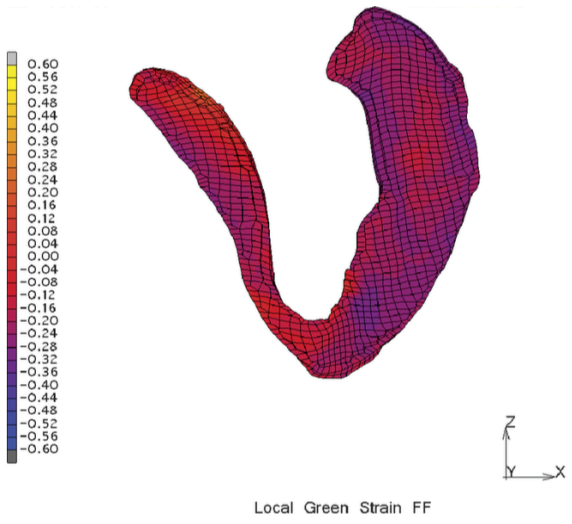

Figure 5. 13 – Colour-coded maps of strain pattern in a septal-lateral long-axis section at end-systole. The figure shows the strain distribution along fiber direction (Eff) [72].

5.6 Cardiac work

Through the stress and strain distribution, the stroke work density (SWD) was computed. It is the area of the myofibres stress-strain curve, and is defined as the contractile myofibres work per unit of tissue volume per beat. The stroke work per unit volume was calculated in simulations as the product of the active tension and the strain, where the activate tension and strain are the second Piola Kirchhoff Stress and the Green strain rate, respectively. Here, the averaged values are reported.

RCH-5-1 ***SWD*** $= 4.76 \pm 2.22\ kJm^{-3}$
RCH-6-1 ***SWD*** $= 5.08 \pm 3.2\ kJm^{-3}$

These values were compared with those from previous studies on mono-ventricular [70, 71] or biventricular [73] models. The simulation results are largely comparable with the values reported in these works.
Then, the work density was multiplied by the elements volume and the percentage contribution on the total work was calculated for the septum and free wall (Figure 5.14). The septum performs less work than the free wall, consistently with findings previously reported from literature [70, 73].

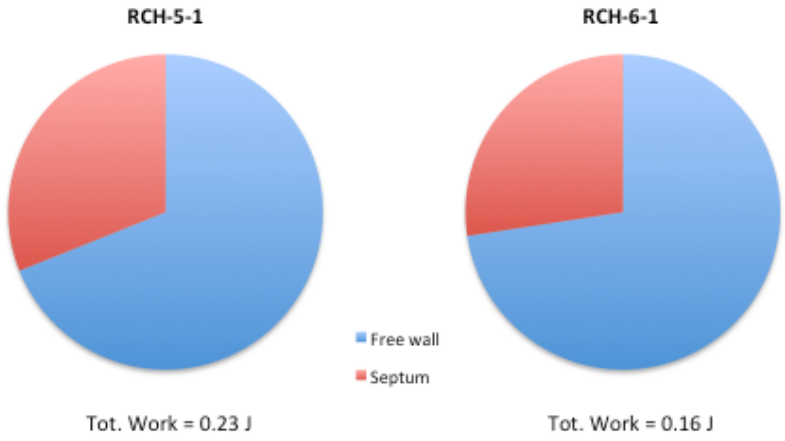

Figure 5. 14 – Percentage contribution of the septum (red) and the free wall (blue) to the total work.

To further evaluate the computation of the cardiac work, it was compared with the computed P-V loop area. Figure 5.15 shows that there is good agreement between the computed stroke work and the PV loop area. Percentage errors of 15% and 14% resulted for patients RCH-5-1 and RCH-6-1, respectively.

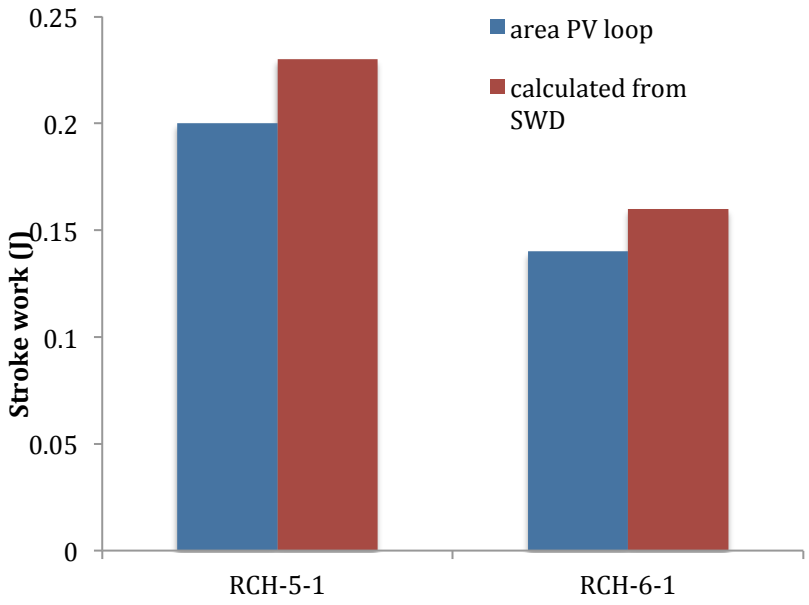

Figure 5. 15 – The stroke work calculated from the stroke work density is compared with the PV loop area. The bar graph shows that there is a small error between the values.

Chapter 6

Conclusions and future improvements

This project focused on the development of patient-specific finite element models of the right ventricle (RV) in a preliminary cohort of patients suffering from Hypoplastic Left Heart Syndrome (HLHS).

The realization of patient-specific anatomic models was initially provided by a semi-automatic segmentation of short axis MRI images. Subsequently, a manual fitting was used to adjust a mono-ventricular mesh template to the patient-specific segmentation data. Although the method was considered satisfying for the project goal, some improvements could be done to optimize the model construction. The use of a mono-ventricular mesh template characterized by low elements number implicates a rough fitting, especially for irregular ventricular shape. Increasing the elements number would provide a more accurate geometry.

The models were used to simulate the RV mechanics.

Passive diastolic filling simulation allows the valuation of passive material properties of the myocardium. Two different approaches were tested. The Krishnamurthy's algorithm was considered inappropriate for the right ventricle behavior. Changing the boundary conditions could improve the results. Still, the method will be unsuitable because of the comparison between the Klotz curve (estimated for left ventricle) and the right ventricular inflation curve. On the other hand, the unloaded volume and geometry estimation from MRI has been proved to be a valid method.

Hemodynamic and active material parameters were estimated during the full beat simulation. These were adjusted to match the patient's end-diastolic pressure-volume relations, and the left and right- ventricular cavity pressures measured in the patient, respectively. Then, in order to study the accuracy and reliability of the models, the stress and strain distribution, as well as the right ventricular work, were calculated.

An important aspect to be considered is that the determination of the active and the hemodynamic parameters are performed independently. This might lead to some variation between the estimated and actual parameters. The problem can be better solved with the help of an optimization algorithm that can find the right parameters matching the model output with measurements. In addition, the use of a smoother mesh could result in more accurate stress and strain distribution, and accordingly stroke work density and cardiac work. Anyway, the computed values were compared and considered to be in agreement with values from literature.

In conclusion, the viability of creating detailed patient-specific models to perform biomechanics simulations was demonstrated. The models are capable of replicating patient-specific global cardiac function. These could be used to study the effect of different therapies with the goal of predicting treatments for heart disease.

In particular, in the Cardiac Atlas Project (CAP), models will be used to identify differences between systemic left and right ventricular physiologies, to compare Congenital Heart Disease (CHD) ventricles with normal hearts and to analyze changes in shape and wall motions over time in single ventricle CHD. These comparisons will be used to test the hypothesis that indices of ventricular shape remodeling in single ventricle pathologies both over time and compared with normal ventricles will correlate with differences in regional mechanical function between the cohorts.

The new atlas-based anatomic models of CHD will be used to simulate both cardiac mechanics and fluid structure-interactions in single ventricle pathologies; thus allowing the potential derivation of new early markers of compensatory or maladaptive remodeling.

Quantitative mechanistic analyses of single ventricle CHD may identify earlier and more reliable indicators of adverse remodeling and inform more effective treatment to prevent disease progression. In all single ventricle physiologies, effective diastolic filling is critical to maintain forward Fontan flow. Since adequate measures of single ventricle diastolic function are lacking, fluid-structure interaction (FSI) models will be used to identify potential early markers of diastolic heart failure in single ventricle CHD and to test the hypothesis that increased diastolic flow stagnation may be an early marker of diastolic failure in single ventricle disease.

Patient-specific finite element models of a subset of single LV and single RV patients will also be used to test the hypothesis that systolic wall stress is higher in single RV than single LV patients, and high wall stress correlates with higher incidence of heart failure in single RV physiology.

Appendix A – Finite element method

To approximate a set of points by a continuous function, a popular method is to use a polynomial expression such as $u(x) = a + bx + cx^2 + ..$ and then to estimate the coefficients *a, b, c*,... to obtain the best approximation to the field variable *u(x).*

Since high-order polynomials tend to oscillate unphysically, it is useful to divide a large domain into smaller subdomains and use low-order piecewise polynomials over each of them, these subdomains are the finite elements. For example, a field variable *u(x),* may be represented by several linear elements as illustrated in the top of Figure A.1. To ensure continuity of *u(x)* across elements, also called *C0* parametric continuity, it is necessary to impose constraints across elements. Re-parameterizing the linear function from monomial coefficients a and b in the first element in terms of nodal values of u at each end of the element (*u1* and *u2*) gives: $u(\varepsilon) = u_1(1 - \varepsilon) + u_2\varepsilon$ where $\varepsilon \in (0; 1)$ is a normalized measure of distance along the one-dimensional element. See the central illustration of Figure A.1. Parametric *C0* continuity means that the curves are joined at the join point. Sometimes it is desirable to use interpolation that also preserves continuity of the derivative of field variable *u* with respect to the element coordinate ε_1 across element boundaries. This can be done by adding a nodal parameter, being the derivatives $(\frac{\partial u}{\partial \varepsilon})$. The basis functions are chosen such that the derivative of *u2* in element 1 is the same as the derivative of *u1* in element 2, see the bottom of Figure A.1. These elements are used in the cubic Hermite mesh. With *C1* continuity the first derivatives are equal, with *C2* continuity the first and second derivatives are equal.

Besides parametric continuity (*C0, C1, C2*), there is also geometric continuity (*G0, G1, G2*). Geometric continuity requires the geometry to be continuous, the derivatives have the same direction, but not necessarily the same magnitude.

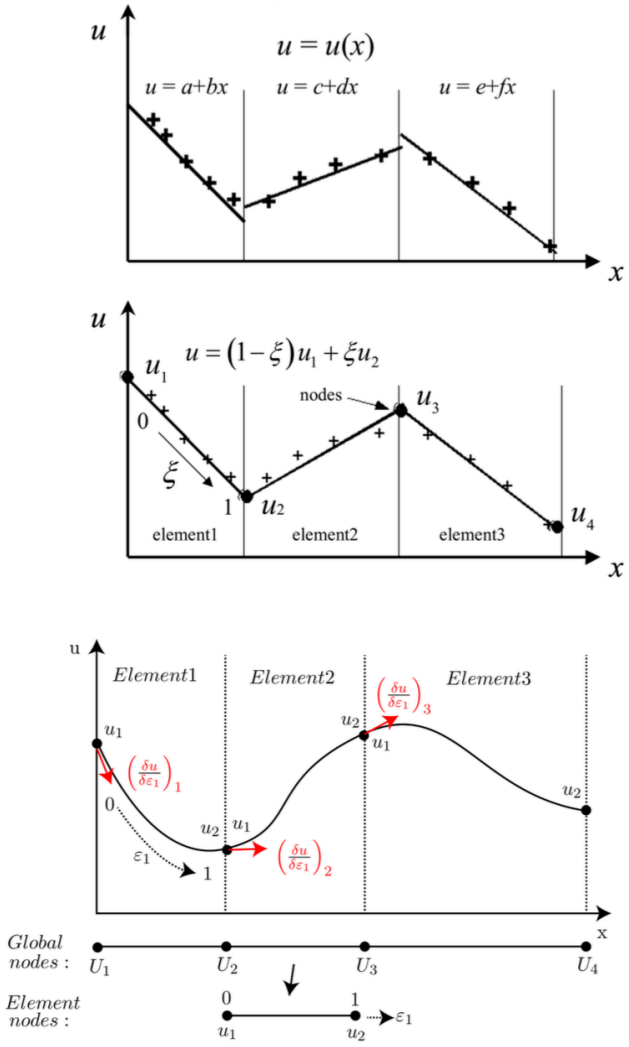

Figure A. 1 – Elements with different interpolation methods. Top: no continuity over elements. Middle: continuity of nodal values over elements. Bottom: continuity of the derivative of nodal field over elements.

Cubic Hermite mesh

Using Cubic Hermite interpolation provides higher-order continuity by sharing the derivative of the field variable u with respect to the element coordinate $\varepsilon_{1,2,3}$ across element boundaries. This is achieved by including additional nodal parameters $\frac{\partial u}{\partial \varepsilon_{1,2,3}}$($\varepsilon_{1,2,3}$ are the curvilinear element coordinates). The basis functions must comply with:

$$\left.\frac{\partial u}{\partial \varepsilon}\right|_{\varepsilon=0} = \left(\frac{\partial u}{\partial \varepsilon}\right)_{u1} = u1' \quad \text{and} \quad \left.\frac{\partial u}{\partial \varepsilon}\right|_{\varepsilon=1} = \left(\frac{\partial u}{\partial \varepsilon}\right)_{u2} = u2'$$

Because *u* is shared between adjacent elements, derivative continuity is ensured, e.g. *u1'* of element 2 is equal to *u2'* of element 1. The cubic Hermite basis functions are thus derived from:

$$u(\varepsilon) = a + b\varepsilon + c\varepsilon^2 + d\varepsilon^3, \qquad \frac{\partial u}{\partial \varepsilon} = b + 2c\varepsilon + 3d\varepsilon^2$$

Subject to the constrains:

$$u(0) = a = u1$$
$$u(1) = a + b + c + d = u2$$
$$\frac{\partial u}{\partial \varepsilon}(0) = b = u1'$$
$$\frac{\partial u}{\partial \varepsilon}(1) = b + 2c + 3d = u2'$$

Solving these equations gives the following cubic Hermit basis functions (Figure A.2):

$$u(\varepsilon) = \varphi_1^0(\varepsilon)u1 + \varphi_1^1(\varepsilon)u1' + \varphi_2^0(\varepsilon)u2 + \varphi_2^1(\varepsilon)u2'$$

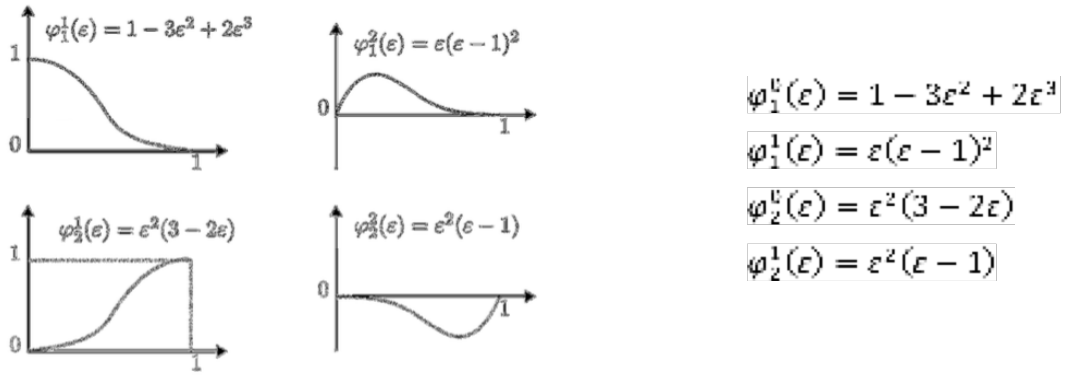

Figure A. 2 – Cubic Hermite basis functions.

A three dimensional tricubic Hermite element requires eight derivatives per node:

$$u, \frac{\partial u}{\partial \varepsilon_1}, \frac{\partial u}{\partial \varepsilon_2}, \frac{\partial u}{\partial \varepsilon_3}, \frac{\partial u^2}{\partial \varepsilon_1 \varepsilon_2}, \frac{\partial u^2}{\partial \varepsilon_1 \varepsilon_3}, \frac{\partial u^2}{\partial \varepsilon_2 \varepsilon_3}, \frac{\partial u^3}{\partial \varepsilon_1 \varepsilon_2 \varepsilon_3}$$

Appendix B – Active material model

The generation of active stress in the fiber direction is calculated by the Arts model of sarcomere mechanics [52], in which the length of the contractile element (L_{sc}) and a time-variant contractility parameter (C) were state variables.

The normalized length of the series elastic element (L_{sNorm}) is calculated by:

$$L_{sNorm} = (L_s - L_{sc})/L_{SerEl} \quad \text{(B1)}$$

Where L_s is sarcomere length and L_{SerEl} length of the series elastic element during isometric contraction.

The contractile element velocity (dL_{sc}/dt) is calculated by:

$$\frac{dL_{sc}}{dt} = \begin{cases} \dfrac{L_{sNorm} - 1}{b_{hill} \cdot L_{sNorm} + 1} v_{\max} & L_{sNorm} \le 1 \\ \dfrac{L_{sNorm} - 1}{b_{Hill} \cdot L_{sNorm} + 1} v_{\max} \cdot e^{a_{Hill}(L_{sNorm} - 1)} & L_{sNorm} > 1 \end{cases} \quad \text{(B2)}$$

This contractile element velocity is a modification from Lumens et al. [53], which yields a hyperbolic Hill-relation between shortening velocity and force.

Contractility C is described by

$$\frac{dC}{dt} = \frac{1}{\tau_r} \cdot C_L \cdot f_{rise} + \frac{1}{\tau_d} \cdot \frac{C_{rest} - C}{1 + e^{(T-t)/\tau_d}} \quad \text{(B3)}$$

Where:

t is time elapsed since electrical activation;

$$C_L = \tanh(2 \cdot (L_{sc} - L_{s0})^2) \quad \text{(B4)}$$

regulates contractility dependence on contractile element length;

$$f_{rise} = 0.02(8 - x)^2 x^3 e^{-x} \quad \text{(B5)}$$

with x=min(8,max(0,t/τ_r) regulates rise of contractility and

$$T = \tau_{sc}(0.29 + 0.3L_{sc}) \quad \text{(B6)}$$

regulates twitch duration as function of contractile element length.

Active fiber stress $\sigma_{f,a}$ is calculated by

$$\sigma_{f,a} = \sigma_{act} \cdot C \cdot L_{sNorm} \quad \text{(B7)}$$

Equation B7 is a modification from [70] such that active tension does not increase indefinitely with increasing sarcomere length. This imposes a limit on the total amount of work a fiber can generate. Table B.1 lists the values of the contractile material parameters.

Parameter and unit	Description	Value
a_{Hill} [-]	Parameter that determines curvature of Hill relation during stretching	1.5
C_{rest} [-]	Diastolic contractility level	0.0
b_{Hill} [-]	Parameter that determines curvature of Hill relation during shortening	1.5
L_{s0} [μm]	Contractile element length at zero active stress	1.51
L_{SerEl} [μm]	Length of series elastic element during isometric contraction	0.04
v_{max} [μm/sec]	Unloaded sarcomere shortening velocity	5.0
τ_d [ms]	Relaxation time scaling factor	33.8
τ_r [ms]	Contraction rise time scaling factor	28.1
τ_{sc} [ms]	Twitch duration scaling factor	293
σ_{act} [kPa]	Active stress scaling factor	65.0

Table B. 1 – Active material properties of the mechanics model.

Bibliography

[1] A. J. Marelli, A. S. Mackie, R. Ionescu-Ittu, E. Rahme, L. Pilote. 2007. *Congenital heart disease in the general population: changing prevalence and age distribution*. Circulation 115: 163-172.

[2] M. E. Brickner, L. D. Hillis, R. A. Lange. 2000. *Congenital heart disease in adults. First of two parts*. N Engl J Med. 342: 256-263.

[3] M. E. Brickner, L. D. Hillis, R. A. Lange. 2000. *Congenital heart disease in adults. Second of two parts*. N Engl J Med 342: 334-342.

[4] S. Piran, G. Veldtman, S. Siu, G. D. Webb, P. P. Liu. 2002. *Heart failure and ventricular dysfunction in patients with single or systemic right ventricles.* Circulation 105: 1189-1194.

[5] C. M. Augustin, A. Neic, M. Liebmann, A. J. Prassl, S. A. Niederer, G. Haase, G. Plank. 2016. *Anatomically accurate high resolution modeling of human whole heart electromechanics: A strongly scalable algebraic multigrid solver method for nonlinear deformation*. J Comput Phys (15) 305: 622–646.

[6] H. Talbot, S. Marchesseau, C. Duriez, M. Sermesant, S. Cotin, H. Delingette. *2013 Towards an interactive electromechanical model of the heart*. Interface Focus 3: 20120091.

[7] R. C. P. Kerckhoffs, O. P. Faris, P. H. M. Bovendeerd, F. W. Prinzen, K. Smits, E. R. McVeigh, T. Arts. 2005. *Electromechanics of paced left ventricle simulated by straightforward mathematical model: comparison with experiments*. Am J Physiol Heart Circ Physiol 289: H1889–H1897.

[8] A. Krishnamurthy, C. T. Villongco, J. Chuang, L. R. Frank, V. Nigam, E. Belezzuoli, P. Stark, D. E. Krummen, S. Narayan, J. H. Omens, A. D. McCulloch, R. C. P. Kerckhoffs. 2013. *Patient-specific models of cardiac biomechanics*. J Comput Phys 244: 4–21.

[9] J. Aguado-Sierra; A. Krishnamurthy, C. Villongco, J. Chuang, E. Howard, M. J. Gonzales, J. Omens, D. E. Krummen, S. Narayan, R. C. P. Kerckhoffs. 2011. *Patient-Specific Modeling of Dyssynchronous Heart Failure: A Case Study*. Progress in Biophysics and Molecular Biology.

[10] A. J. Prassl, F. Kickinger, H. Ahammer, V. Grau, J. E. Schneider, E. Hofer, E. J. Vigmond, N. A. Trayanova, G. Plank. 2009. *Automatically generated, anatomically accurate meshes for cardiac electrophysiology problems*. IEEE Trans Biomed Eng 56 (5): 1318–1330.

[11] J. D. Bayer, R. C. Blake, G. Plank, N. A. Trayanova.2012. *A novel rule-based algorithm for assigning myocardial fiber orientation to computational heart models*. Ann Biomed Eng 40 (10): 2243– 2254.

[12] C. G. Fonseca, M. Backhaus, D. A. Bluemke, R. D. Britten, J. D. Chung, B. R. Cowan, I. D. Dinov, J. P. Finn, P. J. Hunter, A. H. Kadish, D. C. Lee, J. A. C. Lima, P. Medrano-Gracia, K. Shivkumar, A. Suinesiaputra, W. Tao, A. A. Young. 2011. *The Cardiac Atlas Project - an imaging database for computational modeling and statistical atlases of the heart*. Bioinformatics 27: 2288-2295.

[13] J. Betts Gordon. 2013. Anatomy & physiology: 787–846.

[14] J. Goldstein. 2005. *The right ventricle: what's right and what's wrong*. Coron Artery Dis 16:

1–3.

[15] L. J. Dell'Italia. 1991. *The right ventricle: anatomy, physiology, and clinical importance*. Curr Probl Cardiol 16: 653–720.

[16] F. Haddad, S. A. Hunt, D. N. Rosenthal, D. J. Murphy. 2008. *Right Ventricular Function in Cardiovascular Disease, Part I. Anatomy, Physiology, Aging, and Functional Assessment of the Right Ventricle*. Circulation 117: 1436-1448.

[17] A. N. Redington, H. H. Gray, M. E. Hodson, M. L. Rigby, P. J. Oldershaw. 1988. *Characterisation of the normal right ventricular pressure-volume relation by biplane angiography and simultaneous micromanometer pressure measurements*. Br Heart J 59: 23-30.

[18] D. A. Goor, C. W. Lillehei. 1975. *Congenital malformations of the heart*. 1st ed New York: Grune and Stratton: 1–37.

[19] S. Y. Ho, P. Nihoyannopoulos. 2006. *Anatomy, echocardiography, and normal right ventricular dimensions*. Heart 92 (Suppl I): i2-i13.

[20] M. Lev. 1952. *Pathologic anatomy and interrelationship of hypoplasia of the aortic tract complexes*. Lab Invest 1: 61-70.

[21] J. A. Noonan, A. S. Nadas. 1958. *The hypoplastic left heart syndrome: an analysis of 101 cases*. Pediatr Clin North Am 5: 1029-56.

[22] R. Farrugetti. 1998. *Vital statistics: US birth rates. National Center for Health Statistics*. United States Department of Health and Human Services. Annual Report for the Year 1997. Ed. The World Almanac and Book of Facts 1999.

[23] C. D. Morris, J. Outcalt, V. D. Menashe. 1990. *Hypoplastic left heart syndrome: natural history in a geographically defined population*. Pediatrics 85: 977-1000.

[24] L. R. Feit, J. A. Copel, C. S. Kleinman. 1991. *Foramen ovale size in the normal and abnormal human fetal heart: an indicator of transatrial flow physiology.* Ultrasound Obstet Gynecol 1: 313-9.

[25] M. R. De Leval. 1992. *Right heart bypass operations*. W.B. Saunders Company (eds): 565-585.

[26] A. Blalock, H.B. Taussig. 1945. *The surgical treatment of malformations of the heart in which there is pulmonary stenosis or pulmonary atresia*. J Amer Med Assoc 128: 189-202.

[27] F. Fontan, E. Baudet. 1971. *Surgical repair of tricuspid atresia*. Thorax 26: 240-247.

[28] E. L. Bove, T. R. Lloyd. 1996. *Staged reconstruction for hypoplastic left heart syndrome*. Ann Surg 224: 387-95.

[29] M. D. Iannettoni, E. L. Bove, R. S. Mosen, et al. 1994. *Improving results with first-stage palliation for hypoplastic left heart syndrome*. J Thorac Cardiovasc Surg 107: 1121-8.

[30] W. I. Douglas, C. S. Goldberg, R. S. Mosca, I. H. Law, E. L. Bove. 1999. *Hemi-Fontan procedure for hypoplastic left heart syndrome: outcome and suitability for Fontan*. Ann Thorac Surg 68: 1361-8.

[31] E. L. Bove. 1998. *Current status of staged reconstruction for hypoplastic left heart syndrome*. Pediatr Cardiol 19: 308-15.

[32] P. M. F. Nielsen, I. J. Le Grice, B. H. Smaill, P. J. Hunter. 1991. *Mathematical model of geometry and fibrous structure of the heart*. Am J Physiol Heart Circ Physiol 260: H1365–78.

[33] F. J. Vetter, A. D. McCulloch. 1998. *Three-dimensional analysis of regional cardiac function: a model of rabbit ventricular anatomy*. Prog Biophys Mol Biol 69: 157–83.

[34] R. Haddad, P. Clarysse, M. Orkisz, P. Croisille, D. Revel, I. E. Magnin. 2005. *A realistic anthropomorphic numerical model of the beating heart*. Funct Imaging Model Heart 2005: 384–93.

[35] B. Appleton, Q. Wei, N. Liu, L. Xia, S. Crozier, F. Liu. 2006. *An electrical heart model incorporating real geometry and motion.* 27th Annu Int Conf Eng Med Biol Soc: 345–8.

[34] P. Colli Franzone, L. Guerri, M. Pennacchio, B. Taccardi. 1998. *Spread of excitation in 3-D models of the anisotropic cardiac tissue. II. Effects of fiber architecture and ventricular geometry*. Math Biosci 147: 131–71.

[35] R. C. Kerckhoffs, P. H. M. Bovendeerd, J. C. S. Kotte, F. W. Prinzen, K. Smits, T. Arts. 2003. *Homogeneity of cardiac contraction despite physiological asynchrony of depolarization: a model study*. Ann Biomed Eng 31: 536–47.

[36] S. Ordas, E. Oubel, R. Sebastian, A. F. Frangi. 2007. *Computational anatomy atlas of the heart*. 5th Int Symp Image Signal Process Anal: 338–42.

[37] J. D. Humphrey, F. C. P. Yin. 1987. *On constitutive relations and finite deformations of passive cardiac tissue. Part I. A pseudo-strain energy function.* J Biomech Eng 109: 298–304.

[38] J. D. Humphrey, R. K. Strumpf, F. C. P. Yin. 1990. *Determination of constitutive relation for passive myocardium. I. A new functional form*. J Biomech Eng 112: 333–339.

[39] J. M. Guccione, A. D. McCulloch, L. K. Waldman. 1991. *Passive material properties of intact ventricular myocardium determined from a cylindrical model*. J Biomech Eng 113: 42–55.

[40] K. D. Costa, P. J. Hunter, J. S. Wayne, L. K. Waldman, J. M. Guccione, A. D. McCulloch. 1996. *A three-dimensional finite element method for large elastic deformations of ventricular myocardium. II. Prolate spheroidal coordinates*. J Biomech Eng 118: 464–472.

[41] L. L. Demer, F. C. P. Yin. 1983. *Passive biaxial mechanical properties of isolated canine myocardium*. J Physiol Lond 339: 615–630.

[42] B. H. Smaill, P. J. Hunter. 1991. *Structure and function of the diastolic heart: material properties of passive myocardium.* Theory of heart: biomechanics, biophysics, and nonlinear dynamics of cardiac function: 1-29.

[43] V. P. Novak, F. C. P. Yin, J. D. Humphrey. 1994. *Regional mechanical properties of passive myocardium*. J Biomech Eng 27: 403–412.

[44] K. D. Costa, J. W. Holmes, A. D. McCulloch. 2001. *Modeling cardiac mechanical properties in three dimensions*. Phil Trans R Soc Lond A 359: 1233–1250.

[45] H. Schmid, M. P. Nash, A. A. Young, P. J. Hunter. 2006. *Myocardial material parameter estimation—a comparative study for simple shear.*

[46] G. Holzapfel, R. Ogden. 2009. *Constitutive modelling of passive myocardium: a structurally based framework for material characterization*. Philosophical Transactions A 367.

[47] J. Walker, M. Ratcliffe, P. Zhang, A. Wallace, B. Fata, E. Hsu, D. Saloner, J. Guccione. 2005. *MRI-based finite-element analysis of left ventricular aneurysm*. American Journal of Physiology – Heart and Circulatory Physiology 289 (2): H692.

[48] M. Sermesant, R. Razavi. 2010. *Personalized computational models of the heart for cardiac resynchronization therapy*. Patient-Specific Modeling of the Cardiovascular System: 167–182.

[49] S. Klotz, I. Hay, M. L. Dickstein, G. H. Yi, J. Wang, M. S. Maurer, D. A. Kass, D. Burkhoff. 2006. *Single-beat estimation of end-diastolic pressure-volume relationship: a novel method with potential for noninvasive application*. American Journal of Physiology – Heart and Circulatory Physiology 291 (1): H403–H412.

[50] I. Mirsky. 1976. *Assessment of passive elastic stiffness of cardiac muscle: mathematical concepts, physiologic and clinical considerations, directions of future research*. Prog Cardiovasc Dis 18: 277–308.

[51] R. C. P. Kerckhoffs, S. N. Healy, T. P. Usyk, A. D. McCulloch. 2006. *Computational Methods for Cardiac Electromechanics*. Proceedings of the IEEE.

[52] T. Arts, T. Delhaas, P. Bovendeerd, X. Verbeek, F. Prinzen. 2005. *Adaptation to mechanical load determines shape and properties of heart and circulation: the CircAdapt model*. American Journal of Physiology – Heart and Circulatory Physiology 288 (4): H1943.

[53] J. Lumens, T. Delhaas, B. Kirn, T. Arts. 2009. *Three-wall segment (TriSeg) model describing mechanics and hemodynamics of ventricular interaction*. Annals of Biomedical Engineering 37 (11): 2234–2255.

[54] N. Westerhof, G. Elzinga, G. C. Van Den Bos. 1973. *Influence of central and peripheral changes on hydraulic input impedance of systemic arterial tree*. Med Biol Eng 11: 710–723.

[55] N. Stergiopulos, B. E. Westerhof, N. Westerhof. 1999. *Total arterial inertance as the fourth element of the windkessel model*. Amer J Physiol, Heart Circulat Physiol 276: H81–H88.

[56] Y. Sun, M. Beshara, R. J. Lucariello, S. A. Chiaramida. 1997. *A comprehensive model for right-left heart interaction under the influence of pericardium and baroreflex*. Amer J Physiol, Heart Circulat Physiol 41: H1499–H1515.

[57] C. H. Liu, S. C. Niranjan, J. W. Clark, K. Y. San, J. B. Zwischenberger, A. Bidani. 1998. *Airway mechanics, gas exchange, and blood flow in a nonlinear model of the normal human lung*. J Appl Physiol 84: 1447–1469.

[58] J. F. Golden, J. W. Clark, P. M. Stevens. 1973. *Mathematical modeling of pulmonary airway dynamics*. IEEE Trans Biomed Eng 20: 397–404.

[59] T. P. Usyk, A. D. McCulloch. 2003. *Electromechanical model of cardiac resynchronization in the dilated failing heart with left bundle branch block.* J Electrocardiol 36: 57–61.

[60] D. P. Nickerson, N. Smith, P. Hunter. 2005. *New developments in a strongly coupled cardiac electromechanical model*. Europace 7: 5118–5127.

[61] F. Liu, W. X. Lu, L. Xia, G. H. Wu. 2001. *The construction of three-dimensional composite finite element mechanical model of human left ventricle*. JSME Int J Series C, Mech Syst Mach Elements Manuf 44: 125–133.

[62] S. A. Niederer, P. Lamata, G. Plank, P. Chinchapatnam, M. Ginks. 2012. *Analyses of the*

Redistribution of Work following Cardiac Resynchronisation Therapy in a Patient Specific Model. PLoS ONE 7 (8): e43504.

[63] H. Talbot, S. Marchesseau, C. Duriez, M. Sermesant, S. Cotin, H. Delingette. 2013. *Towards an interactive electromechanical model of the heart.* Interface Focus 3: 20120091.

[64] T. P. Usyk, R. Mazhari, A. D. McCulloch. 2000. *Effect of laminar orthotropic myofiber architecture on regional stress and strain in the canine left ventricle*. J Elasticity 61: 143–164.

[65] L. Ge, W. G. Morrel, A. Ward, R. Mishra, Z. Zhang, J. M. Guccione, E. A. Grossi, M. B. Ratcliffe. 2014. *Measurement of mitral leaflet and annular geometry and stress after repair of posterior leaflet prolapse: Virtual repair using a patient specific finite element simulation*. Ann Thorac Surg 97 (5): 1496–1503.

[66] H. F. Choi, J. D'hooge, F. E. Rademakers, P. Claus. 2010. *Influence of left-ventricular shape on passive filling properties and end-diastolic fiber stress and strain*. Journal of Biomechanics 43: 1745–1753.

[67] J. Bogaert, S. Dymarkowski, A. M. Taylor. 2005. Clinical Cardiac MRI.

[68] D. Nordsletten, M. McCormick, P. J. Kilner, P. Hunter, D. Kay, N. P. Smith. 2010. *Fluidesolid coupling for the investigation of diastolic and systolic human left ventricular function*. International Journal for Numerical Methods in Biomedical Engineering.

[69] R. C. Kerckhoffs, M. L. Neal, Q. Gu, J. B. Bassingthwaighte, J. H. Omens, A. D. McCulloch. 2007. *Coupling of a 3D Finite Element Model of Cardiac Ventricular Mechanics to Lumped Systems Models of the Systemic and Pulmonic Circulation*. Ann Biomed Eng 35: 1–18.

[70] R. C. P. Kerckhoffs, J. H. Omens, A. D. McCulloch, L. J. Mulligan. 2010. *Ventricular dilation and electrical dyssynchrony synergistically increase regional mechanical non-uniformity but not mechanical dyssynchrony: A computational model*. Circ Heart Fail 3 (4): 528–536.

[71] W. Kroon, T. Delhaas, P. Bovendeerd, T. Arts. 2009. *Computational analysis of the myocardial structure: Adaptation of cardiac myofiber orientations through deformation*. Medical Image Analysis 13: 346–353.

[72] F. Dorri , P. F. Niederer, P. P. Lunkenheimer. 2006. *A finite element model of the human left ventricular systole*. Computer Methods in Biomechanics and Biomedical Engineering 9 (5): 319-341.

[73] M. Pluijmert, P. H. Bovendeerd, W. Kroon. 2014. *Effects of activation pattern and active stress development on myocardial shear in a model with adaptive myofiber reorientation*. Am J Physiol Heart Circ Physiol 306: H538–46.